Dissertation

Submitted to the
Combined Faculties for the Natural Sciences and Mathematics
of the Ruperto-Carola University of Heidelberg, Germany
for the degree of
Doctor of Natural Sciences

Put forward by
Maximilian Hackner, M.Sc.
Stuttgart, Germany

Oral examination: October 21, 2021

Metalfiber based 3-dimensional electrical current collectors for ultra-thick battery electrodes

Referees:

Prof. Joachim P. Spatz
Institute for Molecular Systems Engineering
University of Heidelberg

Max-Planck-Institute for Medical Research
Heidelberg

Prof. Martin Möller
Institute of Technical and Macromolecular Chemistry
RWTH Aachen University

DWI – Leibniz-Institute for Interactive Materials
Aachen

Zusammenfassung

Die Entwicklung innovativer Technologien bedarf oft grundlegender neuer Materialeigenschaften einzelner Komponenten. In dieser Arbeit wurden metastabile Metallfasern mit einzigartigen mechanischen und thermodynamischen Eigenschaften sowie kristallografischen Charakteristika zu mechanisch stabilen, elastischen 3-dimensionalen Netzen verknüpft, ohne dass die Geometrie und die physikalischen und thermodynamischen Eigenschaften der Fasern verändert wurde. Die Metallfasernetze wurden als 3-dimensionale Stromkollektoren in der Lithium-Ionen-Batterietechnologie eingesetzt und verbessern damit grundlegend die Batterietechnologie. Prinzipiell werden verbesserte Batterietechnologien in vielen gesellschaftlich relevanten Anwendungen dringend benötigt, um deren Energieverbrauch ökologischer und ökonomischer zu gestalten.

Die durch ein Meltspinning-Verfahren hergestellten Metallfasern basieren auf einer Kupfer-Silizium-Legierung. Die grundlegenden physikalischen und thermodynamischen Eigenschaften sowie der kristallographische Zustand der Metallfasern wurde quantifiziert. Die Metallfasern wiesen eine Länge von mehreren Zentimetern, eine Breite von 10-100 Mikrometern und eine Dicke von 2-10 Mikrometern auf. Die mechanischen Eigenschaften wurden als Funktion der Metallfaserdimension und des kristallographischen und thermodynamischen Zustandes quantifiziert. Insbesondere erwies sich die thermodynamisch metastastabile Phase für die Verknüpfung der Metallfasern als grundlegend. Während des Herstellungsprozesses der Metallfasern wird die Metallschmelze innerhalb weniger Millisekunden abgekühlt und zur Erstarrung gebracht. Als Folge befindet sich die kristallische Struktur bei Raumtemperatur nicht im thermodynamischen Gleichgewicht, deren gespeicherte Energie bestimmt wurde.

Eine dauerhafte Verknüpfung der Metallfasern wurde durch das kalte und warme Sintern der Fasern erfolgreich dargestellt, ohne dass die grundlegende Geometrie und teils die physikalischen sowie thermodynamischen Eigenschaften der Fasern beeinträchtigt wurden. An den Kontaktpunkten zwischen den Fasern zeigt sich bevorzugt eine Verknüpfung durch geringe Aktivierung atomarer Diffusion mittels mechanisch aufgebauten Drucks oder Temperatur. Grund hierfür ist die beim Abschrecken der Metallschmelze in den Fasern kristallographisch gespeicherte Energie.

Die 3-dimensionalen Metallfasernetze wurden hinsichtlich ihrer Eignung als elektrische Stromableiter in Lithium-Ionen-Batterien untersucht. Vor allem die Verbesserung der mechanischen und elektrischen Eigenschaften von Lithium-Ionen-Batterien, die die Grundlage für eine Vielzahl von Prozessen in Batterien sind, stand in dieser Arbeit im Vordergrund. Die 3-dimensionalen Metallfasernetze ermöglichten grundsätzlich die Darstellung funktionsfähiger superdicker Batterieelektroden, die eine deutlich erhöhte Flächenkapazität von größer 8 mAh cm^{-1} aufweisen.

Abstract

The development of innovative technologies often requires fundamental new materials properties of individual components. In the present work, metastable metal fibers with unique mechanical and thermodynamic properties as well as crystallographic characteristics were linked to form mechanically stable, elastic 3-dimensional networks without changing the geometry, physical and thermodynamic properties of the fibers. The metal fiber networks have been used in lithium-ion battery technology as 3-dimensional current collectors, fundamentally improving battery technology. Worldwide there is an urgent need for improved battery technologies which are more ecological and economical.

The metal fibers produced by a Melt spinning process are based on a copper silicon alloy. The basic physical and thermodynamic properties as well as the crystallographic state of the metal fibers were first quantified. The metal fibers had a length of several centimeters, a width of 10-100 micrometers, and a thickness of 2-10 micrometers. The mechanical properties were quantified as a function of metal fiber dimension, crystallographic and thermodynamic state. In particular, the thermodynamic metastable phase was shown to be instrumental for linking the metal fibers. During the metal fiber fabrication process, the molten metal is cooled and solidified within a few milliseconds. As a result, the crystalline structure at room temperature is not in a thermodynamic equilibrium, the stored energy of which was determined.

A permanent linkage of the metal fibers was successfully implemented by cold and warm sintering of the fibers without affecting the basic geometry and partly the physical as well as thermodynamic properties of the fibers. Low activation of atomic diffusion by means of mechanically built-up pressure or temperature resulted in a linkage preferentially at the contact points between fibers. The reason for this is the crystallographic energy stored in the fibers during quenching of the molten metal.

The 3-dimensional metal fiber networks were investigated in terms of their suitability as electrical current conductors in lithium-ion batteries. In particular, this work focused on improving the mechanical and electrical properties of lithium-ion batteries, which are the basis for a variety of processes in batteries. In principle, the 3-dimensional metal fiber networks enabled the fabrication of functional super-thick battery electrodes, which have a significantly increased surface capacitance of greater than 8 mAh cm^{-1}.

Contents

Acronyms

CNT	Carbon nanotubes
CuSi3	Copper (97 wt.-%) Silicon (3 wt.-%)
CuSi4	Copper (96 wt.-%) Silicon (4 wt.-%)
DMC	Dimethyl carbonate
DSC	Differential Scanning Calorimetry
EC	Ethylene carbonate
EIS	Electrochemical impedance spectroscopy
LCO	Lithium cobalt oxide
LIB	Lithium-Ion-Battery
LTO	Lithium titanium oxide
NI	Nanoindentation
NMC	Lithium nickel manganese oxide
PE	Polyethylene
PP	Polypropylene
PVA	Polyvinyl alcohol
PVDF-HFP	Polyvinylidenflouride-*co*-hexafluoropropylene
PVP	Polyvinylpyrolidone
SEM	Scanning Electron Microscopy
SOC	State of charge
SPM	Scanning Probe Microscopy
STA	Simultaneous Thermal Analysis
TG	Thermogravimetry
XRD	X-Ray Diffraction

1. Introduction

A better battery has significant societal benefits. Its success accelerates the transformation from a fossil fuels-based economy to a CO_2-free economy. [1-3] Batteries are being used in all mobile vehicles, consumer electronics and time-shifted energy supply systems, such as the powering of houses to name a few. This is because batteries are loaded with electrical energy, which may be produced entirely by environmentally friendly technologies. A better battery will have to be safe, have high gravimetric or volumetric energy density, high charging and discharging rates, be completely recyclable and, eventually, economically inexpensive. [4-6] So far battery research has been slow-moving when it comes to cell architecture, meaning that for decades batteries have been produced in the same way. The true potential of battery technology will only be unlocked once new structures with improved chemistries are implemented. [7] This requires fundamental knowledge and engineering science-based breakthroughs in material chemistry which accumulates and releases energy, called active material, current collector and general cell design. It is widely understood in the battery field that the design of thick batteries is a major obstacle. This thesis explores fundamentally what limits the formation of thick batteries and presents a new battery design principle.

Lithium-Ion Batteries (LIBs) are currently the dominating electrochemical storing system for electrical energy. The principles of the batteries go back to John Goodenough [8], Stanley Whittingham [9] and Akira Yoshino [10], who were awarded the Nobel Prize in Chemistry in 2019. The LIB contains several electrochemically active as well as inactive components. Electrochemically active components include anode and cathode active materials, and the electrolyte. Electrochemically inactive components are mainly the separator, current collector, additives, and the casing. [11]

The working principle is based on lithium ion (Li^+) diffusion in an electrolyte from cathode to anode (loading) and vice versa (unloading). This is schematically shown in Figure 1. Lithium is stored inside the active material at anode and cathode inside the respective structure. Here, two types of storage must be distinguished. The first type is known as conversion electrodes. Here, the atomic charge in the crystal of the active material changes during lithiation. Typical materials are therefore transition metal oxides like manganese oxide. The charge of the manganese changes during lithiation from Mn^0 to Mn^{2+} which provides a theoretical capacity of 800 mAh g^{-1}. [12]

The second type of storage is intercalation of lithium inside material structures without a change of atomic charge. Two principle types of intercalation active materials are known: Layer-structured ones, e.g. graphite (anode) or $LiNiMnCoO_2$ (NMC) (cathode). Here, the lithium is stored in between the layers of the active material. On the other hand, there are materials in which the lithium is ingested into the crystal structure, e.g. in $Li_4Ti_5O_{12}$ (LTO) (anode). Intercalation and deintercalation occurs at a material-specific voltage, the so-called intercalation voltage, e.g. for graphite at 0.1 V vs. Li/Li^+ or 3.7 V vs. Li/Li^+ for NMC [11]. The cell voltage is then given by the difference between cathode and anode intercalation voltage, e.g. for a Graphite-NMC-Battery, which is the most common one, a value of 3.6 V is generated.

If all lithium is removed from the active material, the assembled structure may collapse. Therefore, only a certain fraction of the lithium in the active material can be used and the real usable capacity is lower than the theoretical one. For $Li_{1-x}CoO_2$ (LCO) the theoretical capacity with $x = 1$ yields at 274 mAh g^{-1}, whereas the real capacity at $x = 0.3$ ranges from 140-150 mAh g^{-1} without collapse. This effect is based on the Co^{3+}/Co^{4+} redox couple that can only compensate the lithium ion removal to a certain point before phase transformation sets in. This phase transformation converts the usable hexagonal structure to a monoclinic phase and is not electrochemically reversible. [11, 13, 14]

As described above, lithium ions are stored inside the active material at the anode and cathode. However, to make use of the potential difference in the charged state or to recharge the battery, it is necessary to ensure ion transport between anode and cathode. Hence, an ion conductive electrolyte is required. Lithium salts such as $LiPF_6$ dissolved in compatible solvents usually serve as electrolyte. Typically, one or several carbonates (e.g. ethylene-, dimethyl-, diethyl-, ethylmethylcarbonate) are the solvents of choice. There are three decisive factors the electrolyte has to meet: Firstly, high resistance against decomposition during loading and unloading of the battery. Secondly, only minor electrical conductivity and thirdly, high lithium ion diffusion which is typically in the range of 10^{-10} m^2 s^{-1}. Especially in thick 3D batteries, demand for good lithium ion transport through the whole assembly is very high. [11, 15, 16]

The next generation of lithium ion batteries are solid-state batteries. [5] In these type of battery, the liquid electrolyte is replaced with a solid one in form of a polymer gel. For these pseudo all-solid-state batteries, the same type of active materials is mainly used as for traditional liquid electrolyte cells. In real all-solid-state batteries, no electrolyte is used. [17] Therefore, a high lithium ion transport in the active material is needed. Here, lithium metal anodes are used due to their high capacity of 3860 mAh g^{-1} and their low potential of -3.04 V vs. the standard hydrogen electrode. [18] A large problem for lithium metal anodes is dendrite formation due to polarities in the electrode. Dendrite formation, however, can be prevented with a better potential distribution as, for example, in electrode systems with a 3D current collector. [19]

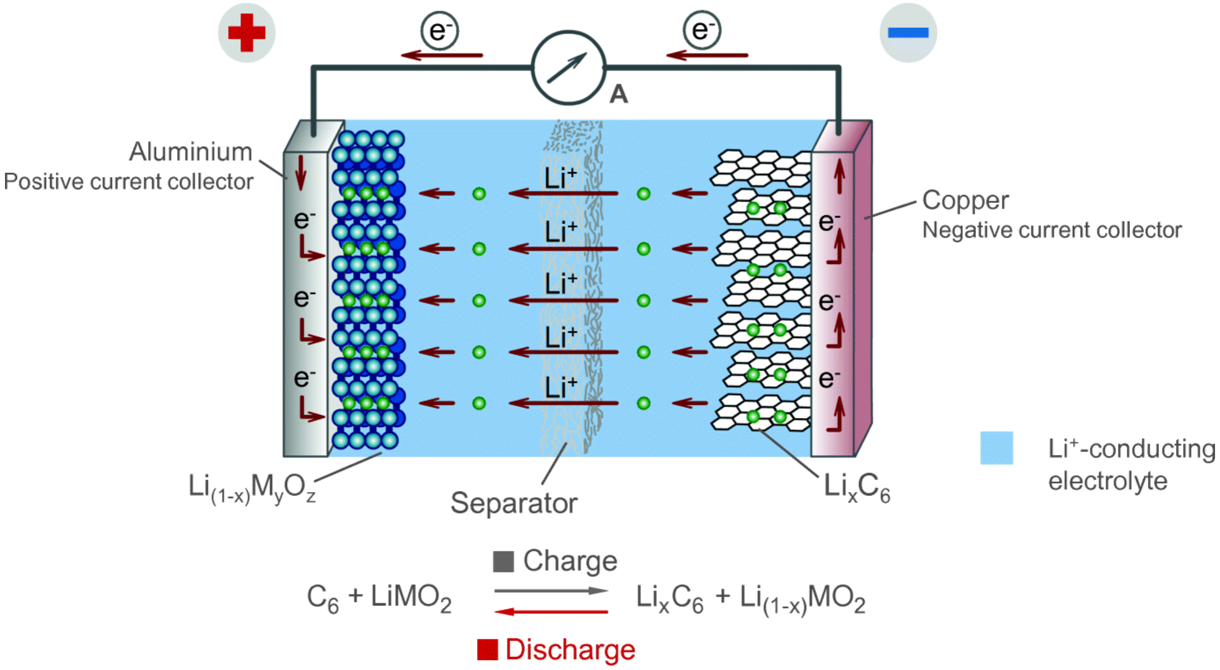

Figure 1: Scheme of the structure and working principle of a Lithium-Ion-Battery. [11] Reprinted under permission by Springer (© 2018 Springer)

Additionally, a separator is needed. Its primary function is the physical and electrical separation of anode and cathode, thus preventing an electric short circuit of the cell, i.e. the separator needs to be electrically non-conductive. While the electron transport needs to be suppressed, a good ion transport through the current collector is necessary. This can be achieved by porous separator structures that can be penetrated by the electrolyte containing the ions. Another possibility are ion conductive materials, which are mainly used in all solid state batteries. Hence, separators are mainly based on porous polymers and/or ceramic particles and/or fibers. In some separators, mainly ceramic-based separators, it is also possible to suppress the formation of lithium dendrites, which could pierce the separator und would end in short-circuiting the cell. Therefore, a high mechanical stability of the separator is desirable. To ensure a good performance, thickness and porosity are crucial. If the porosity is too low or the separator too thick, lithium ion transport will be hindered whereas too thin or too porous structures fail at reliably isolating the cell. [11, 20, 21]

In order to collect or provide electrons from the active material to the electrical circuit and vice versa, a so-called current collector is needed. This is typically an electrically highly conductive material that is coated with the active material. In state-of-the-art batteries, a copper foil at the anode side and an aluminum foil at the cathode side is used. Since the active material's electric conductivity is lower compared to the current collector's, electron transport in the active material is better close to the foil. Especially in systems with low conductive active materials like oxide-based electrodes, the demand for conductive additives like carbon black graphene sheets [22], carbon nanotubes [23] or metallic nanowires [24] is high. [25, 26]

A current trend in Lithium-Ion Batteries is thicker electrodes. Here, the fraction of inactive components like current collector foils or also separators can be severely decreased [27] leading to a significantly increased gravimetric and volumetric energy density. The gravimetric energy density is the energy that is stored per gravimetrical unit in a battery. Together with the volumetric density, i.e. the energy per volumetric unit, they are the key parameters to describe the battery performance. Figure 2 illustrates the impact of electrode thickness and the resulting fraction of inactive components. Currently, the main problems and challenges are the poor electrical connection of active material located further away from the current collector and the poor ionic conductivity due to the thick layers. Figure 3 illustrates the transport processes in lithium-ion batteries in detail. The electrical connection of the active material at the current collector is much better than for the active material far away from the current collector due to the bad electric conductivity of the active material. Therefore, a potential gradient inside the active material bulk forms. Since intercalation requires a certain threshold voltage, the active material next to the current collector can be charged more than other parts of the active material. In contrast to the electric conductivity gradient towards the current collector, lithium ion diffusion is increased at the separator and the lithium ion source. Consequently, the thicker the electrode, the larger is the distance between the two gradient maxima. In a worst-case scenario, the two gradients are not overlapping and, thus, the battery cannot be charged.

To address the electrical conductivity problem, work has been underway for some time on 3D current collectors that use less conductive additives to enable electrical conductivity throughout the active material. Different forms of three-dimensional structures like metallic foams [28], graphene foams [29], 3D-printed structures, [30] or metallic fibers [31] were tested extensively. All these systems exhibit interesting properties and offer new possibilities for higher loading rates, higher energy densities, and longer lifetimes. However, most of these systems are costly and time intensive to produce and none of these have been translated from basic research into mass production. [7, 19, 32, 33] While in 2D systems, the foil is coated with an active material layer, in 3D systems the structure is infiltrated with the active material and the electrode is pervaded by the 3D current collector over the overall thickness. Therefore, the potential gradient is restricted by the pores and does not stretch out over the whole current collector. Thus, theoretically, the thickness can be increased infinitely. For 3D systems, the pore size must be tuned precisely to adjust the electrically based battery properties.

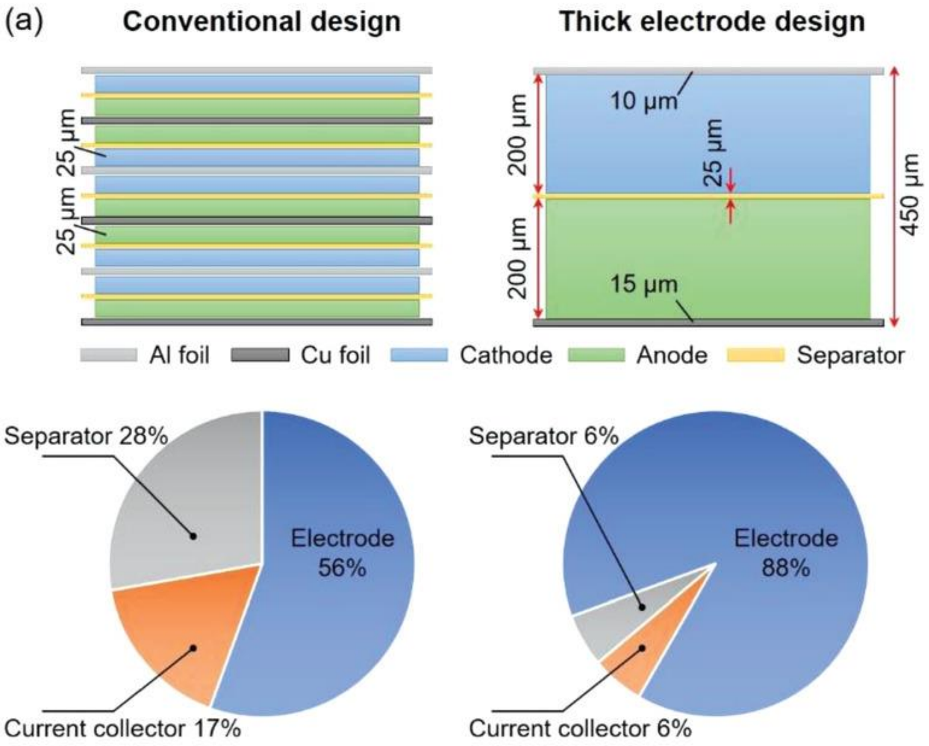

Figure 2: Scheme of thin and thick electrodes and their components ratio. [27] Adapted and reprinted under permisson by Wiley (© 2019 Wiley)

The main research focus in 3D current collectors are currently metallic structures like foams. Metals are characterized by very high electric conductivity as well as a very high mechanical stability. The main problem here are the production possibilities. In general, there are two production routes: In the first, the metal melt is frothed up with gas and cooled as metal foam. Due to random gas bubble recombination, the pore size diameter is very inhomogeneous and mainly in the millimeter range. Furthermore, the pore size cannot be adjusted to the demanded level. Consequently, the inhomogeneous and large pore sizes lead to a varying charging performance for the different pores. [34-36] The second route uses salts with high melting point. These salt particles act here as place holders in the metal melt. After solidification of the metal, the salt is dissolved and thus removed from the metal foam. With this strategy, the pore size diameter can be adjusted very accurately. [36] However, a general challenge for both strategies is the need of an open and connected porosity of the foam. [37] Here, precise process control necessary. However, this makes the whole process costly and laborious and, therefore, not preferable for large-scale battery production. Moreover, the most prominent metal foams are copper or nickel based. Due to the limited electrochemical stability of both materials, they are not suitable for active materials with a high intercalation level. [7]

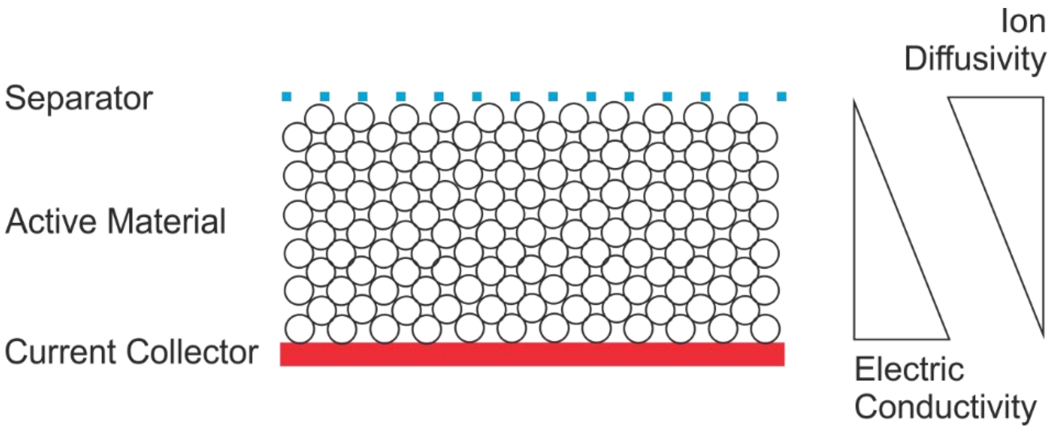

Figure 3: Scheme of the thickness dependence of transport processes in lithium-ion-batteries.

Additionally, graphene foams are currently of significant interest in 3D current collector research. Here, the production strategy is mainly based on graphene oxide plates which are dissolved and dried afterwards. The structure determining process is simple vacuum filtration [38] or, more advanced, freeze drying [39]. After the drying step, a loose structure is formed that has to be interconnected to form a stable structure. Therefore, the graphene oxide is reduced to graphene which then combines with the surrounding plates and forms a mechanically stable connection. The reduction can be initiated, for example, by thermal treatment. [33] A promising factor is that during the production process the active material can be introduced directly into the network and, therefore, provides a good charging performance. In addition, the graphene itself can be charged. [33, 39, 40] However, the main issues are the mechanical stability of the substrate and the pore size diameter, which is mainly in the nanometer to low micrometer range. Within this pore size diameter range, the infiltration of active material after the formation of the 3D structure, for example by doctor blading, is nearly impossible. The reduction process under vacuum, protective or reducing gas at high temperatures is again laborious and problematic for large-scale production.

Metal fibers are also another field of interest in 3D current collector research. Here, two types of metal fibers must be distinguished. The first type of fibers are nanowires grown from solution made of a wide variety of metals. These networks are connected with each other and form a metal fiber network but with a pore size in the lower micrometer range. With their typical fiber thickness below 1 µm the networks are not very stable against mechanical deformation. Fiber growth is slow and cost-intensive, so this route is not very interesting for large-scale production.

The second type of fibers are metal fibers in the micrometer range, which can be produced for example by bundle drawing - a method limited to non-corrosive materials like stainless steel. Jenax Inc. is building secondary batteries utilizing 3D networks made of stainless steel fibers for the current collector network. [41] Due to the electrochemical limitation of stainless steel, active materials with an intercalation voltage of over 3.8 V vs. Li/Li^+ are not suitable for these types of fiber networks. The mechanical stability, electric conductivity, and the pore size adjustability are favorable in this type of system. [42]

In order to summarize the suitability of existing technologies, the 3D current collectors were evaluated in the following categories: i) accurate pore size adjustment in the range of 80-200 µm, ii) electrochemical stability uup to 4.3 V vs. Li/Li^+, iii) mechanical stability, iv) electrical conductivity and v) large-scale production. Only state-of-the-art products were taken into account for all criteria but not small lab-scale proof of principles. For the metal foams, irrespective of the production route, commercially available copper, nickel, cobalt, silver, stainless steel and titanium networks were taken into account. The graphene foams were assumed as current collector which needs to be filled with active material afterwards. The while formation plated active material provides only to less area capacities for industrial use. For the 3D-printed structures, electrochemically suitable materials like aluminum were taken into account. For the carbon nanotube (CNT) networks, fibrous papers without binder as well as carbon nanotubes, which are connected with a conductive binder, were considered. The most suitable metals for fibers were chosen. Thus, for the bundle-drawn fibers stainless steel fibers are the electrochemically best suitable fibers and are, therefore, not suitable as high-voltage cathode materials.

The summarized data in Table 1 show that a wide range of parameters can be covered with existing technologies. For a large-scale production of metal fibers, the bundle drawing approach from Jenax Inc. seems to be a good candidate. Only the limited electrochemical stability up to 3.8 V compared to Li/Li^+ eliminates the system as a universal current collector system for all types of existing and future active materials.

In this work I propose a possibility to produce fiber-based 3D current collectors which are also suitable for large-scale production. Using a special Melt spinning technique, a wide range of metals and alloys with nearly no limitation can be spun into microfibers. Such fibers cover the whole electrochemical window and all kinds of actual and future active materials can be combined with the 3D fiber-based current collector network. Additionally, the ultra-fast quenching rate during the fiber production process *introduces* special thermodynamic and mechanical properties to the fibers. Especially the unique thermodynamic characteristics of the fibers as well as the mechanical properties typical of nano- and micromaterials underline the relevance of this class of materials. For example, special sintering technologies can be used to produce mechanically stable networks without severe reduction of the surface area of the fiber network compared to single fibers. Furthermore, the pore size of the networks can be tuned quite well using different methods of fiber laying and the networks show a very homogenous pore volume distribution. Therefore, infiltration of the fiber networks with active material is not problematic while the adhesive forces holding the active material on the fibers are very strong due to the large contact area. The proposed approach also opens the path towards ultra-thick batteries: a fiber-based 3D current collector, evenly penetrating the whole electrode volume, can overcome problems like decreasing conductivity for ions and electrons, and strong conductivity gradients within the electrode can be formed. In addition, the mechanical stability of the network/active material system remains high. The enhanced mechanical properties of the fibers and the network in combination with the homogenous pores can decrease the problems caused by delamination of the active material on the current collector, leading to an increased lifetime of the battery, an enhanced tolerance towards increased loading rates as well as an improved overall performance.

Table 1: Comparison between different 3D current collector technologies.

	Pore size adjustability	Electrochemical stability	Mechanical stability	Electrical conductivity	Scale up possibility
Metal foam (gas) [7, 36, 37]	-	+	+	+	-
Metal foam (salt) [7, 36, 37]	+	+	+	+	-
Graphene foam [7, 43]	-	+	-	0	-
3D print [30, 44, 45]	-	+	+	+	0
CNT [7, 33, 46]	0	+	-	0	0
Metal fiber (grown) [7, 19]	-	+	-	+	-
Metal fiber (Jenax, steel) [7, 42]	+	-	+	+	0

In summary, the proposed system allows for the utilization of the advantages of ultra-thick electrodes while at the same time overcoming the known disadvantages with respect to battery performance as well as large-scale production: the feedstock for the network, the metal fibers, are produced with a special Melt spinning technique. Due to the special conditions during the manufacturing of the fibers, they exhibit unique properties that are advantageous for their further applications. The networks formed by the fibers have an extremely large surface area and a defined and homogenous pore volume. Thus, the infiltration of the active material does not pose a big problem and results in an electrode that is evenly penetrated by the current collector over the whole volume. This prevents formation of strong conductivity gradients lancing through the current collector. In conclusion, the whole active material volume can be activated and utilized by the current collector, leading to improved performance, fewer problems caused by delamination, longer battery lifetimes and a formidable gravimetric and volumetric energy density. In the following, the production and the characteristics of these novel electrode materials will be described and discussed in more detail.

2. Materials

2.1. Metalfibers

2.1.2. Melt Spinning

The production method of choice for the microfibers used in this work was Melt Spinning, a method that has been well-known for quite some time for the processing of various materials. The principle of Melt spinning is based on the rapid quenching of molten materials and it is mainly used for meltable polymers and metals, especially for metallic glasses. In principle, molten material is blown through a nozzle onto a fast spinning substrate. Traditionally, this spinning substrate for metal production is a vertically spinning wheel made of a copper alloy due to its good heat transfer and thermal conductivity. By contact with the copper wheel, the melt is quenched with a cooling rate of 10,000 K s^{-1} or more, which actually leads to solidification. The microstructure of such materials is either amorphous or nanocrystalline. Due to the high centrifugal forces induced by the spinning wheel with a rotational speed of 30-70 Hz, the solidified part of the melt is accelerated tangentially from the wheel. Interconnection forces between the liquid and solidified part of the material pull the solid material out of the liquid part into foils, ribbons or fibers depending on the nozzle shape and rotational speed. Here, it is important to mention that the spinning substrate can be made from different materials, however, most important is a high heat conductivity to convey the heat from the melt to the mostly water- or nitrogen-cooled wheel.

The first continuous casting technique for metals was described 1976 by Liebermann and Graham who melted a $Fe_{40}Ni_{40}B_{20}$ alloy by induction and blew it out with pure argon gas on a copper spinning wheel. This resulted in amorphous ribbons with a thickness of around 10 µm to 40 µm. [47] In the 2010s, Spatz et al. (at the Max Planck Institute for Intelligent Systems, Stuttgart, Germany) further developed the Melt spinning method into a production technique for fibers with thicknesses in the lower micrometer range. [48] At the end of the 2010s the same group around Joachim Spatz contributed another important advance in Melt Spinning by replacing the vertical wheel with a horizontal plate. [49]

2.1.3. Copper-Silicon (CuSi)

The CuSi fibers were produced by horizontal Melt spinning and kindly provided by Dr. Sebastian Weber and Louise Kaeswurm, both Max Planck Institute for Medical Research. As raw material, the custom alloys were produced by Wieland-Werke AG Vöhringen. CuSi3 means 3 wt.-% silicon in 97 wt.-% copper, CuSi4 4 wt.-% silicon in 96 wt.-% copper. Table 2 gives the alloy components for the element analysis of CuSi4 provided by the manufacturer. The CuSi3 alloy was produced with the same raw materials, so a similar impurity concentration can be assumed. Thickness and width of the fibers were determined by scanning electron microscopy (SEM). The length of the fibers varies from a few millimeters up to several centimeters. If a special length of the fibers is needed, the fibers were parallelized by carding and cut to the demanded/necessary length.

Table 2: Alloy components of the CuSi4 alloy. [50]

Element	wt.-%	Element	wt.-%	Element	wt.-%	Element	wt.-%
Ag	0,00318	Al	0,00312	Cd	0,00334	Mg	<0,00010
Be	<0,00010	Bi	0,00079	Fe	0,069	Pb	0,00676
Cr	0,00133	Cu	95,752	P	0,00227	Si	4,123
Mn	0,00124	Ni	0,00192	Se	0,00018	Zn	0,01712
S	0,00146	Sb	<0,00010	Ti	0,00025		
Sn	0,00999	Te	<0,00010	B	0,00050		
Zr	0,00053	As	<0,00010	Co	0,00205		

2.1.4. Vitrovac

The Vitrovac fibers were produced by vertical Melt spinning and kindly provided by Dr. Alexandre Micoulet (Max Planck Institute for Medical Research). Vitrovac is a specially designed alloy that forms an amorphous alloy by Melt spinning. As raw material, Vitrovac ribbons from Vacuumschmelze GmbH & Co. KG Hanau were procured and remolten. The nominal composition is $Co_{69}Fe_4Mo_3(Nb,Si,B)_{rest}$. [51] The geometric dimension were determined by SEM and also cut to measure, if needed.

2.2. Battery

2.2.2. Active Materials and Additives

As anode active material, graphite flakes with a median size of 7-10 µm on metal basis with a purity of 99% (Alfa Aesar) were used. As conductivity agent Carbon black (Super P® Conductive, 99+% (metals basis), Alfa Aesar) was used. As binder, Poly-(vinylidenfluorid-*co*-hexafluorpropylen) (PVDF-HFP) was used (Merck). The conductive agent has the function to make the binder electrically conductive while the binder permeates the active material bulk and holds the structure together.

2.2.3. Coin-Cell

As test setup for batteries, stainless steel (SS304) CR2032 coin cells (MTI Corporation) were used together with stainless steel (SS304) wave springs and spacers (MTI Corporation, article number CR20WS). Metallic lithium as precut chips (99.95 %) with 15.6 mm diameter and 0.45 mm thickness was used as anode for half-cell testing (PI-KEM Limited). As electrolyte 1 molar lithiumhexafluorophosphat ($LiPF_6$) solution in EC:DMC 50:50 (ethylene carbonate:dimethyl carbonate) was used (Merk). As separator Whatman® glass fiber filters (934-AH) were used.

2.3. General Chemicals and Gases

Table 3: Used chemicals and Gases.

Chemical	**Manufacturer**	**Purity / %**
Acetone	VWR Chemicals	Reag. Ph.Eur.
Argon	Air Liquide	99.999+
Argon W5 (5 vol.-% H_2 in Ar)	Westfalen AG	-
Nitrogen	Linde gas	Liquid nitrogen

3. Methods

3.1. Mechanical Characterization

Amorphous and nanocrystalline materials are known for their unique mechanical properties. Especially their mechanical properties are notable and easily tunable by different processing steps like heat treatments. During external deformation, two types of distortion are present: the elastic and the plastic deformation. The hardness of the material is strongly influenced by the grain size, so that there is a strong connection to the crystallinity of the material.

The determination of the above established mechanical properties is extremely important as these properties have a great effect on the workability, suitability, and possible application of the materials, especially for materials on the low micrometer scale. Nanoindentation is the method of choice to determine the mechanical properties of micro- and nanomaterials. Here, normally a pyramid-shaped diamond tip is pressed into the sample surface deforming the sample, first elastically then plastically. Due to the pyramidal shape of the tip, the effective projected surface A_c gets larger and the force is growing exponentially. To achieve good measurement results, a higher force is needed to overcome the background noise. However, for micro- and nanomaterials a higher force cannot be achieved by increasing the indentation depth. With flatter tips, the force is growing larger due to an increased contact area between sample and tip. Therefore, the standard tip for Nanoindentation is the flat Berkovich tip with an opening angle of 65.3° between edge and center plane (see Figure 4 c)). [52] The unloading curve can be fitted with the Oliver-Pharr-Method to determine the elastic modulus E_r (reduced modulus) of the sample with equation (1). With the maximum displacement $h_{\max}$ and force $P_{\max}$, the hardness H of the material can additionally be calculated with equation (2):

$$E_r = \frac{S\sqrt{\pi}}{2\beta\sqrt{A_\mathrm{c}}} \tag{1}$$

$$H = \frac{P_\mathrm{max}}{A_\mathrm{c}} \tag{2}$$

Here, S is the contact stiffness and β is a constant which is based on the tip geometry, e.g. $\beta = 1.034$ for a Berkovich tip. [53, 54] Figure 4 illustrates the principles of Nanoindentation and the usually used Berkovich tip. Figure 4 a) shows a typical load displacement curve, Figure 4 b) the material feedback and deformation, and Figure 4 c) a Berkovich tip scheme. While loading, the diamond tip is pressed into the material and the force is growing exponentially. According to equation (2), the maximum force $P_{\max}$ over the projected tip area is the material hardness. The unloading curve is the elastic force pressing against the tip while pulling the tip out of the material. The difference between the origin and h_r is the plastic deformation of the material. Due to the need for accuracy, the displacement is normally piezo-driven, the force feedback about the electromagnetic feedback of a 3-plate capacitor. Here, forces in the Nanonewton range and displacements on the Nanometer scale can be determined. [55-58]

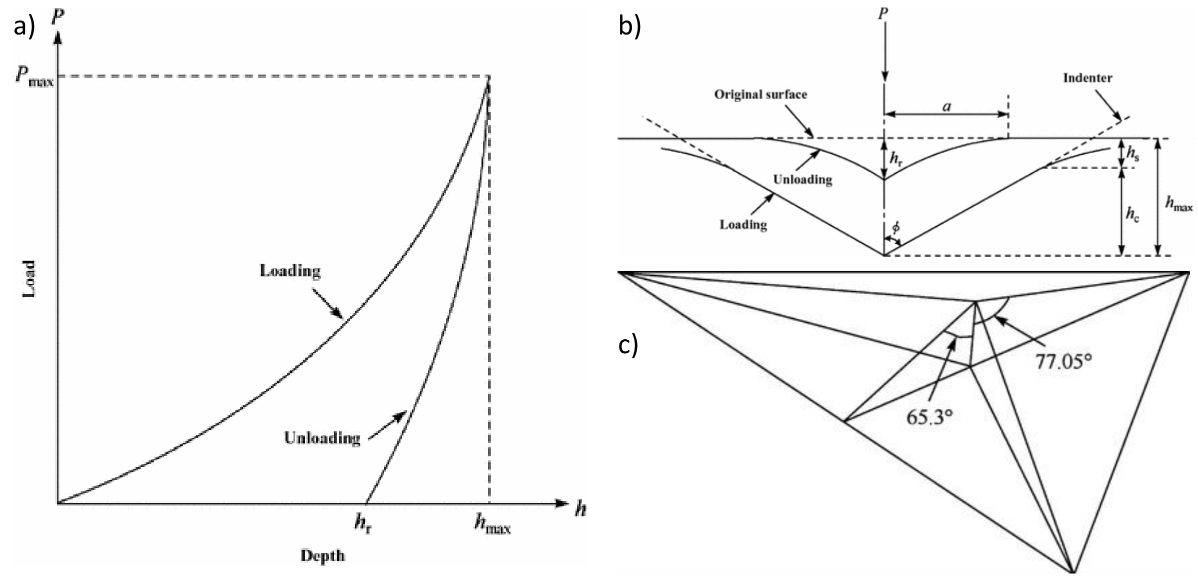

Figure 4: a) Typical load displacement curve of a Nanoindentation experiment, b) the material feedback and deformation and c) the scheme of a Berkovich tip. [55] Adapted and reprinted under permission of Springer Nature (© 2018 Springer Nature)

Elastic deformation describes the reversible deformation of a material by applying an external force. A common measurement technique is the tensile test, where the material is elongated and the force feedback is measured. It can easily be described with the spring model. Here, the atoms are interconnected with a spring with a certain spring force and are elongated or compressed. For elastic deformation, two types of forces must be considered independently of each other. The first type are forces that are perpendicular to the surface like traction and pressure. The second type is shear stress emanating from a force parallel to the surface. This can be described by equation (3) and (4):

$$\frac{F_{\perp}}{q} = E\frac{\Delta l}{l_0} \quad \text{or} \quad \sigma = E\varepsilon \tag{3}$$

$$\frac{F_{\parallel}}{q} = G\frac{\Delta d}{d_0} \quad \text{or} \quad \tau = G\gamma \tag{4}$$

Here, $F_{\perp}$ is the perpendicular and $F_{\parallel}$ the parallel force, q the affected area, l_0 the original length, and Δl the length change, d_0 the original thickness, and Δd the thickness change. From equation 3 and 4 the so-called Hooke's law can be formulated. The normal stress σ is proportional to the elongation ε and interconnected with the elastic modulus E. Similarly, the shear stress τ is proportional to the shearing γ interconnected with the shear modulus G. [59] E and G are material properties and can be evaluated by tensile tests, three-point flexure tests or dynamic mechanical analysis. The macroscopic properties are always based on the microstructure of the material. Shen *et al.* described the change of E and G by lowering the grain size, illustrated for iron in Figure 5. The authors concluded that the intrinsic modulus is fundamentally the same as for larger grain sized materials. At a certain point, the number of atoms which are part of the grain boundaries and their triple junctions in-between are getting larger and the materials properties are changing. [60]

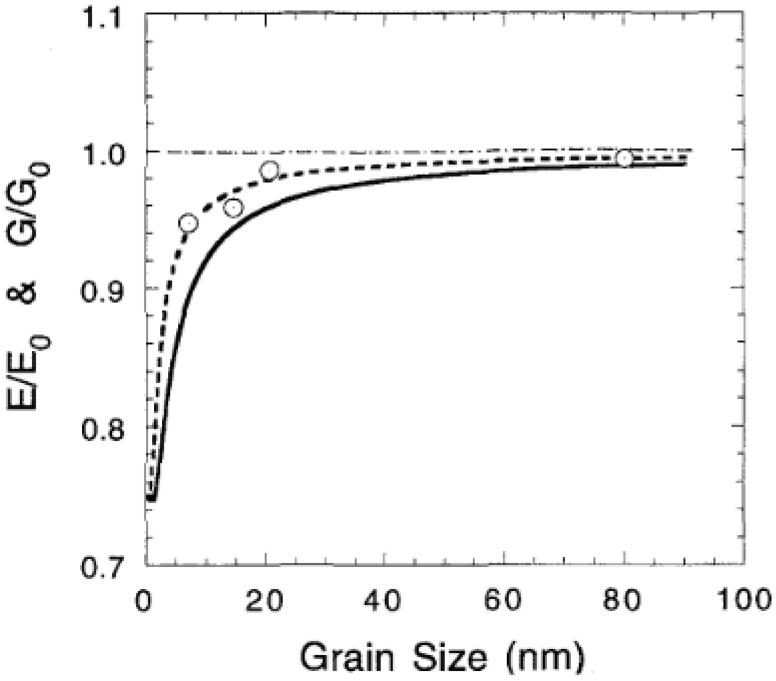

Figure 5: Change of the elastic and shear modulus by lowering the grain size of nanocrystalline materials. The dashed curve represents a grain boundary thickness of 0.5 nm, the solid one for 1 nm. The dashed-dotted line represents the ratio for materials with larger grain sizes. The open circles represent the E/E₀ value of nanocrystalline iron versus the grain size. [60] Reprinted under permission by Springer Nature (© 1995 Springer Nature)

Inelastic properties describe the non-reversible deformation of a material. Whereas for elastic deformation the atomistic connections are just elongated or compressed, for inelastic or plastic deformation the connections are released and reconnected with other atoms which leads to a permanent deformation. Typical of this type of deformation during elongation is necking, i.e. a change in the diameter of the sample with the intention to provide material to the elongating sections before the sample fractures. During compression experiments, like Nanoindentation, folding occurs based on the same principles. A typical mechanism of plastic deformation is the sliding of crystallographic planes towards each other. The crystal structure of solid materials can glide at a certain force against each other to lower the induced stress. This mainly happens over the closed-packed planes inside the structure resulting in slip bands and in single crystals steps on the surface become visible.

Depending on materials properties like ductility, elasticity, plasticity, and viscosity, the hardness describes the mechanical resistance against deformation. Hardness is mainly based on the atomistic microstructure of the material. A very prominent example is the difference between diamond and graphite, although both consist of pure carbon. While graphite has a density of 2.26 g cm^{-3} and a layered hexagonal structure resulting in a low hardness. In contrast, a diamond has one of the most dense lattice structures, resulting in a density of 3.52 g cm^{-3} and is the hardest naturally occurring material on earth. [61] Hardness can be described generally as material feedback against deformation, for example, like pressing an object inside the material, as is the case during Nanoindentation.

However, the hardness of materials is also influenced by the structure of the material and can be adapted by special treatments. A well-known effect for hardening materials is the introduction of defects into the material. At such defect pinpoints, the prominent effects occurring during deformation tend to stack up as their propagation through the material is inhibited. These defects can be on an atomistic level like atomistic vacancies or line defects like dislocations while, for example, precipitations appear on a macroscopic level. Grain boundaries, for example, can be described as an agglomerate of defects between the grains. This leads to energetically more preferable areas with low defect density inside the grains whereas the interconnection in-between the grains has a high density of defects. Here, the propagation of slip planes or dislocations is hindered, hence the deformation of the material needs more energy. Thus, it can be easily understood that materials with small grains are macroscopically harder than materials with big grains due to the higher ratio of grain boundaries per area. This was described by Hall [62] and Petch [63] and can be expressed by the Hall-Petch equation (5):

$$\sigma_{\mathrm{y}} = \sigma_0 + kd^{-1/2} \tag{5}$$

Here, σ_{y} is the yield strength, σ_0 is the stress below which no dislocation movement is present, k is the Hall-Petch slope, and d is the grain size. [59, 64, 65] For some materials, also the inverse Hall-Petch effect is influencing the material properties. It can be explained with the absorption of the atoms and dislocations of grain boundaries. The larger the grain size of the material the larger the number of atoms which must be absorbed before the dislocation is absorbed. Therefore, absorption is less probable for larger grains than for smaller grains. [66] Figure 6 illustrates the relationship between grain size and yield stress. The Hall-Petch slope is positive to around a grain size of 100 nm where it is flattening, at around a grain size of 10 nm the Hall-Petch slope gets negative. This is generally explained by a dislocation pile-up in a grain leading to a stress concentration and, thus, the activation of dislocation sources. [67]

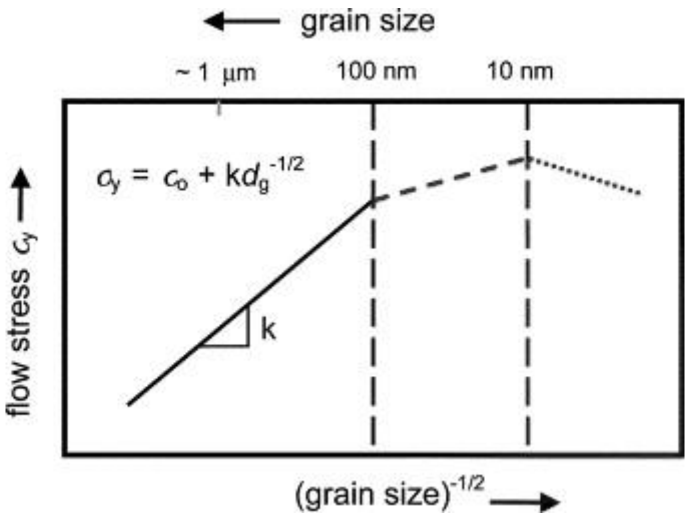

Figure 6: Schematic relationship between grain size and flow stress. [65] Reprinted under permission by Elsevier (© 2003 Elsevier)

For the Nanoindentation (NI) tests, the fibers were parallelized and bundled with adhesive tape. The fiber bundles were then placed upright in a silicone form. A mixture of Aka-Resin liquid epoxy and Aka-Cure slow (Akasel A/S) were prepared according to instructions and poured into the silicone form. The embedding material was cured for 24 h at room temperature followed by 1 h at 110 °C in a drying furnace, both steps were done at ambient atmosphere. Afterwards, the samples were polished with grinding papers of different roughness (P180, P320, P600, P1200, P2400) for 3-5 min per paper, followed by a microfiber cloth (Aka-Napal; Akasel A/S) and grinding particles (DiaDoublo, DiaMaxx, Colloidal Silica; Akasel A/S) for 3-5 min. All steps were performed at a LaboPol-2 (Struers) polishing machine with 250 rpm speed and constant water flow.

The cross-section samples were placed in a Hysitron TI 980 NanoIndenter (Bruker Corporation) on a Performech® 2 Controller. The measurements were performed with a TriboScanner piezo scanner equipped with a standard nanoDMA transducer and a Berkovich tip. A peak force of 1 mN with a loading and unloading rate of 0.1 mN s^{-1} and 2 sec plateau time were used as load function parameters To exclude errors, which can be attributed to drift, a 40-sec drift monitoring with 20-sec drift analysis were performed before every measurement. For the modulus mapping, a maximum force of 200 µN with 1 mN s^{-1} loading and unloading rate, and a spacing of 1 µm were used. All measurements were performed at room temperature and ambient atmosphere in the environmental isolation enclosure of the TI 980 system. Data evaluation was done with the TriboScan software (version 10.2.0.22) and the Indentation Explorer (version 1.00.0.140, provided by Bruker Corporation), part of the Tribo iQ™ package, plugin for Origin Pro (version 9.6.5.169).

The tensile tests were performed on a Bose Electroforce 3200-AT series III equipped with a 22 N load cell. The samples were fixed on both sides with small vices and pulled with a constant displacement rate of 0.03 mm/s to a maximum level of 6 mm. The videos were taken with a Ximea MQ042RG-CM camera.

3.2. Thermodynamic Characterization

While the mechanical properties focus on the behavior of the material when mechanical energy is applied to the material, for example, in the form of stress or strain, the thermodynamic properties describe the stability and energetic balance of the material as well as the behavior when the material is exposed to thermal energy. Fibers produced by Melt spinning are not in a thermodynamically preferred state due to the high quenching rate. Some specially designed materials like Vitrovac [68] or $Fe_{40}N_{40}B_{20}$ [69] are amorphous and often called metallic glasses.

In general, most materials prepared by Melt spinning show a rather small grain size in the nanocrystalline regime as the unordered liquid phase is frozen into a solid state. By heating to the crystallization temperature T_c, the materials flip into a more preferable crystalline phase which, in special cases, can lead to a fundamental change in properties. For this crystallization, an activation energy E_a is needed. With thermal annealing the stored energy, in this case mostly the energy stored in defects, can be released. This energy can be seen as an exothermal peak in differential scanning calorimetry (DSC) measurements.

A way to measure the energetic difference between the untreated, fresh-from-production state and the annealed or crystalline state is the specific heat capacity c_p. The specific heat capacity is defined as the energy per mass which is needed to heat up the material by 1 K. Is the material in a meta- or unstable phase, less energy is needed for heating as the initial state is already energetically elevated compared to the stable state. [70-75] From the specific heat capacity c_p the enthalpy difference ΔH of the system can be calculated by equation (6):

$$\Delta H = \int_{T\mathrm{i}}^{T\mathrm{f}} \left[C_{p,a}(T) - C_{p,g}(T)\right] \mathrm{d}T \tag{6}$$

Here $C_{p,a}$ and $C_{p,g}$ is the specific heat capacity of the glass and annealed state respectively, T_i and T_f is the initial and final state temperature respectively. [75-77] Figure 7 shows these effects in DSC measurements as well as the transmission electron microscopy (TEM) images for the different annealing states. Annealing can increase the glass temperature T_g and the crystallization temperature T_c can be lowered due to the higher degree of crystallization and ordering in the material. The TEM images show this behavior directly. While for the hyper-quenched material almost no ordering is visible, the ordering and, thus, the degree of crystallization is growing. Therefore, less energy is stored which can be released and the exothermal curvature of the differential scanning calorimetry (DSC) is lower and shifted towards higher temperatures. [71]

The typical measurement method is DSC. Here, the sample is placed in a crucible and is heated together with an empty reference crucible. If an exo- or endothermal reaction of the sample occurs during the thermal treatment, a temperature difference between the crucibles can be measured. Combining this information with known calibration values, the reaction energy can be determined. [78]

Thermal conductivity (see equation (7)) and thermal diffusivity (see equation (8)) are significant for the quenching of materials. As shown in the equations below, the thermal conductivity coefficient λ is depending on the heat flow rate Q, the contact area A, the thickness l, and the temperature difference ΔT, and describes the heat transfer trough a material. Using the thermal conductivity coefficient λ, the heat diffusion α can be calculated with the specific heat capacity c_p and the material density ρ. It describes the time-dependent change of the heat transfer due to a temperature gradient. [78]

$$\lambda = \frac{Q \cdot l}{A \cdot \Delta T} \tag{7}$$

$$\alpha = \frac{\lambda}{\rho \cdot c_p} \tag{8}$$

Two systems for DSC measurements were used in this work. For measurements of the melting temperature, and all measurements above 600 °C, a STA 449 F3 system (Netzsch-Gerätebau GmbH) with a silicon carbide furnace and a TG-DSC sample holder system with type S thermocouple were used. Before the measurement, the sample chamber was evacuated three times and flushed with pure argon gas. To remove remaining oxygen and moisture from the gas, an oxygen trapping system (Netzsch-Gerätebau GmbH) made of a zirconium ring was used. The samples were cut into parts with a length of 1-2 mm and pressed in the bottom of an 85 µl-aluminum oxide crucible (THEPRO GbR) with a pierced lid. For the measurements a constant argon gas flow of 50 ml min^{-1} working gas and 25 ml min^{-1} protective gas was used. Data evaluation was performed with Proteus® Analysis (version 8.0.1, Netzsch-Gerätebau GmbH).

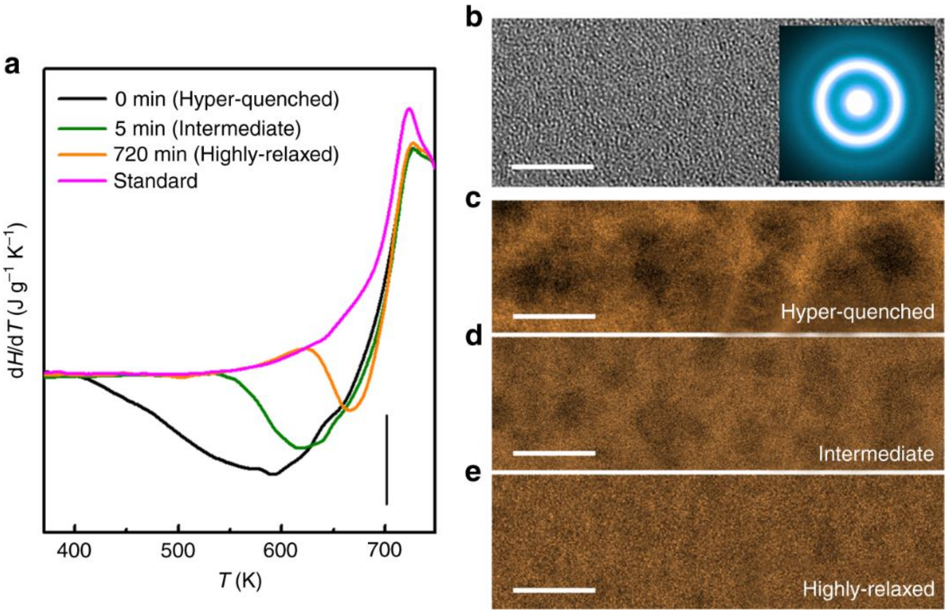

Figure 7: Metallic glass in different thermodynamic states. a) the heat flow DSC measurements for a fast quenched material that was annealed at ~0.8 T_g *for 0 min, 5 min and 720 min or not fast quenched as standard, including b) TEM measurements and as insert the electron diffraction pattern for the hyper-quenched material and the dark field TEM images of c) the hyper-quenched, d) intermediate and e) highly relaxed states.[70] Reprinted under the Creative Commons Attribution 4.0 International License permission (© 2018 the Authors. Published by Springer Nature)*

For measurements of the specific heat capacity and annealing experiments below 600 °C, a DSC 214 system was used. The system was equipped with an Intracooler IC40 systems for defined cooling, an Arena® silver furnace and a Corona® sensor (Netzsch-Gerätebau GmbH). The measurements were performed under constant nitrogen flow (60 ml min^{-1} working gas, 40 ml min^{-1} protective gas). The samples were cut into a length of 1-2 mm and placed in Concavus® crucibles (Netzsch-Gerätebau

GmbH), which were closed with a pressing system to prevent sample movement and guarantees good thermal contact to the crucible and sensor. Data evaluation was performed with Proteus® Analysis (version 8.0.2, Netzsch-Gerätebau GmbH). The specific heat capacity was calculated from the sample DSC results and a sapphire reference scan for sensitivity calibration according to the ratio method. [78]

3.3. Crystallographic Characterization

The crystallographic properties in materials are mainly dominated by two properties, i) the material composition and ii) the cooling rate. The material composition and the resulting crystal phases can be expressed in a phase diagram. The phase diagram of the copper-silicon system is given in Figure 8. Here, the compositions of CuSi3 (3 wt.-% silicon in 97 wt.-% copper) and CuSi4 (4 wt.-% silicon in 96 wt.-% copper) are marked as red lines. Super-fast quenching, as happens for example during the Melt spinning process, freezes the liquid phase of the material into a solid phase. Therefore, the solid phase has the same crystal structure as the liquid phase and an amorphous metallic glass is formed.

However, if the quenching process is too slow, the atoms have sufficient time to form a thermodynamically more preferable crystalline phase and structure. For slower quenching rates, the atoms tend to grow to larger grains compared to fast quenching rates as more time is available to form larger crystallites. This can be described by the grain growth which is time and temperature dependent. The grains continue to grow as long as the temperature exceeds the activation energy which itself is temperature controlled. If the cooling is slow enough, the composition follows in this more or less theoretical case the liquidus line of the phase diagram, so that first one component (component A) of the alloy starts to crystallize. Thus, the composition of the melt changes due to the reduced portion of component A inside the melt until a minimum of the line, e.g. an eutectic point, is reached. If a minimum is reached and the melt is cooled down further, the melt will start to solidify without further impoverishment of component A. Furthermore, the remaining melt will solidify according to the stable phases depicted in the phase diagram for the alloy composition considered. [79-81]

Materials build their crystals randomly in every direction during cooling which is called isotropic growth. If there is an external influence like mechanical forces, strong temperature gradients or electromagnetic forces, the crystals tend to grow preferably into a special direction, called anisotropic growth. These preferred grain orientations can change the properties of the material. If the material is annealed or recrystallized, the degree of orientation is reduced until it is removed completely. The lowering of thermodynamic energy of the whole system is, therefore, the driving force. Annealing describes processes in materials that lower the defect concentration by movement of defects and thereby reducing the internal energy and stresses to a more preferred thermodynamic state.

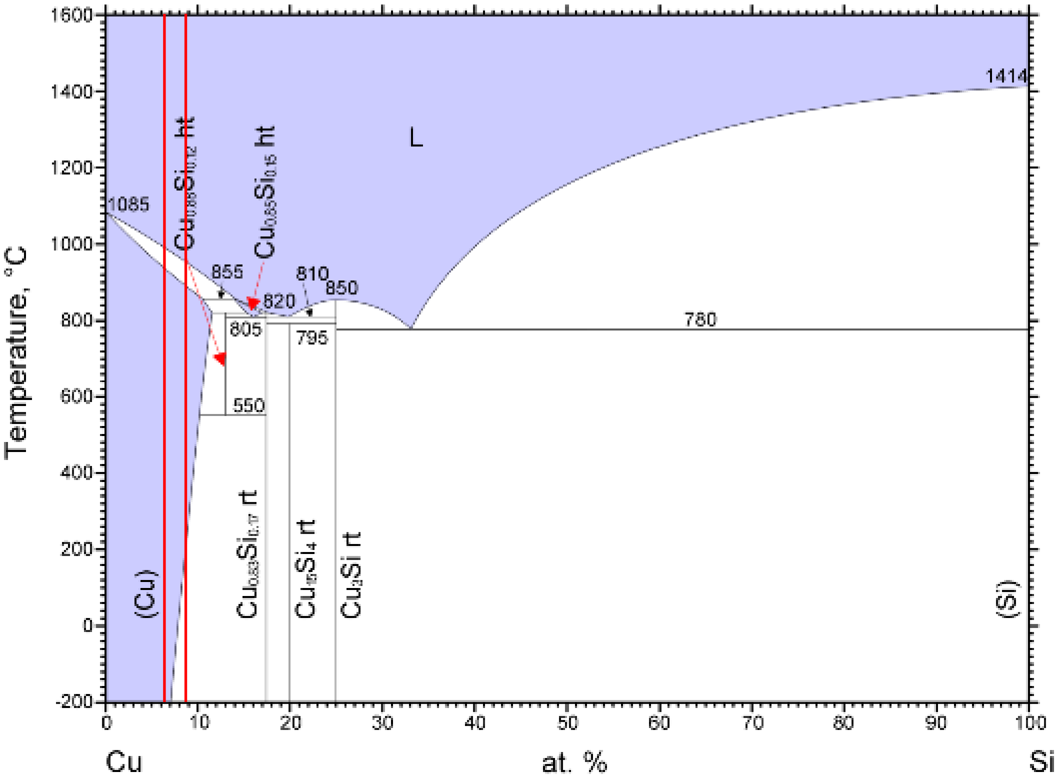

Figure 8: Phase diagram of the copper-silicon system. The red lines indicated the CuSi3 (left) and CuSi4 (right) composition. [82, 83] Reprinted under permission of Elsevier and Springer Materials, original data provided by [82], graphical work by [83] (© 2016 Springer Materials)

However, the original crystal structure remains intact when the temperature stays under the recrystallization temperature. While this process already sets in at relatively low temperatures, a recrystallization of the material occurs at higher temperatures. Here, the atomic lattice is fundamentally reconstructed to a new, energetically more preferential crystal structure. [59, 71, 80]

The standard method for evaluating the crystallographic properties is X-Ray Diffraction (XRD). Here, the electrons of the atomic layers in the crystal structure diffract a focused X-ray beam. Depending on the lattice plane distance, the conditions for constructive interference are fulfilled at certain angles of incidence. In 1913 William Lawrence Bragg expressed with his equation (9) the connection between the X-ray wavelength λ, the angle to the lattice plane θ, and the distance d in-between the lattice planes:

$$n\lambda = 2d \sin\theta \tag{9}$$

Here, n is the grade of the investigated diffraction maxima and is a natural number. [84] The Laue indices can be derived from peak position, intensity and number of the crystal constants of the unit cell. This information is unique for every crystal structure and can be used for structural identification. The intensity of the diffraction peaks helps to identify the degree of a crystal orientation due to the proportionality of the intensity to the structure factor. This factor is the Fourier transform of the electron density and describes all waves that are diffracted in one crystallographic direction. It is, thereby, possible to illustrate these preferred orientations with XRD pole figures. Therefore, the X-ray beam is set to an angle θ (crystallographic orientation O) where a diffraction peak is visible on the common 2θ- diffraction-scan. By rotating the sample along two angles φ and ω, the angle of the preferred crystal structure to the surface can be determined. At a certain angle φ and ω, a higher intensity is measured which can be translated into the orientation distribution function and illustrated as a pole figure. [59, 81, 85] The measurement setup is shown schematically in Figure 9.

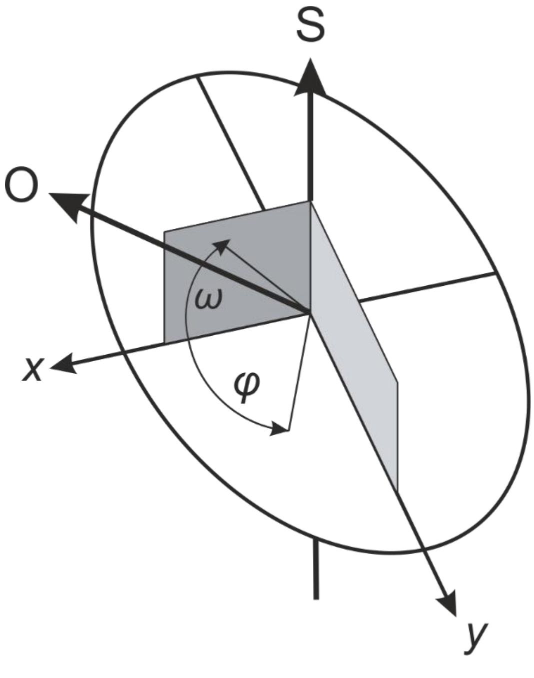

Figure 9: Scheme of the pole figure measurement setup with the sample axis S, the crystallographic orientation O and the measurement angles φ and ω.

The crystallographic analysis was performed with a Bruker AXS D8-Discover DaVinci. Either a copper or cobalt-sealed tube anode was used for the measurements. The 2θ scans were done with line focus through a Göbel mirror and an 0.2 mm slit on the sample. The diffracted beam was detected on a Bruker AXS LYNXEye 1D detector. For this several fibers were fixed on a silicon wafer highly oriented in the (911) direction without an own peak in the measurement range. The measurement range was

20-120° 2θ with a step size of 0.04° for copper radiation scans and 20-100° with a 0.1° step size for cobalt radiation scans. For the pole figure scans, the fibers were fixed parallelly with double-sided tape on a glass slide, the measurement angle was in line with the fibers. For these measurements, the X-ray beam was point focused trough a PolyCap and a 2 mm-snout on the sample. After the sample, a scintillation counter measured the beam after a parallel plate collimator. Here, a φ step size of 3° (0-360°) and a ω step size of 2° (0-88°) with a scan time of 4 s per step was used.

3.4. Structural and in-situ Sintering Characterization

A Zeiss Ultra 55 scanning electron microscope was used with 3 kV acceleration voltage for structural characterization. The fibers were fixed with double-sided conductive carbon tape on the sample holder. The cross-section samples were also fixed with double-sided conductive carbon tape stripes on the sample holder. The double sided tape was led up to the top of the sample to provide good electric conductivity. Here, a 6-nm thick layer of carbon was coated on top.

For the in-situ sintering experiments, the SEM was equipped with a 1050 °C heating module (Kammrath & Weiss GmbH). In order to fix the sample inside the heat stage, the fibers were placed on a soft carbon plate and covered with another plate with a hole in the middle through which the sample can be observed. This setup was placed inside the heat stage and pressed down with a tantalum frame to prevent detaching of the sample. 10 K s^{-1} was chosen as heating rate.

3.5. Electrode and Battery Production

3.5.1 Network Production

Permanent connection between the fibers is achieved by sintering, a thermally activated diffusion-driven process. Diffusion describes the particle movement in materials to balance out concentration differences. In 1855 Adolf Fick described the diffusion processes with his famous equations. His first law (equation (10)) describes the velocity of the particle movement in a certain direction and the second law equation (equation(11)) describes the concentration change as a function over time:

$$J = -D\frac{\partial c}{\partial x} \tag{10}$$

$$\frac{\partial c}{\partial t} = -D\frac{\partial^2 c}{\partial x^2} \tag{11}$$

Here, J is the diffusion flux in one direction, D the diffusion coefficient, c the concentration, x the length, and t the time. [86] With the self-diffusion coefficient D_0 the diffusion coefficient can be calculated by equation (12):

$$D = D_0 exp\left(-\frac{E_\mathrm{a}}{RT}\right) \tag{12}$$

Here, R is the universal gas constant of R = 8.314 J mol^{-1} K^{-1} and T the absolute temperature. The self - diffusion coefficient D_0 is a material specific parameter and can be calculated and determined experimentally. In solid materials, diffusion can be described as the movement from one crystallographic lattice position to another. The self-diffusion coefficient can be expressed by the interatomic distance, the jumping frequency, and the amount of vacant lattice positions. For this processes, an activation energy E_a must be overcome. This can be achieved in a classic way by thermal excitation or by other external influences such as pressure.

To determine the diffusion coefficient experimentally, several different determination methods are possible. One of the most famous and most used is the Matano method, first presented by Chujiro Matano in 1933. [87] Here, two materials are brought into contact with each other and thermally treated for a certain time. Between both materials, an interfacial area is formed with a material concentration gradient. The Matano plane describes the plane in the interfacial area with equal amounts of material on both sides. Hence, the diffusion coefficient can be calculated from the slope of the gradient at the Matano plane. Figure 10 a) shows a scheme of the Boltzmann-Matano method and b) an experimental illustration. By this method, the diffusion coefficient can be determined experimentally. [80, 88]

In a system with similar materials, the determination of the element gradient is not possible. However, if a visible interfacial area is present, the diffusion coefficient can be determined by time and temperature variations. With known time, the width of the interfacial area can be measured and the diffusion coefficient calculated by equation (13):

$$D = \frac{\langle x^2 \rangle}{2t} \tag{13}$$

It is important to note, that the movement length x is the half of the interfacial area width, i.e. the distance of one material to the former contact plane, while t is the time. By determining the diffusion coefficient for several temperatures, the resulting diffusion coefficient can be plotted as an Arrhenius plot. Here, the slope of the resulting fit can be used to calculate the activation energy E_a and the self-diffusion coefficient D_0 according to equation (7). [88, 89]

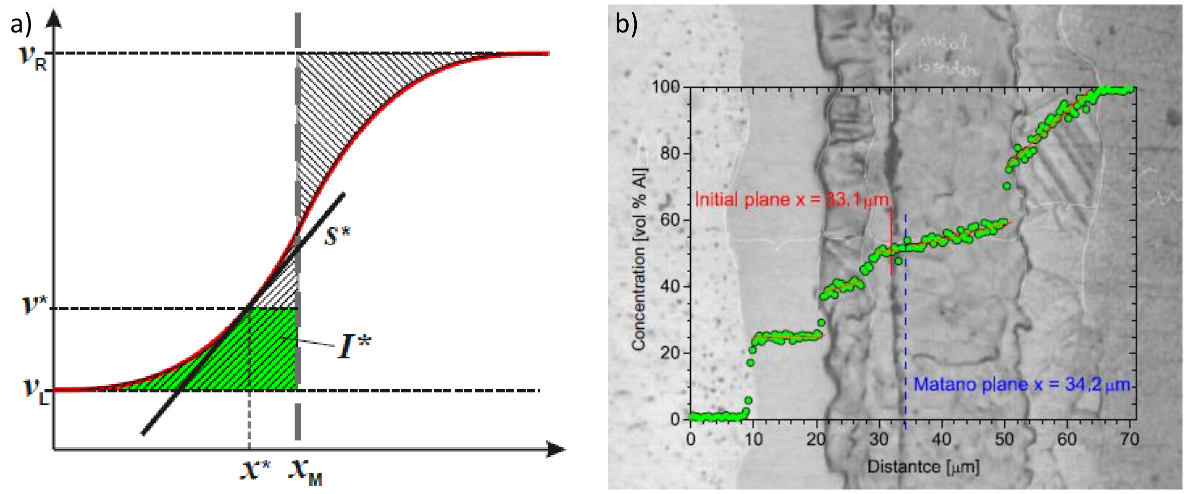

Figure 10: a) Scheme of the Boltzmann-Matano method and b) the electron microscopy (SEM) picture of the cross-section of an aluminum and copper experiment, the concentration (green dots) are determined by energy-dispersive spectroscopy (EDX). [88] Adapted and reprinted under permission by Elsevier (© 2014 Elsevier)

The process of sintering is mostly known for ceramics; however, the term generally describes a thermally activated densification method driven by the reduction of the free enthalpy ΔG of the system due to surface reduction. For ceramics, a powdery raw material is pressed into green bodies without a permanent mechanical interconnection. During the sintering process single particles form a mechanical interconnection by a diffusion-driven exothermal process. Diffusion can happen inside the material bulk, i.e. volume diffusion, across the material surface, i.e. surface diffusion, and in special cases also through evaporation and condensation or for liquid phase sintering also through dissolving and deposition. [90]

The change in free enthalpy during the sintering process can be divided into three parts; the surface part ΔG_S, the volume part ΔG_V, and the grain boundary part ΔG_B. However, during sintering the volume stays nearly constant while the surface is reduced and new grain boundaries are formed. Therefore, the surface fraction ΔG_S is much larger than the grain boundary fraction ΔG_B which results in a negative ΔG_T for the whole process, so that the sintering runs by itself as long as the systems stays over the activation energy barrier. This can all be described with equation (14):

$$\Delta G_{\mathrm{T}} = \underbrace{\Delta G_{\mathrm{V}}}_{=0} + \underbrace{\Delta G_{\mathrm{B}}}_{>0} + \underbrace{\Delta G_{\mathrm{S}}}_{<0} \tag{14}$$

Due to the capillary pressure between two particles, particle movement is directed towards the contact area leading to the formation of sintering necks. The sintering process works below the melting point T_{m}, normally at 75-95% T_{m}, and is diffusion driven. As described in equation (12), an activation energy E_{a} is needed which is normally given by thermal excitation. Thus, the principle shape of the green body can be preserved while a permanent mechanical connection in between the particles is formed. [80, 90]

In order to produce networks for the current collector production, the fibers were first carded with a 2-speed drum carding machine (Ashford) to lay a first network with relatively strong parallel fibers. For the experiments with a carded network, they were directly transferred to a graphite plate. For experiments with dispersed fibers, the carded networks were cut to shorten the fibers to a certain length, depending on the experiment. After cutting the fibers, the short fibers were singularized and dispersed afterwards in a vacuum filtration apparatus.

By stirring, the fibers were homogenized and the dispersing medium was drained afterwards. The fiber fleece was collected on a polymer network and transferred to a graphite plate for sintering. The fleeces were sintered on the graphite plate with small titanium plates as space holders in a protective gas furnace (Carbolite Gero, CWF 12-65 with a retort A105). The furnace was evacuated three times and flushed with pure argon gas. During the experiment, a 1:1 mixture of argon and Ar-W5 was used to flush the chamber with 7 l/min. As sintering temperature, a temperature of 960 °C was chosen with a peak holding time of 1 h and a heating rate of 10 K min^{-1}, followed by a natural cooling of the furnace.

An infrared furnace (MILA-5000, Ulvac) was used for super-fast sintering. Here, the loose fibers were placed on the quartz glass sample carrier. The furnace was evacuated three times to remove oxygen and flushed with around 0.5 bar argon in between. For the sintering process, a flushing argon atmosphere of 50 mbar was used. 1 min was set as heating time for all experiments so that the variation of the heating rate is kept as small as possible.

For pressure-assisted low-temperature sintering, a heatable uniaxial press (PW 100, Paul Weber Maschinen- u. Apparatebau) was used. The heat plates were heated first to working temperature before the network, placed between two highly polished steel plates (Thermax 1.4841), was introduced into the press. After around 2 min preheating of the sample sandwich, the working pressure was set and held for the time of the experiment. The sample sandwich was extracted immediately afterwards and the network was removed from the steel plates in its hot state.

3.5.2. Electrode Fabrication

For the fabrication of electrodes, the sintered networks were first coated with active material by doctor blading with a graphite slurry containing 85 wt.-% graphite flakes, 10 wt.-% PVDF-HFP, and 5 wt.-% Carbon Black. Then, the PVDF-HFP was dissolved in acetone while being stirred at room temperature. Dry graphite and Carbon Black were subsequently added to the solution and dispersed for 10 min at 9000 rpm (IKA, T25 easy clean digital with dispersing tool S25N-25G). The network was placed on an automatic film applicator with a heated vacuum bed (Thierry) and doctor bladed with an adjustable film applicator (Thierry). Afterwards, the coated network was dried at room temperature in a fume hood. In some cases, the electrodes were subsequently compressed with a hot rolling press MSK-HRP-04B (MTI Corporation) at 160 °C.

3.5.3. Coin-Cell Production

For the assembly of coin cells, plates with a diameter of 14 mm were punched out of the electrode and transferred in an argon filled glovebox (Labmaster SP, MBraun). In the negative case of the coin cell, the lithium plates were first placed in the middle followed by a separator. The separators were soaked with five drops of electrolyte before the electrodes were centrally placed on it. Depending on the porosity and thickness of the sample, up to ten additional drops of electrolyte were added until the electrolyte was no longer soaked up. Spacer and spring were placed on top, followed by the positive case. Finally, the coin cells were closed with a hydraulic crimping machine (Nanografi Nanotechnology).

3.6. Electrochemical Characterization

Several electrochemical processes inside the cell drive lithium ion batteries. One of the most important characterization methods for electrochemical cells is electrochemical impedance spectroscopy (EIS). It is typically used to measure different types of resistances and diffusion inside the battery. Figure 11 shows a scheme of a Nyquist plot obtained by EIS of a half-cell and the equivalent circuit model. With equation (15) the equivalent circuit can be fitted. R_1 represents the contact resistance inside the cell, C_2 a double-layer capacitor, R_2 the charge transfer resistance, and W_3 the Warburg element with the Warburg coefficient σ_3, representing diffusion. The impedance Z is a function of the frequency f and is not only a valid method for the determination of the cell parameters, the change of these cell characteristics can give information about aging and the current state of the cell. [91-94]

$$Z(f) = R_1 + \frac{R_2}{1 + i2\pi f R_2 C_2} + \frac{\sqrt{2}\sigma_3}{\sqrt{i2\pi f}} \tag{15}$$

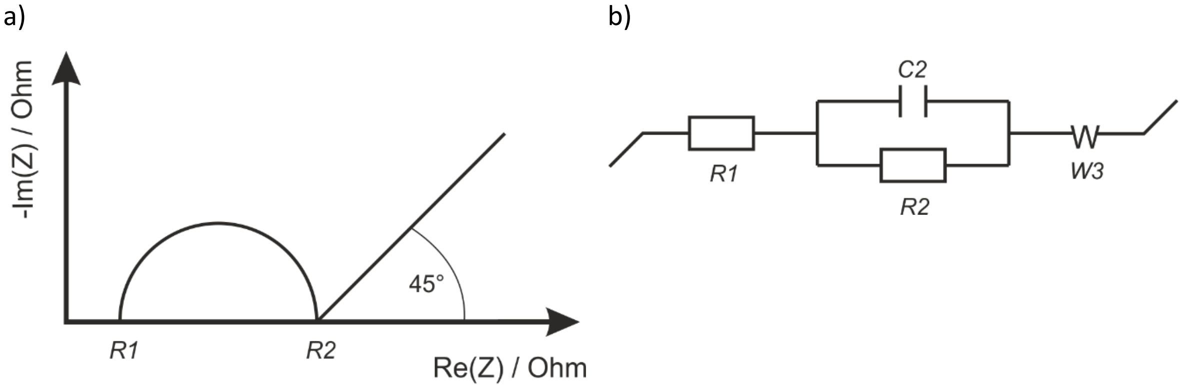

Figure 11: a) Impedance scheme of a half-cell an b) the associated equivalent circuit.

The electrochemical testing was performed on a multichannel potentiostat VMP-300 (Bio-Logic Science Instruments GmbH). The electrochemical stability testing was performed with constant voltage (CV) measurements with a scan rate of 1 mV/s to 0-2.2 V. The battery cycling experiments were done with constant current (CC). The current was set depending on the loading rate and capacity of the electrodes. 0.012 V was chosen as lower and 2.2 V as upper cut-off criteria. The capacity was determined with a battery capacity determination (BCD) function, containing CC loading until 2.2 V and followed by a CV step with 10% of the initial current as cut-off criteria for loading, continued with CC unloading. A scanning range from 10 mHz up to 200 kHz with ten points per decade and a sinus amplitude of 10 mV was chosen for EIS measurements.

The 4-point measurements were performed at a Keithley source meter (2612A) with linear contacts of 2 mm length and a distance between the measurement contacts of 20 mm. The outer two electrodes had a distance of 10 mm to the inner ones. To ensure that there is good electrical contact with the network, the electrodes were pressed on the fibers or network by carefully pushing them down by hand.

3.7. Thermal Treatment

Thermal treatments of the fibers were performed with a tube furnace (SR 70-500, Gero). The samples were placed in an alumina crucible and heated in a 1:1 mixture of argon and argon W5. The heating rate was always set to 10 K/min with 1 h holding time and followed by natural cooling. The holding temperatures for all materials are shown in Table 4.

Table 4: Thermal treatment operation temperature.

Material	Annealing Temperature / °C	Recrystallization/ Crystallization Temperature / °C
CuSi3	300	980
CuSi4	300	980
Vitrovac	300	600

4. Results and Discussion

4.1. Fibers

The crystallographic, thermodynamic, and mechanical properties of the single fibers are experimentally analyzed and discussed.

4.1.1. Crystallographic Properties

The crystal structure is one of the most influential parameters of material properties. Depending on the composition of the material, cooling rate, production, and further treatments, the crystal structure can be tuned to obtain special characteristics. In the present work two similar, yet different, copper-silicon alloys were investigated. As marked in the phase diagram shown in Figure 8, first the melting point is lowered by adding more silicon into the CuSi3 (T_m = 1003 °C) alloy to obtain CuSi4 (T_m = 965 °C). [82, 83] The next notable difference is that the CuSi3 alloy ends in the copper-type region. Here, the silicon atoms are located on interstitial positions of the face-centered cubic (fcc) ($\mathrm{Fm\overline{3}m}$) crystal structure. [95-97] The melt is directly frozen in the liquid state by rapid quenching and the normal solidification and hence crystallization pathways do not exist.

The CuSi4 alloy differs in this regard. If we follow the material composition line from liquid towards room temperature, we end in the two-phase region, i. e. a mixed composition of the fcc copper with interstitial silicon and the $Cu_{0.83}Si_{0.17}$ phase ($\mathrm{P4_132}$). [98] After the melt spinning process, the quenched liquid is present as a metastable single phase, where the copper phase is overloaded with silicon. If the material is treated further, for example with heat, the structure frozen in a metastable state is driven towards a thermodynamically more stable condition, which is why the material splits into the two phases described above.

In a thermodynamic consideration From a thermodynamic view, a secondary phase or precipitation is formed in a region with lower crystallographic perfection, for example, at grain boundaries or at the material's surface. This process is diffusion driven, meaning it is dependent on time and temperature. In a first step, the secondary phase develops in the grain boundary region and is moving towards the surface for longer treatment times. To speed up this process, a higher temperature is needed. [79, 80, 99, 100] Figure 12 shows the thermally annealed CuSi4 alloy. The formerly smooth surface now shows deep surface cracks at the grain boundary region as well as grown crystals on the material surface. Through these cracks at the grain boundaries, the secondary phase is diffusing towards the surface and the silicon content in the copper phase in the bulk is decreasing until a stable composition is reached. In this case, the $Cu_{0.83}Si_{0.17}$ precipitation is relatively brittle compared to the copper phase.

These brittle phases at the grain boundary reduce the resistance against elastic deformation for the whole material.

XRD studies were performed to investigate the crystal structure of the fibers. The resulting pattern is typical for a crystalline sample. It seems that the cooling rate during melt spinning is too low for this system to produce an amorphous or nanocrystalline material, which is in general only possible for pure metals. [101] Figure 13 a) shows the XRD pattern of the CuSi3 fibers without any treatment (red line), with thermal treatment (black line), and the reference pattern for fcc copper (blue line) [102]. For better visualization, the reference pattern was turned negative and the measured pattern shifted along the y-axis.

For an ideal sample, the (111) peak at 43.6 ° should be around double the height of the (200) peak at 50.8 °, which in turn is around double the height of the (220) peak (at 74.7 °) and the (311) peak (at 90.7 °). The (111) and (200) peaks for CuSi3 and the (111), (200), and (311) peaks for CuSi4 will be discussed in detail in the following.

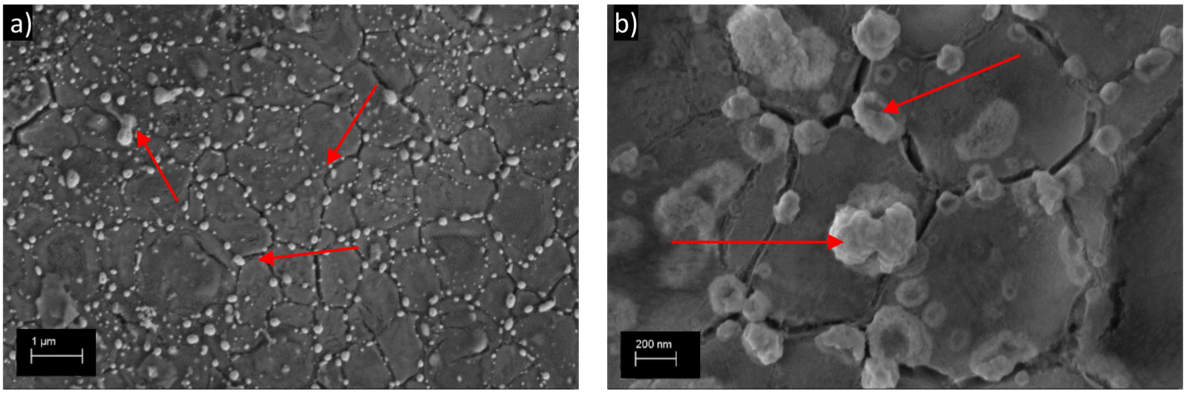

Figure 12: Thermally annealed CuSi4 fibers with $Cu_{0.83}Si_{0.17}$ *precipitations. Some of the precipitations are marked with red arrows.*

For the untreated CuSi3 sample, the (111) and (200) peaks are approximately at the same height. Every peak represents a crystallographic plane, parallel to the surface. If one plane is *overrepresented/occurs more often* compared to other planes, the associated peak has a higher intensity. This effect is known as preferred orientation, therefore a (200)-plane preferred orientation is visible here. The case is different for the thermally treated sample. Here, the (200) peak is very low like all other peaks, except the (111) peak. During thermal treatment, the fibers change from an (200) orientation towards a (111) orientation. This can be explained by the recrystallization process during thermal treatment. As the whole crystal structure is rebuild towards a thermodynamically more preferred phase, the Gibbs energy is lowered. During the recrystallization process, a nucleation, mainly at the grain boundaries, is present at first. Hence, these nuclei can be described as compromise phases of the surrounding material. Additionally, these nuclei are growing at a special growth rate and in the first step form a material with smaller grains than before. However, the grains continue to grow and start combining with their neighboring grains. However, the orientations of the combining grains must be similar in order to eliminate the formation of new grain boundaries. The new orientation is influenced by the macroscopic materials structure, the former orientation, and possible external stresses during recrystallization. [80, 103-109] If the process would continue infinitely, a single crystal could be formed.

In comparison to Figure 13 a), Figure 13 b) shows the XRD pattern for CuSi4 fibers, also for an untreated sample (red line), a thermally treated (black line), and the reference pattern for fcc copper [102] (blue line) visualized with the same conventions as in Figure 13 a). Here, a (200) orientation is visible for the untreated sample, a little weaker as for the CuSi3 sample but still visible. In contrast to the strong (111) orientation of the CuSi3 sample, a strong (311) orientation is present here. The main difference between both samples is the different silicon fraction. While for the CuSi3 sample, no precipitation is expected and also not visible on SEM images, for the CuSi4 sample, a surface and grain boundary precipitation is present as discussed. It seems that these precipitations change the grain orientation during recrystallization. On the XRD pattern, neither the $Cu_{0.83}Si_{0.17}$ phase is visible nor another phase. The reason for this is the small fraction of just around 4 at.-% in the material which results in peaks smaller than the background noise of the instrument. Additionally, only the surface crystals can be measured by XRD and the grain boundary precipitation is perpendicular to the surface. Therefore, it’s visualization is not possible due to the lack of X-ray penetration. [80, 81]

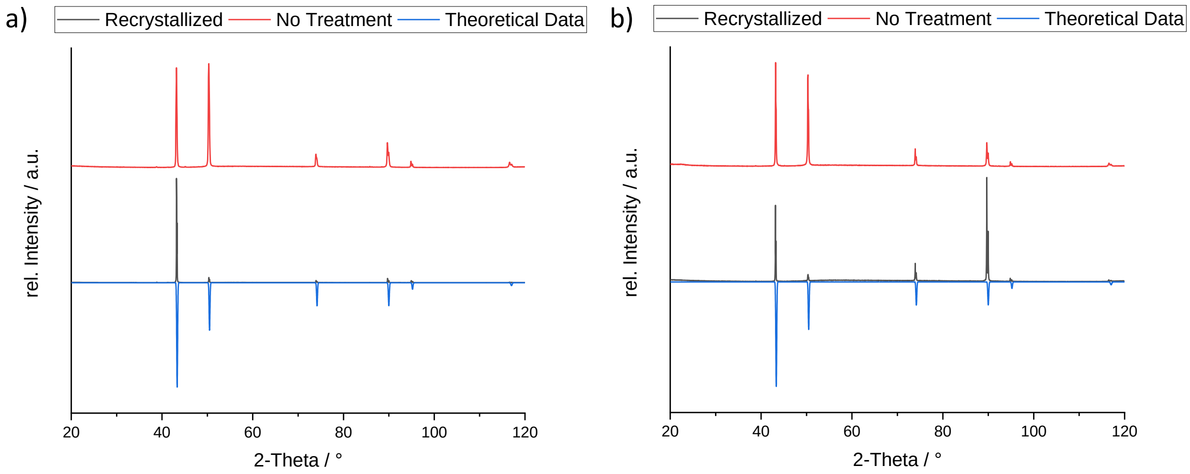

Figure 13: XRD pattern of a) CuSi3 and b) CuSi4 fibers with and without thermal treatment and the simulated fcc copper reference pattern [102].

Pole figure measurements were performed to further investigate the preferred orientation of the fibers. Therefore, two types of CuSi3 fibers with different widths were measured first as a normal scan, then as a pole figure on the two main peaks (111) and (200). The smaller fibers had a width of around 30 µm, the bigger ones around 90 µm. Figure 14 shows the XRD patterns for both samples for untreated (black line), annealed (red line), and recrystallized (blue line) fibers as well as the simulated data for fcc copper [102] (green line). For the 90 µm fibers, the processes discussed above are present. In this case, annealed fibers were added to the investigation. In contrast to the recrystallized samples, no fundamental change of the crystal structure occurs. Only structural defects are moving towards grain boundaries to decrease the intrinsic free energy. Therefore, no change in the orientation is expected and only a small change within the measurement accuracy is visible.

For the 30 µm fibers, the strong (200) orientation is not as pronounced in the untreated sample as for the 90 µm sample. For the annealed sample, the (200) orientation is again as strong as expected. As discussed, no fundamental change of the crystal structure takes place during annealing, therefore the weaker (200) orientation for the untreated sample must be attributed to measurement accuracy and preparation. For both fiber sizes, the dominant (111) orientation appears for the recrystallized sample.

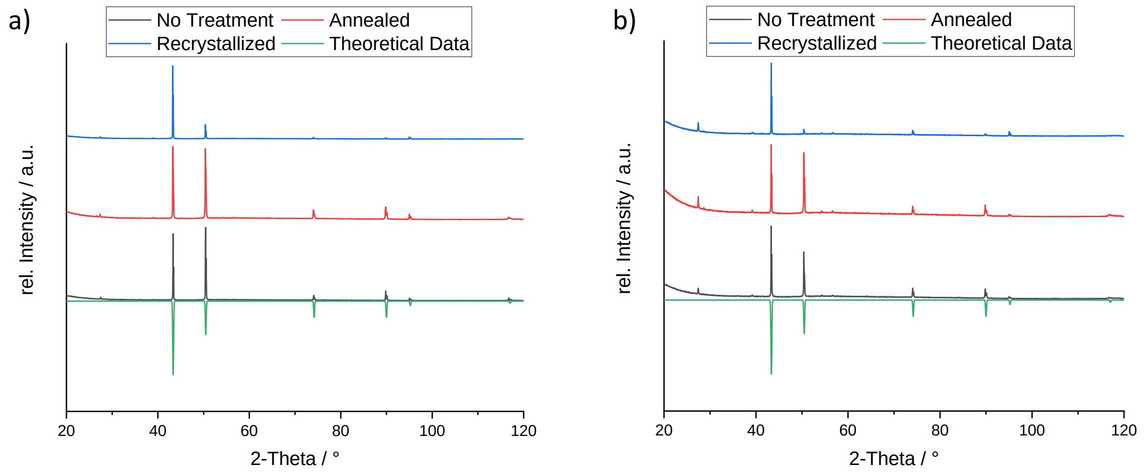

Figure 14: XRD pattern of annealed, recrystallized, and untreated a) 30 µm and b) 90 µm CuSi3 fibers as well as the simulated fcc copper pattern [102].

Figure 15 shows the measured (111) and (200) pole figures for the 30 µm CuSi3 fibers. In an ideal pole figure, the focused peak is just visible as a single point at a certain position. The specific position is given by the stereographic projection of the corresponding crystal structure. Under certain rotational angles φ and ω of the sample, the crystallographic plane parallel to the surface fulfills the Bragg equation (9) and a diffraction is measurable, representing an increased intensity in the pole figure. If no peak is visible, no preferred orientation is visible at this position. Compared with typical measurements the surface of the sample here is not flat due to the surface curvature of the melt spinning fibers. If we focus first on the (111) scans, four intensities at φ = 0°; 90°; 180°; 270° and ω = 54.74 ° are visible for the untreated sample. These correspond to the 4-symetrical (111) peaks of a cubic crystal structure. At all other positions, the intensity is unequal to zero, which means no total (111) orientation is present in the fibers. The surface curvature of the samples may also be another reason for this effect. For the annealed sample only two peaks are visible, the surrounding areas show the same values as for the untreated sample, unequal to zero. A big difference is visible in the case of the recrystallized sample. Here, nearly the whole pole figure is at a relatively low intensity. This also supports the aforementioned crystallographic changes during recrystallization and the decrease/reduction of the preferred orientations inside the sample.

If we focus now on the (200) figures, a stronger orientation appears for the untreated and annealed sample. The expected peak is on the φ = 0° and ω = 0° position and is more focused than for the (111) figures. For the recrystallized samples, nearly the same (200) pole figure appears as for the (111), so also no preferred orientation is visible for this second crystallographic orientation. For the whole (200) system, the expected peak is elongated on the 0° and 180° direction which corresponds to the fiber direction inside the instrument. It can, therefore, be concluded that the (200) plane is only somewhat tilted along the fiber. Overall, the pole figures support the XRD measurements of the fibers and their changes in the preferred orientations for different states of thermal treatment. While the untreated and annealed samples show a slightly preferred orientation in the directions expected for the considered crystal planes, the preferred orientation is lost after recrystallization due to the new constitution of the crystal lattice.

Figure 16 shows the pole figures for the larger 90 µm CuSi3 fibers. Here, a similar result compared to the smaller 30 µm fibers can be observed. While for the untreated and annealed fibers a preferred orientation is visible for (111) and (200), again no orientation is visible for the recrystallized samples.

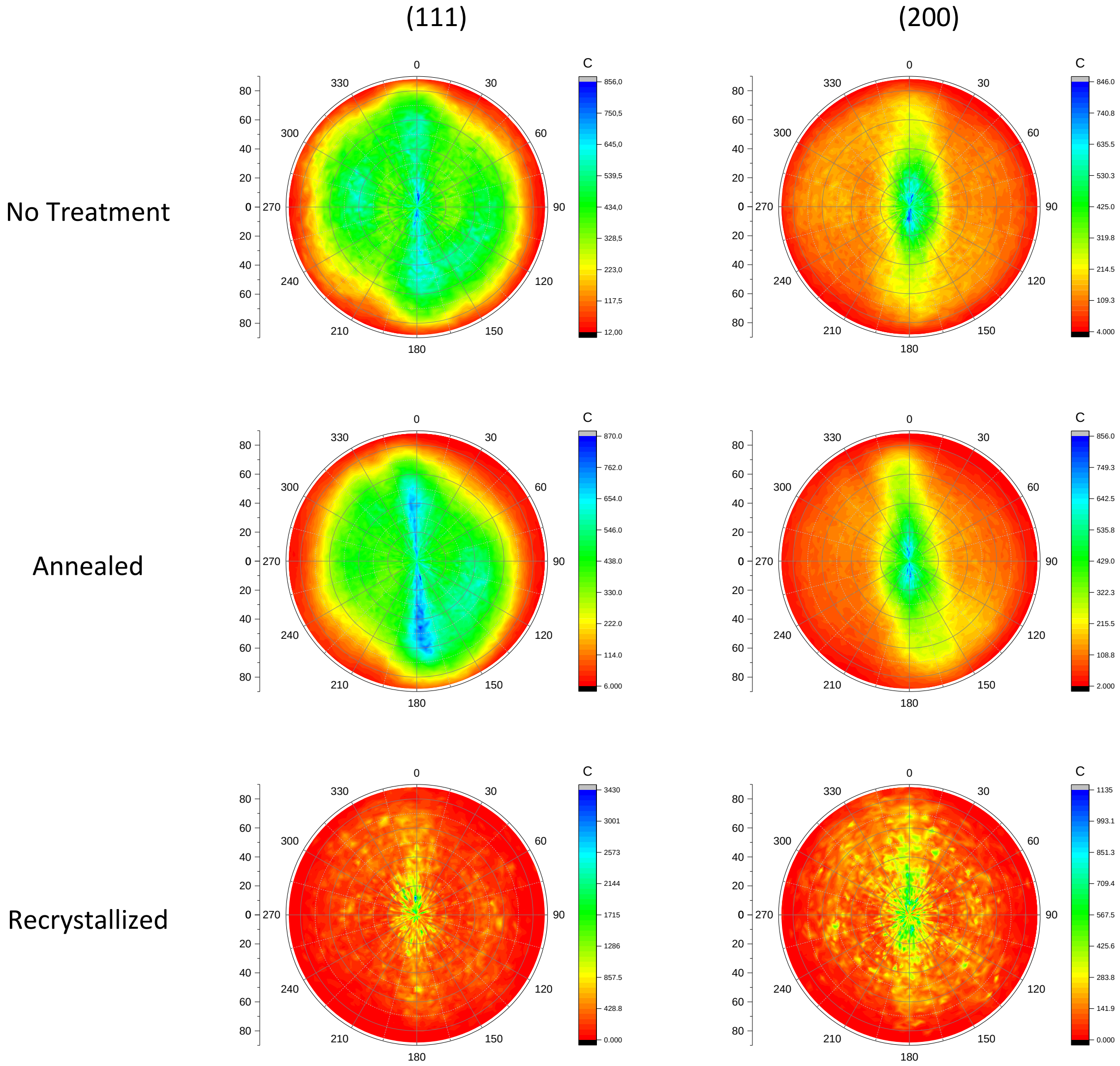

Figure 15: (111) and (200) pole figures for untreated, annealed, and recrystallized 30 µm width CuSi3 fibers.

If we compare the pole figure of the small and larger fibers, the preferred orientation is more dominant for the larger fibers. Taking into consideration the quenching theory and the grain growth, this can easily be explained: If we assume an infinitely fast quenching, the solid state is reached immediately and the atoms have no time to build a crystal structure, therefore, the structure would be completely amorphous. The lower the quenching rate, the more time the atoms have to find their way into their predestined position in the crystal structure. By combining this with the fast acceleration of the wheel, it is obvious that the crystal structure has a preferred orientation due to the production process. As the fibers are pulled out of the molten metal in tangential direction to the wheel, the quenching is faster in this axis. The fibers are mounted for the measurements in a way that this axis is aligned along the φ = 0° to φ = 180° direction. If we assume now that the contact time between the melt droplet and the wheel is equal for all fiber sizes as well as the material-dependent heat transfer rate, the transferred heat per contact area is also equal. Larger fibers have obviously a larger volume than smaller ones, so the energy per contact area is higher. With the same heat transfer rate per area, the higher area energy results in a lower quenching rate for larger fibers, resulting in a higher degree of crystallization and preferred orientations. [110-113]

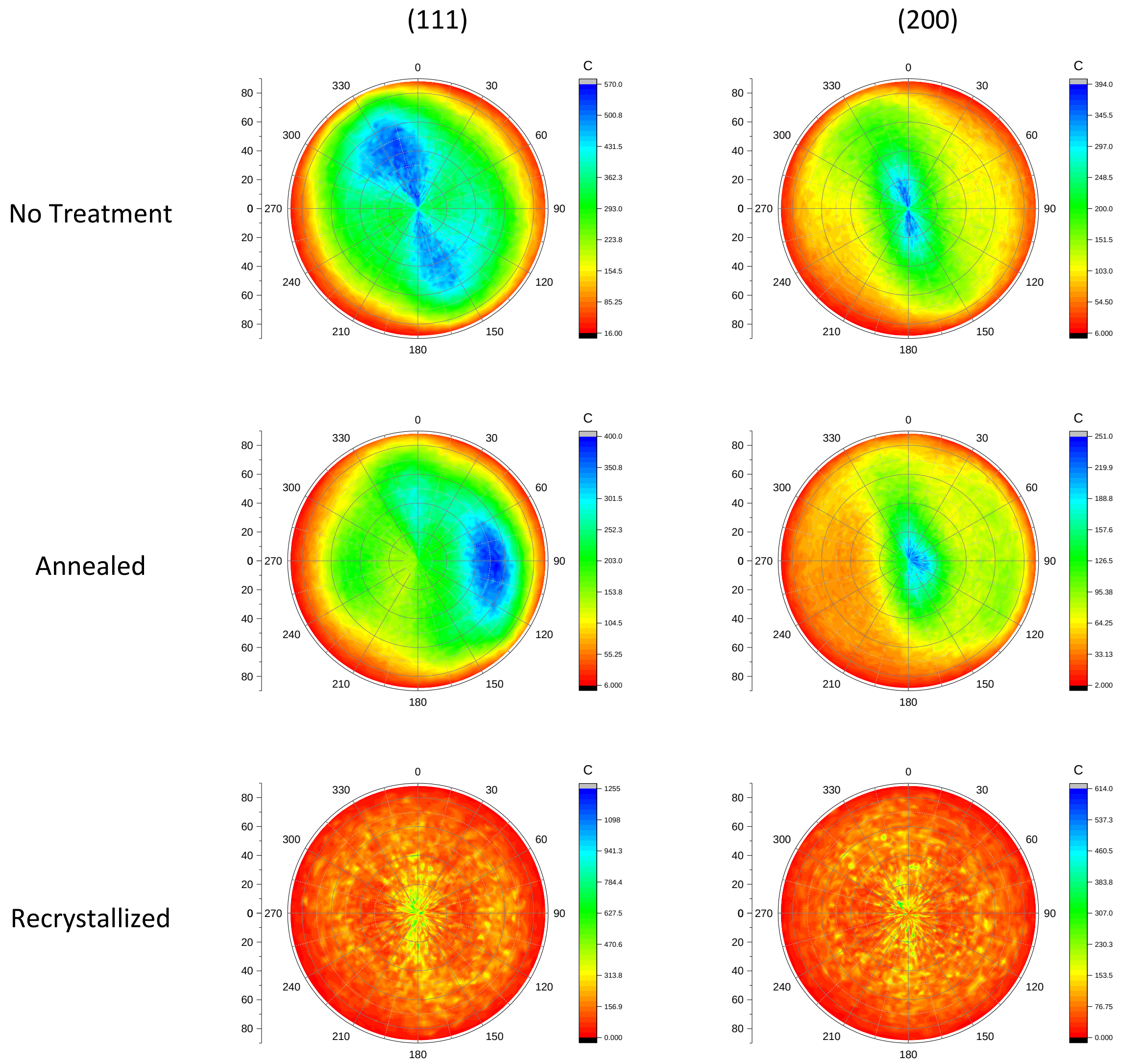

Figure 16: (111) and (200) pole figures for untreated, annealed, and recrystallized 90 µm width CuSi3 fibers.

Another indicator of differences in the quenching rate is the grain size. This parameter is not only different for different fiber sizes, it is also different for the upper and lower side of the fibers. Figure 17 shows SEM images of the upper a) and lower b) side of a CuSi fiber. While the upper side is macroscopically smooth, the lower side, which was in contact with the wheel, is structured. This structuring can be explained by the roughness of the wheel and is just in the range of several nanometers. Consequently, the grains on the lower side are smaller and more elongated than the pseudo round and larger ones from the upper side. Again, the explanation can be found in the thermal diffusivity and the thermal conductivity. For the thermal conductivity, we assume that the heat removal is equal for all areas due to the water-cooled wheel and the area A can be assumed as not dependent on the thermal conductivity calculation according to equation (7). As the same material melt is considered, the only difference lies in the thickness, therefore the thermal conductivity λ and temperature difference ΔT are equal. It can be observed that the thickness ratio is proportional to the heat flow ratio rate of the fibers. The same accounts for the thermal diffusion described in equation (8). For the same material, like in this case, the thermal conductivity λ, the density ρ, and the specific heat capacity c_p are equal. For pure copper, a thermal diffusivity of $\alpha = 114\ \text{mm}^2\ \text{s}^{-1}$ [114] is reported. For a fiber thickness of 10 µm, the heat transport from the upper side to the lower side is in the range of 10^{-7} s. For a heat difference of 1000 K between melt and wheel, the quenching rate on the upper side of the fiber is in the $10^{10}\ \text{K s}^{-1}$ range. Liu *et al.* reported a quenching rate of $8.05\sim3.58*10^{13}\ \text{K s}^{-1}$ to generate copper in the metallic glass state, $3.58\sim0.715*10^{12}$ for the fcc-hcp structure transaction cooling rate and $5.43\sim3.62*10^{11}\ \text{K s}^{-1}$ for the hcp phase [115]. Hence, the quenching rate in the performed experiments was too slow to form a metallic glass and a crystalline fcc copper was formed instead. Figure 17 c) shows the cross section of a torn CuSi fiber. The right side represents the lower side and the left side the upper side of the fiber. This also shows that the grains directly at the contact side with the wheel are much smaller than in the rest of the bulk. This supports the assumptions that the contact area is quenched immediately and the rest cools down slower due to the limited thermal transfer.

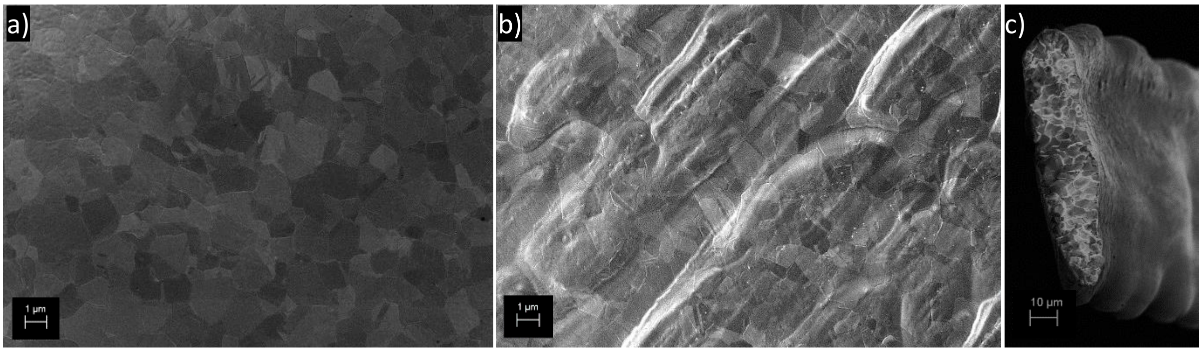

Figure 17: The a) upper and b) lower side of a CuSi fiber and their c) cross section.

To evaluate the difference of the grain sizes for different fiber sizes, several fibers were measured for different thermal states. Fibers with a width of 30 µm, 45 µm, and 90 µm without thermal treatment, annealed fibers and recrystallized fibers were used. The results are shown in Figure 18 a). The smaller the fibers, the smaller the grain size for the untreated fibers. As expected, the grain size does not change during the annealing process. During recrystallization, the grain size is growing for all fiber sizes. The biggest grain growth occurs for the smallest fibers compared to a lower growth for larger fibers. At the beginning of recrystallization an activation energy is needed for the nucleation to set in. While the rapidly quenched atoms are in a non-ideal thermodynamic state, more energy is stored inside the material. Therefore, less external energy supply in form of thermal energy is needed to start the nucleation processes and therefore the recrystallization starts earlier and proceeds faster. The stored energy is discussed in detail in chapter 4.1.2.. The biggest difference in the shape of the untreated (Figure 18 b) and annealed (Figure 18 c) fibers is the smoother surfaces and the more pronounced grain boundaries due to the movement of the crystal defects towards the grain boundaries. [59, 80, 108, 116]

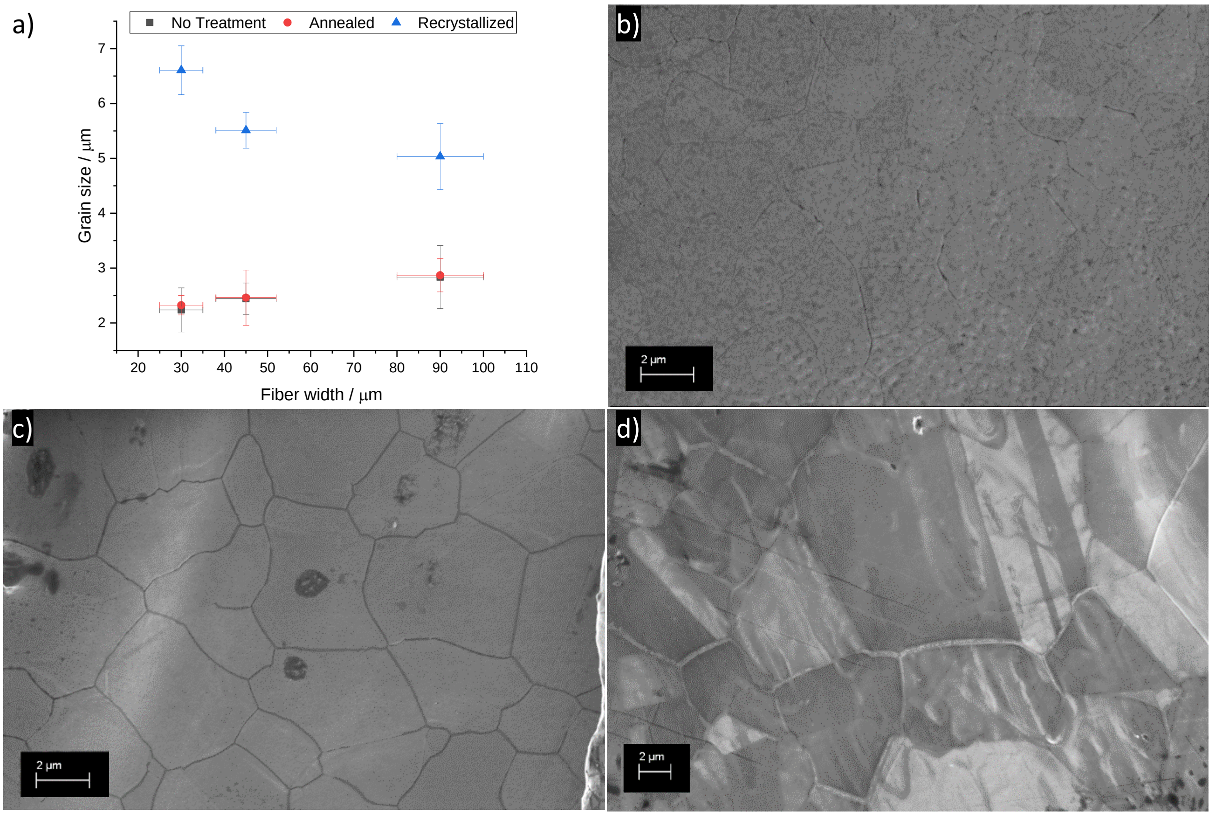

Figure 18: a) Grain sizes of untreated, annealed and recrystallized CuSi3 fibers of different width and SEM images of a b) untreated, c) annealed and d) recrystallized CuSi3 fiber.

However, the situation for the designed alloy Vitrovac appears to be different. Here, the quenching rate is fast enough to achieve an amorphous alloy. The fibers were annealed, crystallized, and investigated with XRD in the same way as the copper fibers were investigated. Figure 19 shows the

XRD pattern of the Vitrovac system. For the untreated and annealed fibers, a typical amorphous pattern is presented showing a typical undefined wave instead of sharp peaks. [68, 117, 118] This is caused by the fact that an amorphous material features only a near order of atoms instead of a far order, which is present in crystalline materials and needed to generate sharp XRD peaks. Thus, for amorphous materials, only blurred and widened peaks can be expressed at those angles where the peaks for the crystalline material would have been expected. [81, 119] Widened peaks are also visible for the crystallized fibers. This can be explained by the undersized grains present in the crystallized fibers with a low degree of far order. [120-122] Therefore it can be concluded that the correct quenching rate is important for the type and structure of the material. Schawe *et al.* presented in their work a theoretical system in which the heating and cooling rate is responsible for the nucleation and the crystal growth of the material. Depending on the cooling rate, a semi-crystalline glass, a self-doped glass or a homogeneous glass is formed. [123] With this, it can be explained the semi-crystalline structure of the fibers discussed in the present work can be explained. Also,by applying much higher cooling rates a less crystalline to completely amorphous material could be obtained.

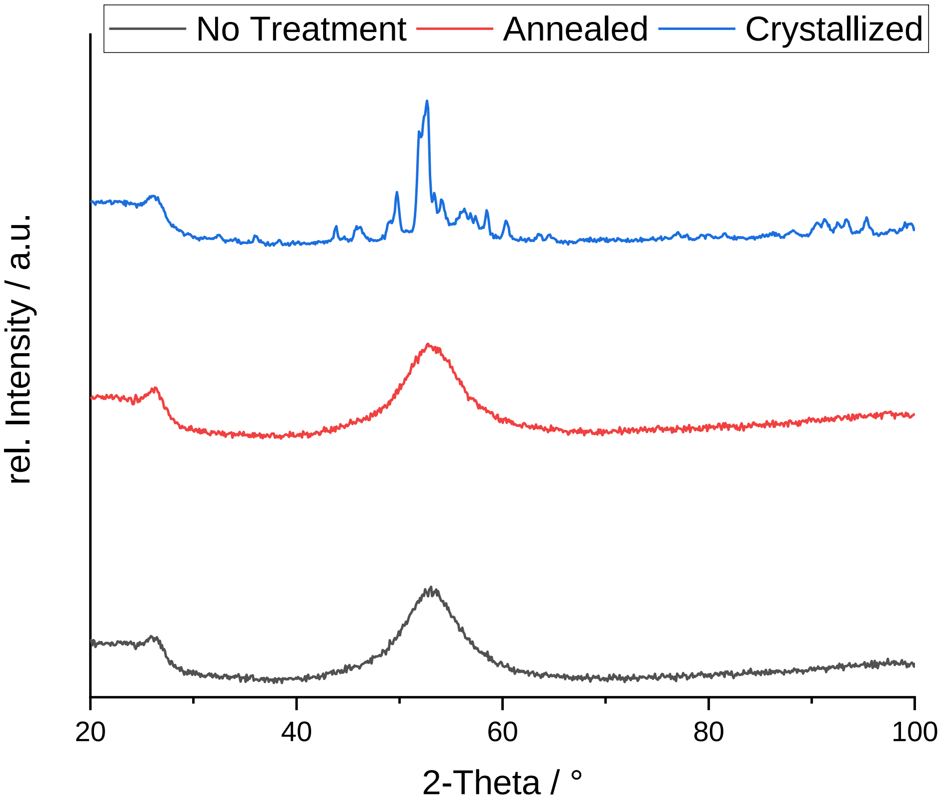

Figure 19: XRD pattern of Vitrovac fibers with and without thermal treatment.

4.1.2. Thermodynamic Properties

Amorphous, nanocrystalline or, in general, all quenched materials are frozen in an unstable or metastable phase. These phases represent atomic positions outside of their thermodynamically ideal positions. Figure 20 a) shows a scheme of different thermodynamic states. The thermodynamic ambition of every material is always to achieve the lowest energetic condition which is normally represented by the ideal crystal structure of the material. Fast quenching and undercooling of the melt, causes the atomic positions to be frozen and a non-ideal thermodynamic system is formed. In the case of Vitrovac, the designed alloy is frozen in an unstable equilibrium. With thermodynamically small treatments like annealing, the atoms move from their frozen and unstable position to metastable positions but the material remains amorphous.

With a more influential thermal treatment, the atoms are moving towards a labile position with the possibility to fall back in the metastable amorphous phase or into the stable crystalline phase. The temperature needed for atoms to overcome the labile state and fall into the crystalline phase is called the crystallization temperature T_c. [75, 80, 124] Figure 20 b) shows the DSC scans of three different Vitrovac samples. During heating, the frozen energy is released as an exothermal signal during heating. [70, 74] The frozen energy is defined here by the energy difference between the frozen energy level and the metastable energy level or the metastable energy level and the stable energy level. The released exothermal energy for the recrystallized sample originates mainly from the surface energy that is released while sintering the fibers. [90] This surface energy is released for all three types of fibers equally, so only the disparity of the curves is discussed here as frozen energy. The small exothermal peaks at 560 °C for the untreated and annealed fibers show the crystallization temperature of Vitrovac. The turning point, where the curve has a positive slope at 1030 °C, is the melting temperature. A detailed Vitrovac measurement can be found in the appendix Figure A 1.

Crystallization of the fibers cannot only occur at temperatures above the crystallization temperature. If a thermal treatment like annealing is applied to overcome the activation energy barrier of crystallization, the material can also crystallize. To achieve this a temperature near the crystallization temperature is needed that is held for a specific time. This mechanism is based on the movement of atoms towards thermodynamically more stable positions during thermal treatment. The closer the treatment temperature is to the crystallization temperature, the lower the energy which is needed to overcome the activation barrier and the faster this process proceeds. [113, 125-129]

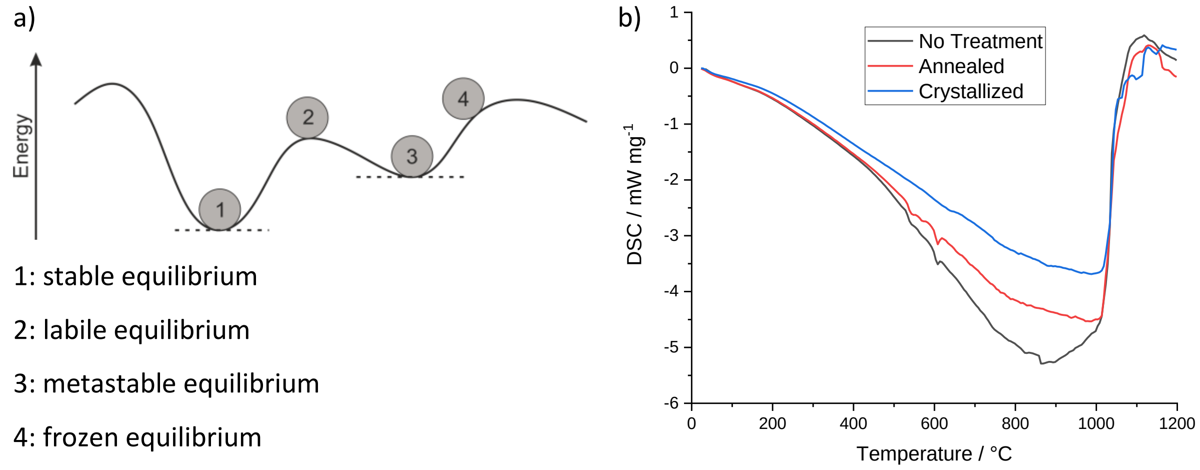

Figure 20: a) Scheme of different equilibria states and b) DSC results of Vitrovac fibers with and without thermal treatment.

If the special properties of the amorphous form are needed, then the manufacturing processes have to be adjusted accordingly, for example during sintering. [130, 131] The crystallization temperature for Vitrovac at a constant heating rate of 10 K s^{-1} was determined to be 565 °C (appendix, Figure A 2). A typical process time for further processing like sintering is 1 h, so the fibers were treated pseudo-isothermally by temperature-modulated DSC to split the reactions in a reversing and non-reversing part. Figure 21 shows the pseudo-isothermal treatment at a) 500 °C and b) 550 °C, the signals were shifted along the y-axis for better visualization. The treatment at 500 °C shows no reaction while an exothermal peak at around 6 min is visible at 550 °C. This peak corresponds to a non-reversible reaction like crystallization. Afterwards, a standard DSC measurement with heating showed the expected absence of a crystallization peak for the 550 °C sample, so the crystallization can clearly be assigned to the event at 6 min. For the 500 °C sample, however, a crystallization peak could be measured proving that no crystallization happened during pseudo-isothermal treatment. To calculate the activation energy of the crystallization Kissinger [132], Boswell [133] and Ozawa [134] formulated equations, all based on the shift of the crystallization depending on different heating rates. The different equations are given as:

Kissinger equation
$$\underbrace{\ln\left(\frac{\alpha}{T_p^2}\right)}_{y} = -\frac{E_a}{RT_p} + \text{constant} \tag{16}$$

Boswell equation
$$\underbrace{\ln(\alpha)}_{y} = -\frac{E_a}{RT_p} + \text{constant} \tag{17}$$

Ozawa equation
$$\underbrace{\ln\left(\frac{\alpha}{T_p}\right)}_{y} = -\frac{E_a}{RT_p} + \text{constant} \tag{18}$$

where α is the heating rate, R the ideal gas constant and T_p the maximum peak temperature. Figure 22 shows the a) shift of the crystallization peak for several heating rates and b) the adapted Arrhenius plot according to the equations (16-18). From the slopes, the activation energy for crystallization was calculated as E_a = 538.7±5.8 kJ mol^{-1}. This is about twice as high as for bulk samples from the same material [118]. The obvious difference is the sample format: here fibers in the micrometer range width are observed whereas Balasubramanian *et al.* investigated around 2mm wide and 40 µm thick samples also produced by Melt spinning. The surface of the fibers is several hundred times larger compared to the foil sample and thus exhibits a higher activation energy to reduce the surface energy. Here, both activation energies of crystallization and surface reduction are overlaying which results in a higher energy border before the unwanted crystallization happens. [90]

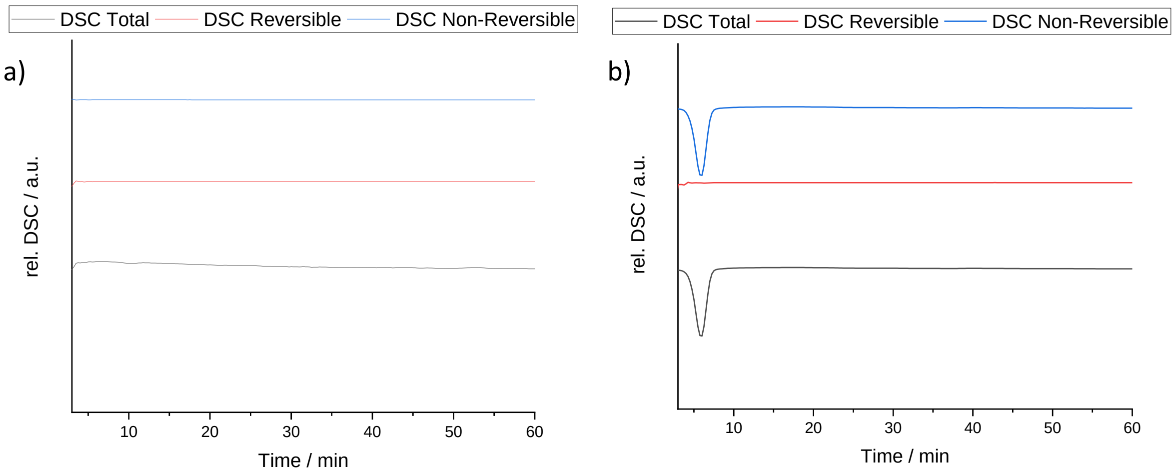

Figure 21: Pseudo-isothermal TM-DSC measurements of Vitrovac fibers at a) 500 °C and b) 550 °C.

The specific heat capacity, c_p, is a good parameter to investigate the energy demand for heating and the stored inner energy. The specific heat capacity is defined as the energy needed to heat up 1 kg of the material for 1 K in order to bring it to a higher energy level. If we compare the energy levels of a frozen and a stable energetic state, it is clear that the frozen state is at an elevated energy level. Therefore, less energy should be needed to increase the energy level even further as compared to the stable state. Thus, the specific heat capacity is lower. [123, 135] Figure 23 shows the heat capacity measurements of amorphous Vitrovac fibers. The peak at around 560 °C is the crystallization, here the specific heat capacity cannot be determined due to the phase transformation. [78]

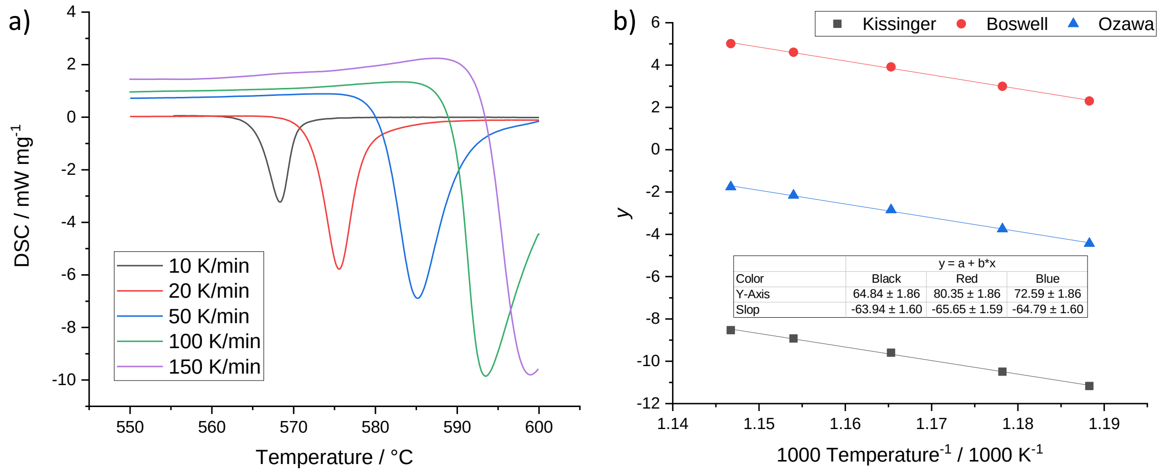

Figure 22: a) DSC measurements with different heat rates and b) activation energy plots.

Specific heat capacity measurements of metallic glasses in literature report a similar trend of the curvature but with significantly higher specific heat capacities. [71, 72, 123, 135] In all of these cases bulk materials were measured. Therefore, the parameter influencing the specific heat capacity seems to be neither the material nor the manufacturing route. However, the surface of the fibers is obviously several hundred times larger than that of a bulk material, especially the surface of the non-round fibers. Wang *et al.* described in their work the influence of the surface on the specific heat capacity [136]. They describe the surface as a negative pressure on the system that softens the phonon frequency and that the specific heat capacity is in direct correlation with the phonon frequency: The smaller the phonon frequency the higher the specific heat capacity. [137] Similar effects are known for material stresses which are also lowering the phonon frequency. [138] The high quenching rate results in a crystallographic orientation of the fibers and the amount of defects and, therefore, internal stress is increased. Thus, the specific heat capacity should be higher for our fibers than for bulk materials. Nevertheless, the measured specific heat capacities are significantly lower than expected, which is due to the decreased heat flow for porous materials like fibers as has been discussed before. If we compare the specific heat capacity before and after crystallization, a drop is visible which can be explained by the crystallization itself. During crystallization atoms jump from their unordered amorphous state to a regular crystalline state with a lower energy. The enthalpy change can be expressed with equation (19):

$$\mathrm{d}H = \mathrm{d}U + p\mathrm{d}V \tag{19}$$

While pressure p and volume V are not changing significantly, $\mathrm{d}V \approx 0$, the enthalpy change ΔH is mainly influenced by the internal energy U, which is decreased during the crystallization, i.e. $\mathrm{d}U < 0$. This is resulting in a negative enthalpy change which leads to a lower specific heat capacity c_p according to equation (6). The negative enthalpy change occurs for every exothermal reaction, i.e. a reaction where energy is released. The specific heat capacity drop is influenced by the cooling rate and therefore by the degree of disorder in the system. [139, 140] Thus, materials without super-fast quenching or after a specific thermal treatment cannot exhibit such a drop.

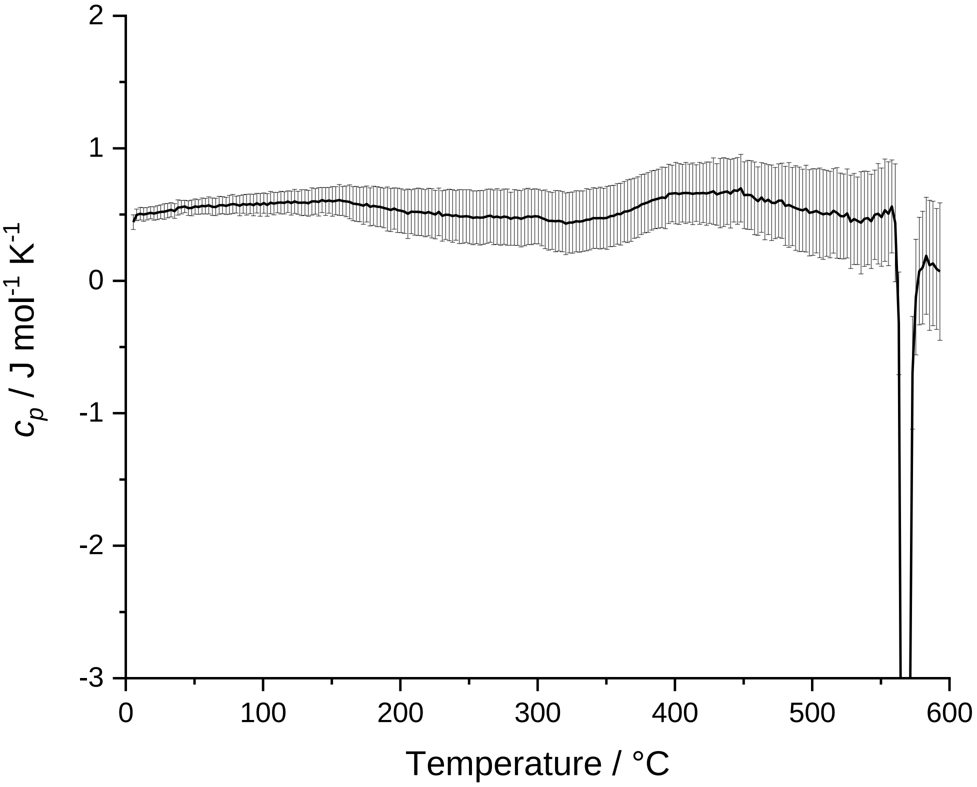

Figure 23: Specific heat capacity of amorphous Vitrovac fibers.

Similar effects can be observed in the also super-fast quenched but crystalline CuSi system. Figure 24 shows the DSC measurements for a) CuSi3 and b) CuSi4. Like the Vitrovac fibers, the CuSi fibers show a strong exothermal reaction. For the CuSi3 fibers, the melting peak is well visible at 1025 °C while for CuSi4 the melting point is only visible as changes in the data slope. The melting point was determined in a second heating cycle as 1002 °C. Both points are in agreement with the copper-silicon phase diagram shown in Figure 8.

While just one solidification peak is visible at 988 °C for CuSi3, two solidification events are visible at 945 °C and 933 °C for CuSi4. This difference can be explained by the phase diagram. While CuSi3 remains in a single phase region where silicon is on interstitial positions in the copper-type structure, CuSi4 enters a two-phase region while cooling. Therefore, first one phase solidifies with a higher amount of silicon from the melt while cooling. Then the residual melt solidifies with a lower amount of silicon. This phase separation is not visible in the first heating step. Due to the super-fast quenching of the Melt spinning process, only one phase is present in the material but in a metastable phase with excess silicon jammed in the copper phase, leading to a stronger distortion of the crystal structure. Consequently, the melting peak is not visible as a single and sharp peak for CuSi4 but only as a slope change. In addition to the melting event, the temperature range also supports other processes like phase separation into two different but more stable phases. These exothermal processes are overlapping with the endothermal melting. In the second heating cycle, the melting peak can be seen clearly as an endothermal event showing a broadening shoulder with slope changes on the side towards lower temperatures. This shoulder can be explained by the two overlapping melting events of the two phases. [78, 79]

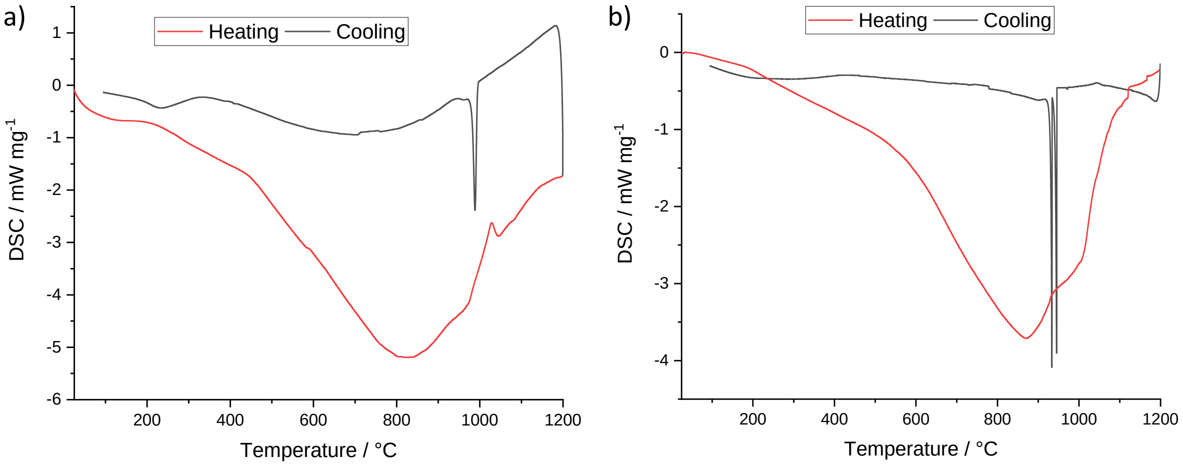

Figure 24: DSC results for a) CuSi3 and b) CuSi4.

For the Vitrovac fibers the difference in energy is directly visible as a drop in the specific heat capacity after crystallization, whereas the CuSi3 fibers are crystalline after production. Therefore, the fibers were annealed to increase the degree of crystallinity and minimize stresses and defects. Qiao *et al.*

reported in their work an increase in the recovery enthalpy for metallic glasses during annealing below the crystallization temperature [71].

Figure 25 a) shows the specific heat capacity for untreated and annealed CuSi3 fibers. The difference between both specific heat capacities is again the enthalpy change due to relaxation according to equation (6). The temperature integral of the data is shown in Figure 25 b). The higher the temperature, the higher the difference in specific heat capacity and the enthalpy change is, therefore, visible. As for the crystallization in Vitrovac, the relaxation is an exothermal event. In order to use the stored energy for a certain thermal process, a high heating rate should be used so that the stored energy is still present and not released during heating. The annealing and, therefore, the release of stored energy is highly time-dependent due to limited growth. [71] Again, it is important to note that the annealing of the fibers was performed at a temperature at which neither grain growth nor recrystallization occurred. Therefore, the initial parameters of the two samples only differ in the values of the internal energy in form of defects, stresses, and metastable phases and not with regard to crystallographic parameters like grain size.

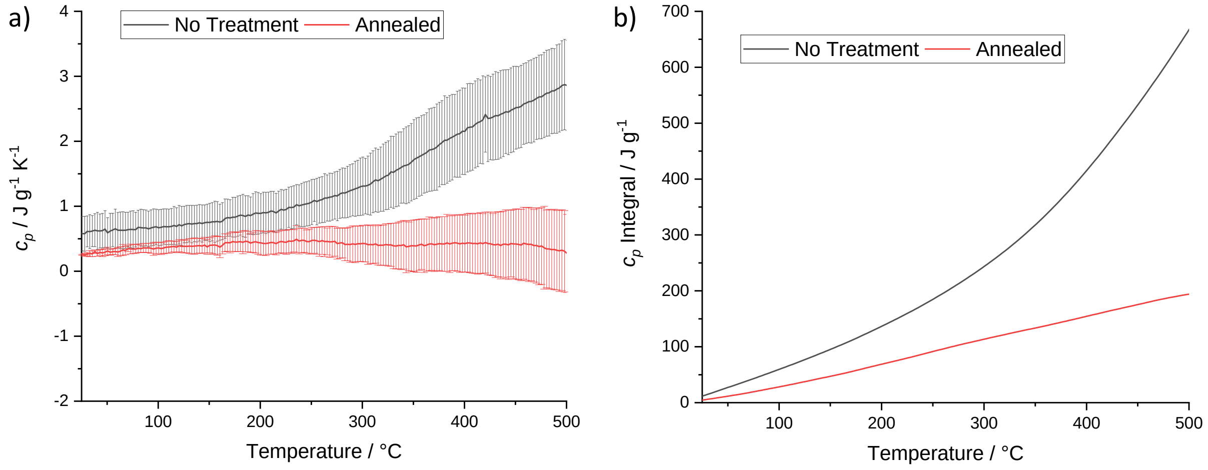

Figure 25: a) Specific heat capacity for CuSi3 fibers in different states and b) the associated time integral.

As the stored energy manifests not only in the change in the specific heat capacity, it can also effect the shift of the exothermal curvature in the heat flow of a DSC measurement as reported by Zhu *et al.* [70]. This was shown for the Vitrovac system in Figure 20 b). The recovery energy for the CuSi system is much lower due to the smaller degree of disorder in the system.

As the thermal contact between sample and crucible is considered the parameter with the most influence on heat capacity measurements, fibrous and, therefore, very porous structures are not suitable for all types of thermal measurements. This leads to a significant error, larger than the actual effect. The main influencing parameters here are the fiber widths and the fiber shapes, which are also crucial parameters when comparing the amount of stored energy within the fibers at different quenching rates. For each set of measurements, the same type of fibers with the same weight per sample were used so that the thermal heat flow is equally limited for all samples of the set. Under these conditions, the measurements can be compared qualitatively. [78, 141, 142]

The fibers were measured with the same measurement program a second time to investigate the influence of external parameters. Here, the measurement data was similar for all samples, independent of their thermal history. Thus, the influence of external parameters on the data acquired during the first run can be neglected. In general, due to the complexity and the error proneness of the measurement setup, thermal analysis measurements are just valid relatively to each other within one system and should not be compared with a different setup without adequate caution. In the case of the CuSi system, the measurement error is rather significant so that the actual effect of the thermodynamic properties of CuSi is overlapped by the error.

In summary, the previously discussed properties for varying grain sizes, crystallographic orders. and stored energy reveal a dependence on the fiber sizes. As smaller fibers show faster quenching rates, the structure is frozen in an undesirable, energetically high state leading to an unstable crystallographic state. This explains the comparatively rapid grain growth of smaller fibers as shown in Figure 18 a) as well as the mechanical properties and later the manufacturing principles like sintering.

4.1.3. Mechanical Properties

The mechanical properties of a material are of major significance as they define not only the stability but also the processability and possible applications. As crystallographic properties like the grain size as well as intrinsic stresses can influence the material properties in various ways, rapidly quenched materials show interesting mechanical properties. Therefore, CuSi3 and CuSi4 fibers were tested via Nanoindentation in different thermal and crystallographic states. Figure 26 shows the results for CuSi3 fibers of different widths and in different states. The first result shows a reduced modulus for decreasing fiber widths. The highest elasticity was measured for all fiber widths for the fibers without treatment. As discussed before, the smallest fibers have the smallest grain size and the highest crystallographic disorder. Additionally, smaller fibers show a higher amount of stored energy that is often accompanied by stresses and defects inside the material.

As already discussed, thermal treatments like annealing or recrystallization can change the mechanical properties due to the reconstruction of the changing crystal structure. For metallic glasses, the degree of crystallinity is increased which results in a so-called embrittlement. This behavior was reported by Zhu *et al.* for a specific metallic glass after different thermal treatments [70]. Liu *et al.* reported a difference in crystallinity caused by different quenching rates [143]. These observations fit with the crystallographic properties and the XRD measurements of the structures discussed in the chapters before. [72, 144-147] Additionally, these results are supported by the thermodynamic observations of the recovery enthalpy while annealing metallic glasses or fast-quenched materials. [71, 72]

If we compare the results with the bulk material properties of a slowly cooled CuSi3 sample, we see that the largest fibers are in the range of a bulk material while the smallest fibers are more elastic. Similar elastic properties as for bulk CuSi3 are known for bulk copper. [148] This corresponds to the principles of Hall-Petch [62, 63] and the reported data from Shen *et al.* [60], also displayed in Figure 5. As discussed, for the annealing process only the internal stress is reduced leading to a decrease of the stored internal energy without a change of the grain size. Hence, the difference between untreated and annealed fibers is defined by the low degree of crystallographic order while the grain size remains unchanged.

Another key factor is the stress induced by the surface. In a thermodynamic ideal system, the volume to surface ratio is maximized to decrease the influence of the surface tension of the materials. The smaller the diameter of a body, the higher is the influence of the surface tension on the whole material. In the case of our fibers, the cross-section is not round but rather resembles an elongated ellipsoid. Therefore, the surface area and with this the surface tension is stronger compared to round fibers. [149-151] A rounding of the fibers can occur during recrystallization, if the treatment time is long enough.

Another reason for the higher elasticity in smaller materials is mainly known from nature: while a single cellulose fiber is extremely flexible, cellulose fibrils, consisting of numerous single cellulose fibers stabilizing each other, show a higher stiffness and allow plants to build mechanically stable structures. Inhomogeneous materials like cellulose show various elastic points and less elastic points. When several fibers bundle up they are stabilized by the surrounding fibers. Compared with large fibers or bulk materials, our fibers have less neighboring structures stabilizing the material against deformation. The more elastic areas in cellulose fibers exhibit an amorphous phase while the less elastic areas have a crystalline structure. [152] A similar behavior can also be observed in semi-crystalline polymers. Here, a crystalline part increases the mechanical strength while the amorphous share enables a certain flexibility. [153]

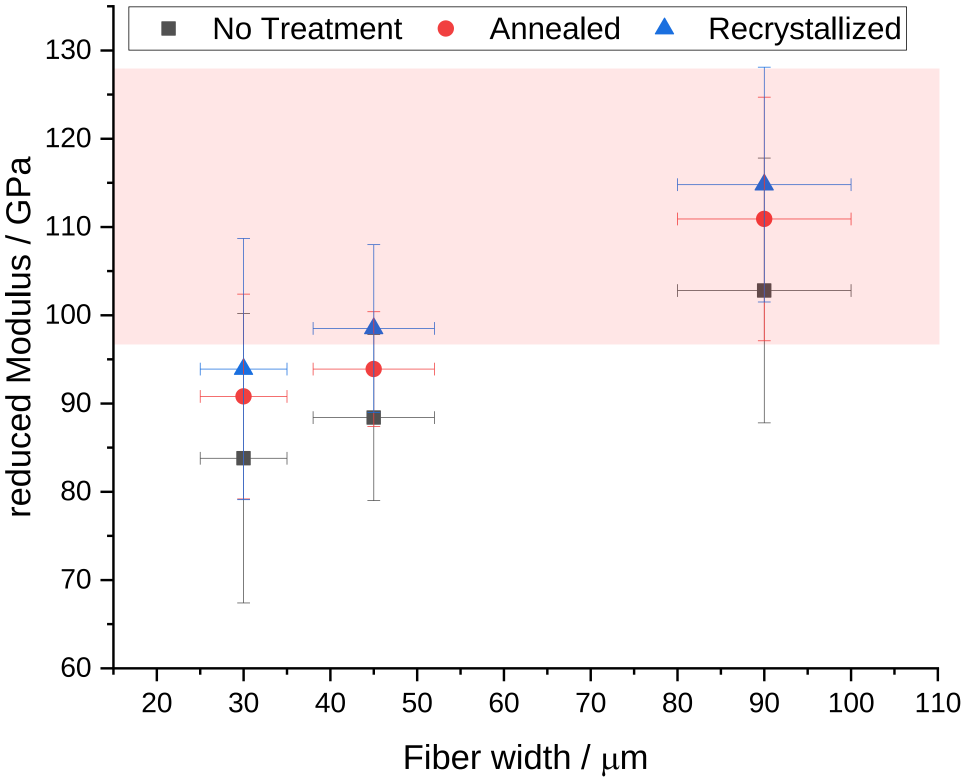

Figure 26: Nanoindentation data for CuSi3 fibers of different widths and states and the CuSi3 bulk properties as red area.

This can be translated to the metal system in our case where the fibers have domains with higher and lower crystallinity, as discussed previously. In the Nanoindentation experiments, the maximal displacement hmax was in the range of around 100 nm with a projected area of 0.34 µm^2. This is smaller than the nominal grain size in the materials (see Figure 18). Hintsala et al. reported in their empirical study that the influenced bulk radius of a Berkovich tip is around 5.6 times higher than the indentations' radii [154]. With a maximal displacement of around 100 nm, the tip radius was found to be around 800 nm. So the affected area is in the range of 4.5 µm, twice as large as the grain size but still smaller than the original fiber diameter. [57] Consequently, a neighboring grain with a lower degree of crystallinity affects the material properties of the whole measured region. As shown above, small diameter fibers, which are quenched with a higher cooling rate, have a lower degree of crystallinity and the influence on the mechanical properties is more prominent than in the case of fibers with a large diameter. This effect is not unique to the microscopic scale: The smaller the fibers, the smaller the number of neighboring grains with higher crystallinity. Hence, the stabilizing effect from neighboring grains with a pronounced crystallinity is weaker than it is in larger fibers.

Consequently, the fibers show a stronger elastic behavior and exhibit haptic properties similar to hair or silk.

Crystallographic orientation represents another influential parameter. Wang *et al.* and Liu *et al.* reported a strong influence of the direction of single crystalline copper on the material properties [155, 156]. In the pole figure experiments performed on our fibers, a strong orientation could be observed. Therefore, orientation could have an effect on the mechanical properties of fibrous materials. An additional effect on the mechanical properties, which is directly linked to the orientation. is the slip mechanism. This process plays a major role in macroscopic deformation and can be described as the sliding of whole crystal planes against each other. [157] The slip plane is always the closest packed plane in the crystal structure. For fcc materials like copper, this is the (111) plane. [158]

In our system with a strong (200) orientation, the (111) plane is in a 54.75° angle to the elongated direction along the fibers length. This leads to a stronger deformation and an increased resistance against cracking in a tensile load along the fiber length.

The results for CuSi4 in Figure 27 show the same trend of the reduced modulus as for CuSi3 fibers. In this magnitude, the determination of different kinds of effects is complex and even with an extremely precise measuring method like Nanoindentation, it is impossible to investigate the different effects independently. Hence, the focus will be on the overall material behavior. Here, the size effect is more dominant for the elastic properties. While for the CuSi3 fibers the untreated sample is always the one with the highest elasticity, the behavior is different for CuSi4. For the smallest two fibers, the recrystallized state is the one with the highest elasticity, for the largest fibers it is again the untreated state. The main difference between the CuSi3 and CuSi4 fibers is the formation of a ceramic and brittle second phase in CuSi4. While the recrystallized sample shows a high concentration of the secondary phase at the grain boundaries, the annealed sample shows a distribution of the phase over the bulk.

The brittle secondary phase precipitations at the grain boundaries are in the double-digit nanometer range. As discussed before, the resolution of Nanoindentation depends primarily on the type and size of the surrounding material. It is therefore not possible to distinguish between the material properties of the two different phases or to determine the material properties of one phase isolated from the other. If the surrounding material is comparably brittle, the influencing area/volume around the indentation is smaller than for soft materials. With the brittle secondary phase, the elastic modulus of the whole material is higher due to the small grain size, especially for the smallest fibers. For the largest fibers, the grains can be sufficiently large after recrystallization, hence the influence of the secondary phase loses relevance. For the annealed fibers, the silicon overloading of the copper phase is not resolved by a secondary phase formation. Here, the material starts to build an area with higher crystallinity in the nanometer range. Furthermore, thermodynamics promote the formation of an unfavorable secondary phase if this phase can severely reduce the stress in the whole material caused by the silicon overloading of the copper structure. As the relief of the thermodynamic state is the main driving force of every self-containing process, the final state of the system will exhibit a lower thermodynamic state as before transformation. [79, 159, 160]

An additional temperature increase after annealing could lead to a diffusion of the secondary phase towards interfaces like grain boundaries or the precipitations could act as nuclei. The impact of such unaffiliated precipitates in the grains is lower than the effect of interconnected secondary phases at grain boundaries. [161-163]

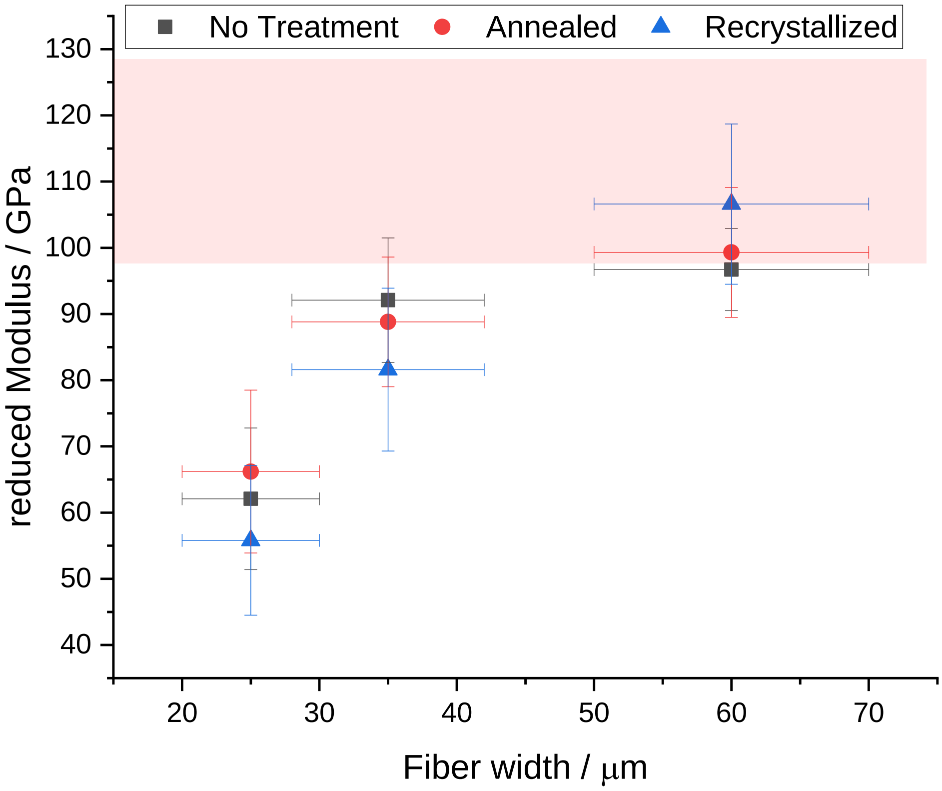

Figure 27: Nanoindentation data for CuSi4 fibers of different widths and states, and the CuSi3 bulk properties as red area.

Yet, another important influence on the material is the stress induced by the quenching. This stress is reduced during annealing by the known/described mechanism and the elasticity of the material is enhanced. In contrast, the degree of crystallization is growing in general for undercooled metals which entails embrittlement. [144, 145, 164] In the case of metallic glasses, changes in material properties are mainly caused by an increasing degree of crystallinity, while in crystalline materials a higher number of related effects are relevant. These effects include influences that diminish or enhance material elasticity like: crystallinity, thermodynamic state, thermal past and material treatments. Due to the variety of overlapping and related influences, it is impossible to differentiate between the respective implications of each effect. Therefore, theoretical considerations from metallic glasses are applied for the design and prediction of experimental outcomes, but empirical and experimental data are more popular for this type of material. [72]

4.2. Networks

For most applications like lithium-ion batteries, mechanically stable and electrically conductive macroscopic 3-dimensional network are required. In this section, the different fleece manufacturing strategies are discussed as well as the respective properties of the connected networks. As these characteristics are based on the fiber properties, sintering strategies maintaining the special fiber properties are discussed as well. Most sintering strategies make use of the energy stored in the frozen meta-stable state and are, therefore, unique for this system.

4.2.1. Fleece laying

Two well-known strategies in fiber technology for the production of networks were investigated for our metal fibers. In particular carding was used for a dry route, whereas a combination of dispersing the fibers followed by vacuum filtration was used for a wet route. While carding is a significant technology for the wool industry, vacuum filtration is widely used in the fleece and filter industry.

4.2.1.1. Carding

Carding is a mechanical process that is based on the detangling and straightening effect achieved by feeding the raw fibers through differently moving surfaces. These surfaces are covered with the so-called card clothing that acts as tweezers pulling the clumped fibers apart, straightening them and laying them into an ordered network.

In the beginning, the unordered fibers were collected by the first drum with the needle-like card clothing, which pulls up the fibers. A second larger drum with a higher rotational speed pulls the fibers out of the first smaller drum. Here, three production specific parameters can be changed and were investigated, i) minimal and maximal fiber length, ii) distance between the drums and iii) the rotational speed.

The minimal and maximal fiber length is mainly determined by geometrical conditions. The minimal fiber length is limited by the card clothing, which is collecting and holding the fibers. In our case, eleven needles per square centimeter are attached on the drum surface, which is relatively fine. The higher the amount of fibers per area, the shorter the fibers can be used while the stress on the fibers is increased at the same time. As the main application for carding is the sorting and ordering of organic fibers like wool, cotton or silk, a cross-section of around 20-30 µm is reported, which is similar to the dimensions of our metal fibers. [165]

The main difference between organic and metallic fibers is their mechanical properties. Metals have a very high elastic modulus compared to organic fibers. For copper, the elastic modulus exceeds the one for cotton by roughly ten times[148, 166] Therefore, organic fibers can be elongated elastically up to 30 % with a lower load compared to metallic fibers.

During carding, the fibers are pulled out of the first small drum by the large drum leading to a parallel alignment. If the needle density on the drum is too high, the fibers get stuck between the needles, especially if knots or agglomerates are present inside the material. In an ideal case, the fibers would be pulled out of the knots and only small residuals stay on the small drum. If the needle density on the drum is too low, the fibers do not stay fixed between the needles and are therefore not transported to the transfer area between the drums and the small fibers fall out of the instrument. Hence, the minimal fiber length could be measured from these fibers as l_{min} = 5 cm. The maximal length of the fibers is limited by the scope of the drums.

The fibers must be shorter than the drum scope, otherwise it is not possible to transfer the fibers from one drum to the other without tearing them apart. Actually the fibers start tearing much earlier limiting the fiber length to l_{max} = 15 cm. While organic fibers are very elastic and can glide smoothly against each other, the metal fibers are comparably brittle. A longer fiber length leads to a higher number of needles the fibers wrap around and increases the induced stress during transfer which increases the risk of the fibers tearing apart. Here, tests with fibers of various lengths were performed and the tearing, knots, and network homogeneity were determined optically. The best results for carding were achieved with fibers with a length of l_{ideal} = 5-7 cm.

The distance between the drums affects the amount of fibers which are transferred and, therefore, can be used to regulate the amount of fibers in the system. In the case of overlapping needles, nearly all fibers are transferred from one drum to the other. Here, the induced stress on the fibers is so high that they are torn apart and cannot be used any further.

If the distance between the needles of the two drums is nearly zero, only the fibers which are not stuck too deep inside the small drum are transferred. Here, the best results were achieved for the CuSi fibers.

On the other hand, some of the knots and agglomerates are also transferred to the large drum and must be sorted out afterwards, leading to the formation of holes in the network. Therefore, the zero gap approach is only valid for fibers without agglomerates.

For fibers more brittle than copper, the stress is still too severe and they are torn apart. For such brittle fibers and fibers with a higher amount of agglomerates, a gap of 2-3 mm between the drums is preferrable. Here, only the fibers that are not stuck in the small drum are transferred with relatively low stress and most of the agglomerates or knots remain in the small drum. Additionally, the drum distance is also a decisive for the final thickness of the fleece.

The rotational speed not only regulates the production speed, for example, the fibers can be pulled out easier from knots or agglomerates at a lower speed. On the other hand, this means a higher risk of an agglomerate being transferred to the large drum. At higher speeds, the tearing occurs more often but the amount of transferred knots and agglomerates is significantly lower. This can be explained by the mechanical properties of the fibers. When pulled slowly, the fibers can glide out of the knot and can be transferred. If the fibers reach their tensile strength before they are pulled out, the fibers are torn apart. The more brittle the fibers, the lower the carding speed has to be set.

As a result of the carding process, the fibers are strongly parallelized and most of the agglomerates and knots are removed. The homogeneity of the resulting fleece is mainly influenced by the amount of used fibers. If just a small amount of fibers is used, pockets with higher area weight can form. The shape of the unordered fibers can explain this. Looking at the fibers directly after Melt spinning, the fiber bunch has domains with a higher fiber density. As carding only parallelizes and flattens the fiber dabbers, the domains with higher densities remain since the fibers are only relocated on a short-range instead of a long-range rearrangement. By re-carding the resulting network, these gradients can be lowered but for every carding step, a certain amount of fibers are torn apart and the amount of scrap grows.

If a fleece with low area weight and, therefore, higher porosity is needed, it can be helpful to use assisting fibers which can be extracted in a further processing step without damaging the metal fibers. For example, the fibers are sintered after carding under protective gas, here argon, at a temperature of around 1000 °C, so a material that completely decomposes under these conditions would be suitable for the assist. To avoid the production of acidic gasses, all chloride-containing materials were excluded. The most promising materials are polymer fibers that solely consist of carbon, hydrogen, and oxygen. Therefore, Polypropylene, Polyester, and virgin wool were tested with the sintering program for their decomposition properties.

Figure 28 shows the STA results for two types of Polypropylene fibers. The lab produced fibers (DWI, Aachen) decomposed completely at around 490 °C, with the decomposition process starting at around 350 °C. Under protective gas, Polypropylene starts to decompose and forms saturated and unsaturated aliphatic hydrocarbons, which are in the gaseous state at these temperatures. [167] The industrial fibers (IFG Asota, Linz) leave a residue of 4.9 wt.-% after processing at 490 °C, while a 2.8 wt.-% residue remained at the maximum temperature of 600 °C.

For the TG-signal, the line for the lab-produced fibers are constant over 490 °C while the line for the industrial fibers is still decreasing slowly. This decomposition over 490 °C is also visible as an exothermal signal in the DSC measurement. After the experiment, black foam stays as residual in the measurement crucible. Studies on the black foam residues of the industrial fibers showed that it contains several elements such as aluminum, sulfur, and phosphorus. All these elements are part of radical starters and catalysts of the polymer synthesis and unproblematic for normal application. However, for our approach only the pure form from lab production can be used. [168] The other types of fibers showed even higher amounts of residues and were, therefore, eliminated from further investigations. The STA measurements are shown in the appendix (Figure A 3, Figure A 4).

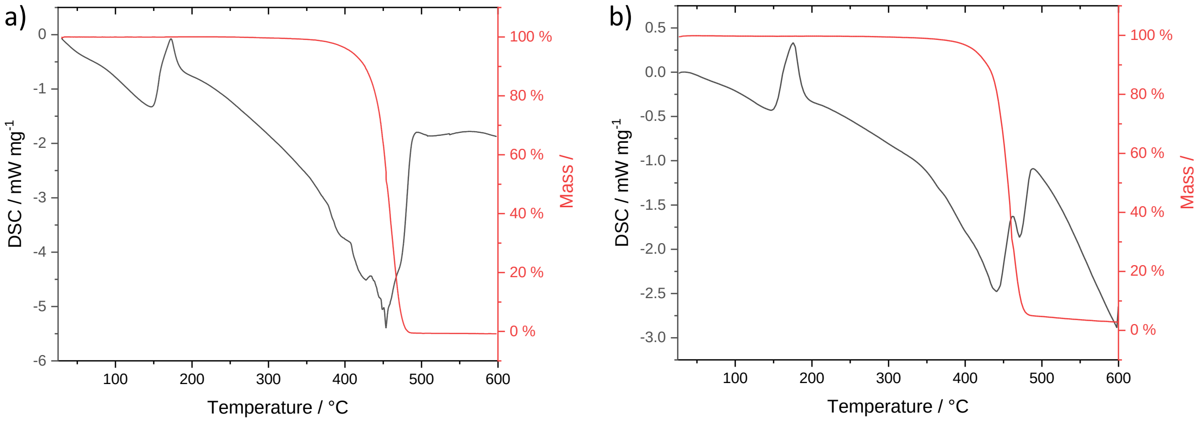

Figure 28: STA measurements of a) lab-produced and b) industrial Polypropylene fibers.

For tests with the assist fibers, some carding experiments were performed with a volumetric metal to polymer fiber ratio of 1:1, 1:2 and 1:3. The higher the amount of polymer fibers, the higher the homogeneity of the resulting metal network before and also after sintering. On the other hand, the higher the amount of polymer fibers, the more often the fiber compound needs to be carded. For a 20 mg cm-2 (metal fraction) metal network, the fiber compound needs to be carded 5-7 times before sufficient homogeneity is reached. It is expedient to mix the polymer and metal fibers as homogenously as possible before the first carding due to the known minor ability to distribute the fibers over a longer distance.

4.2.1.2. Dispersing

As described in section 3.5.1, the parallelized CuSi4 fibers were cut into pieces and subsequently dispersed. Mainly two concepts are known for dispersing. The first concept involves the particles being held in liquid suspense due to the higher viscosities of the used liquid. Typical thickeners are soluble polymers like PVP (Polyvinylpyrrolidone) or PVA (Polyvinylalcohol) or organic substances like cellulose or arabic gum. The second concept is based on the surface modification using surfactants like soap, which is used most often. In this work, however, the focus is on the first concept based on the viscos liquids. This is necessary due to possible problems with contamination of the fibers arising during their later application as current collectors for lithium-ion batteries caused by the surface modifications.

The first investigated system was water as medium and PVP and PVA as thickener. Both polymers show high thickening properties and are well soluble in water. [169, 170] For PVP, thermal decomposition under protective gas is reported to start at 395 °C and reaching 525 °C. Here, a residual of around 3.5 wt.-% remains, so the thermal decomposition under protective gas is not feasible. [171] Insteat decomposition under air was investigated. Figure 29 shows the TG curve of pure PVP (Sigma Aldrich, mol. wt. 40,000) and CuSn8 (engineering product, EN CW453K) with an unknown part of PVP. For the pure PVP, a similar mass loss under air is visible as for a protective gas atmosphere. In the TG curve, a mass residual of 2.5 % is visible while the crucible was completely empty after the experiment. Therefore it can be concluded that a complete decomposition happens and the residual can be ascribed to a balancing error. For the fibers with PVP, a small mass loss starting at 200 °C and up to 380 °C can be correlated with the decomposition of the PVP in the mixture. After 380 °C, a large mass gain is visible which fits perfectly with the oxidation of copper. [172]

These results eliminate the use of polymers as thickeners followed by thermal decomposition for our CuSi fibers due to oxidation. It is impossible to rid the networks of the polymers residual free as the decomposition temperatures under protective gas are too high and the oxidation behavior of the fibers prohibit the use of oxygen-containing atmospheres. For non-oxidizing materials, such as stainless steel, this process is in contrast highly suitable.

In a second approach, a polymer, which is well soluble in water, was used as thickener to test if the remaining polymer after dispersing could be decomposed or washed out. Here, a 1 molar aqueous PVA (Sigma Aldrich, mol. wt. 85,000-124,000, 99+ % hydrolyzed) solution was used to disperse the CuSi4 fibers. The thermal behavior of this setup was investigated using TGA measurements. Here, in a first step, PVA was decomposed under argon atmosphere as a baseline scan. Again, a non-complete decomposition occurs with a residual of 5.3 %, starting at around 250 °C. The results for the pure PVA is shown in Figure 30 as well as the TG measurement for the sample washed for 3 min under running water (5 l min^{-1}). For washing, the network was pressed between two plates of fritted glass (size 00) to achieve a homogeneous water flow over the sample and to avoid destroying the loose fiber network due to the water flow. The decomposition of PVA is described in detail by Peng *et al.* [173]. No mass loss is visible for the washed fibers and the fibers were apparently in the same condition as before and not covered with residual PVA. This shows that the washing approach is helpful for the removal of polymer but that the network homogeneity is lowered by the water flushing, even if the network was pressed between two stabilizing frameworks. The small mass gain for the washed fibers at the beginning can be explained by the buoyancy effect.

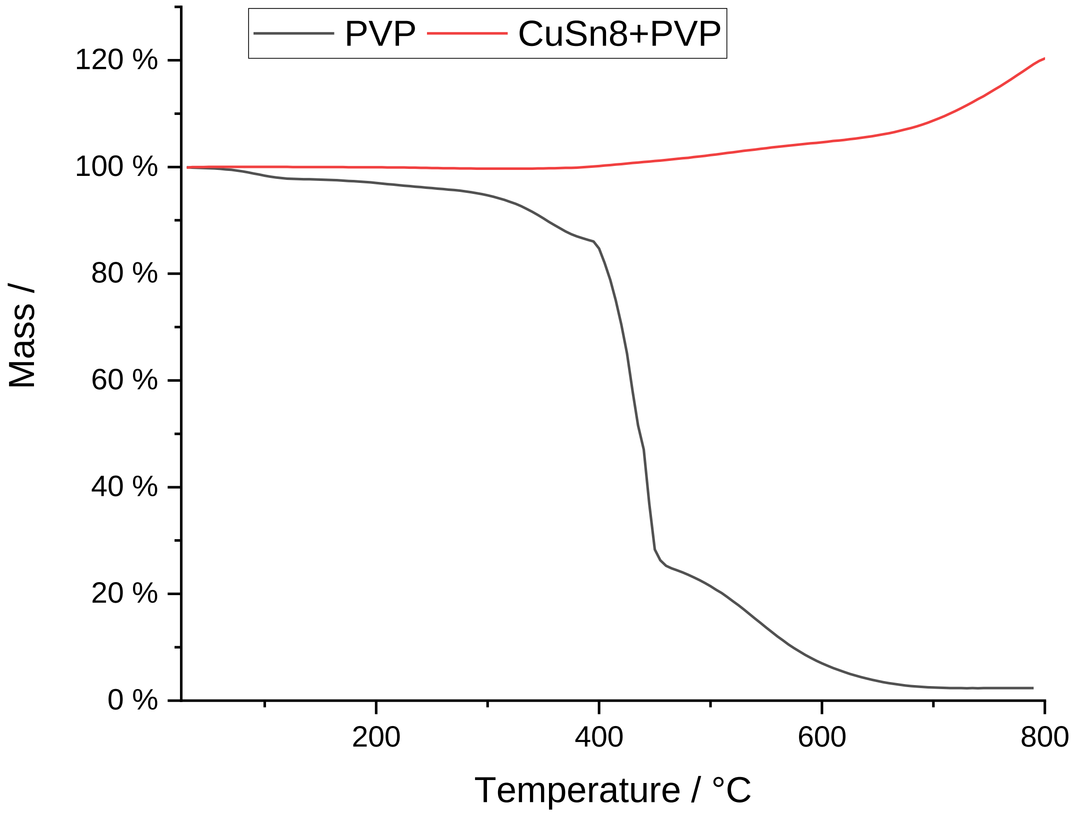

Figure 29: TGA measurement for PVP and CuSn8 fibers with PVP.

For the next approach to find the right dispersing media, a low viscosity paraffin oil was chosen. Paraffin oil consists of different alkanes and, therefore, only of carbon and hydrogen. The chain length is between n = 18-32 with the sum formula C_nH_{2n+2}. Paraffin oil is well known for dispersing metal nanoparticles due to their good wetting behavior. [174] For our approach, a bunch of loose CuSi4 metal fibers were mixed with a drop of paraffin oil (44 wt.-% CuSi4, 56 wt.-% paraffin oil) and tested for their thermal behavior. Figure 31 shows the TGA results for the experiment. It can be seen that starting at around 150 °C, the paraffin oil starts to evaporate and is completely removed at around 320 °C, which is well below the later sintering temperature. In contrast to the above tested polymers, no decomposition occurs here and therefore no residues remain in the fiber network. The above described polymers mainly decompose to low molecular-weight molecules like acetic acid, acetaldehyde, and methine. [171, 173] Most of the low molecular-weight molecules are gaseous at room temperature or slightly above and can be aspirated during the sintering processes. However, the paraffin oil evaporates directly at a comparatively high temperature, so the risk for condensation in the apparatus is comparatively high. The reason for this are cold zones in the instruments, especially in the pumping system. Nevertheless, paraffin oil shows the best results for further dispersing experiments from a processing point of view and is also advantageous for network homogeneity after dispersing and as well after sintering as no residuals remain on the network.

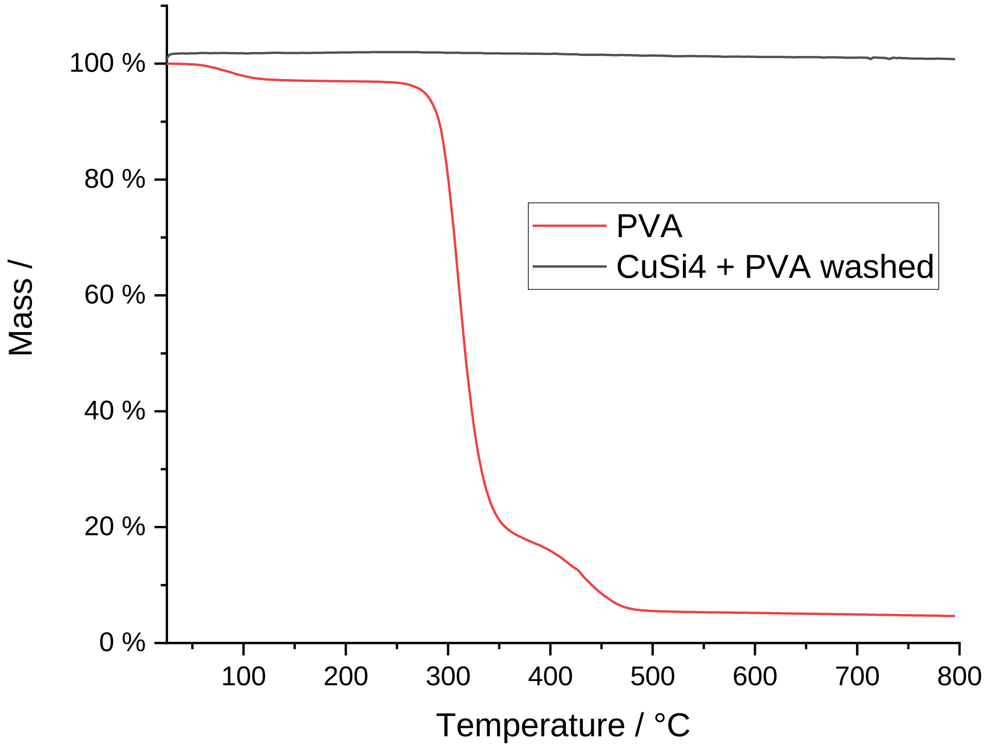

Figure 30: TGA measurement of PVA and washed CuSi4 fibers with PVA.

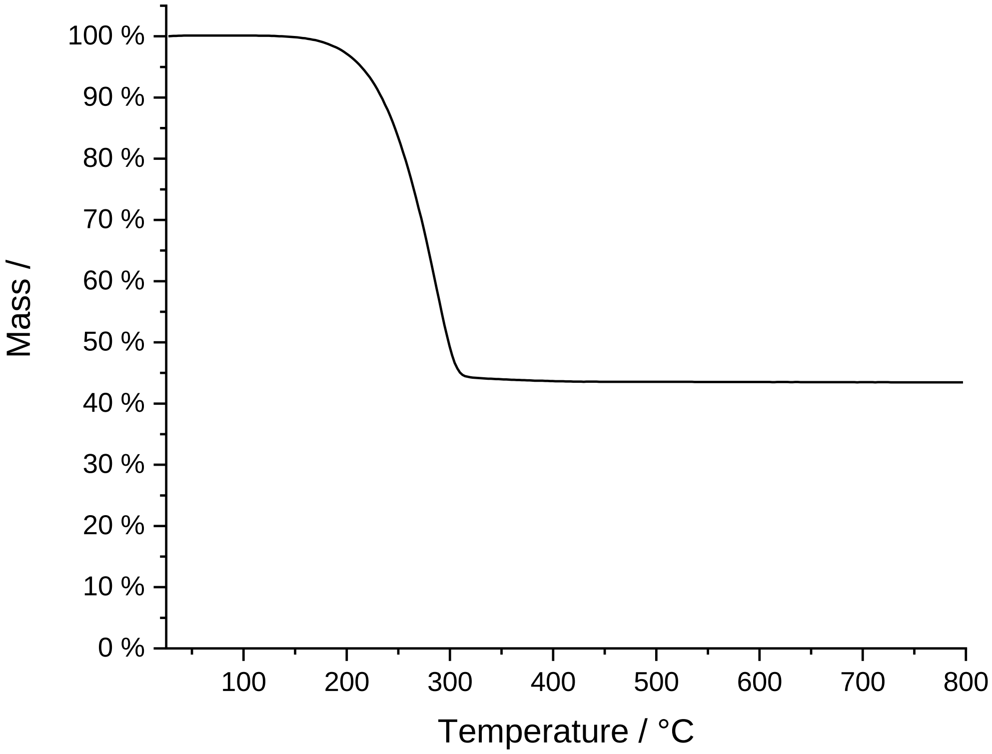

Figure 31: TGA results of a CuSi4 fiber and paraffin oil mixture.

4.2.2. Sintering of metal fibers

Sintering is a basic principle for forming connections between particles without melting the material. The driving force for sintering is the lowering of the Gibbs free energy of the system by minimizing the surface according to equation (14). Therefore, a system with a high surface to volume ratio sinters faster and easier. with regard to our fibers not only their small size is helpful but also their non-round cross-section maximizes the surface compared to round fibers. The surface part ΔG_s of equation (14) can be expressed with (20):

$$\Delta G_s = \gamma_s \cdot \Delta A_s \tag{20}$$

here, γs is the specific surface energy and ΔAs is the change of the surface. [90] If we compare round fibers with non-round fibers, the possible change of the surface is much higher. Depending on the fibers' size and aspect ratio, the surface can be several times higher. Figure 32 shows the sintering junction between two CuSi fibers and the sinter neck on the left side. The former interface of the fibers exhibits a different structure, here depicted as a light grey area and marked with a red circle. This interfacial area is the combined phase of both fibers. Both fibers contain the same material but with different crystallographic orientations. Therefore, the interfacial area can be explained as grain boundaries formed over the former contact point of the fibers. During longer thermal treatments this interfacial area would disappear for thermodynamic reasons. Sintering is a diffusion-based process where the atoms form a new materials structure at the connection points. Therefore, here a different crystal structure is formed. From a thermodynamic viewpoint, it is more preferable to form a stable crystalline phase compared to the meta-stable phase observed in the fibers.

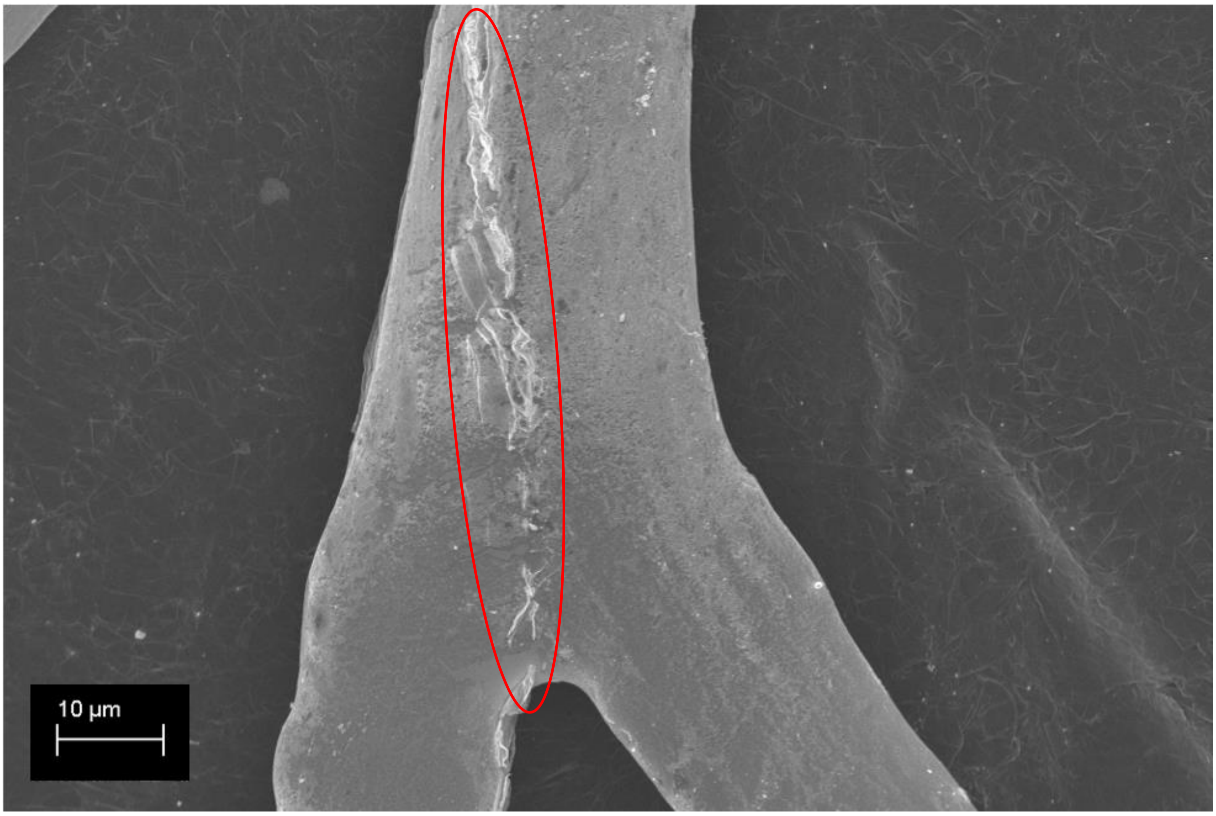

Figure 32: Representative SEM image of sintered CuSi3 fibers with visible necking between the fibers. The red circle marks the interfacial area between the fibers.

With in-situ SEM sintering, the temperature range was determined and also how well the fibers sinter together. Figure 33 shows two excerpts from a video. The temperatures indicated in both pictures were measured with a thermocouple on the heat stage. Noteworthy is the difference of around 100 K with regard to the sintering temperature determined later by ex-situ furnace experiments. This can be explained by the different experimental setups. Whereas an ambient protective gas atmosphere is used during the furnace experiments, a high vacuum is present in the SEM. Therefore, the thermal transport from heating element to the thermocouple is worse in the SEM, so if there is just a tiny gap between thermocouple and heating element then the measured temperature can be much lower than the real temperature present. Figure 33 a) shows the moment two copper fibers starts to sinter, which is visible as a smearing of the interface between the fibers. Figure 33 b) shows the critical temperature of the sintering when the diffusion is so high that a necking of the fibers occurs, preferably at points where the fiber is twisted. The underlying mechanism is again the lowering of the surface energy. In addition, it can be seen that the width of the fibers is decreased, so that not only a necking occurs but the fibers also start to get round and minimize the surface. Therefore, the working range for sintering processes is very small for fibers with these dimensions.

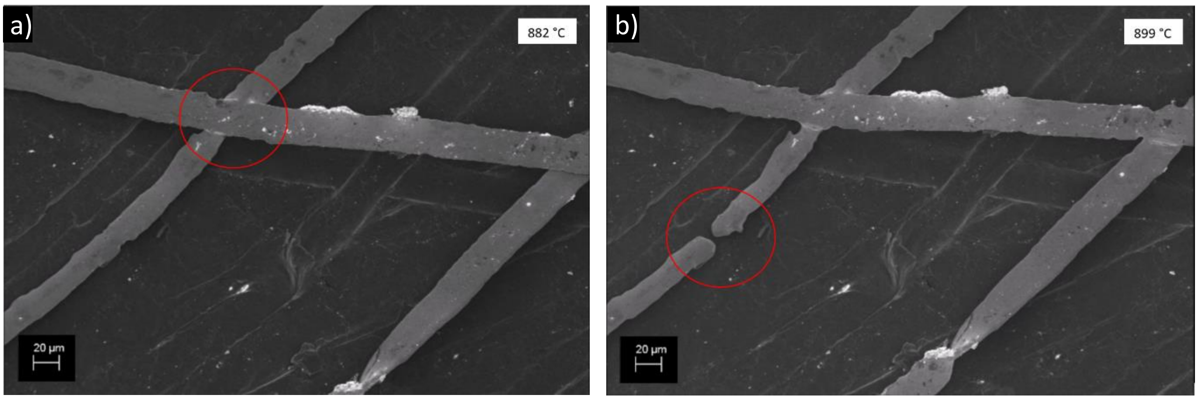

Figure 33: In-situ sintering of CuSi3 fibers with a) the sintering point and b) the necking point of the fibers. The red circles mars these points on the fibers. [175]

4.2.2.1. Sintering with fiber rounding

Parts of the experiments discussed, findings as well as graphs and images in this section are part of the patent application [176].

During a standard sintering process diffusivity is so high and the time so long that everything is moving towards the thermodynamically most preferred state. As the connection between the fibers is formed, the surface in minimized. For round fibers as well as for round particles, the process is described with the well-known 2-particle model. [90] The necking between the fibers is growing more and more until finally the two particles form one oval particle which gets perfectly round with continued treatment. The same principle applies to flat fibers but the contact area between flat fibers is highly increased compared to round fibers. Therefore, the pore volume between two fibers is much smaller and, consequently, the sintering time is reduced.

Additionally, the sintering process can be deliberately used to round flat fibers and create a network of round fibers. This can be used to control the surface area of the network. In many processes the surface area is an important factor for the efficiency of the system, e.g. catalysis, electrolysis or current collectors in battery systems which benefit from large surface areas.

As described in the patent [176], the aspect ratio of the fibers in the network strongly influences the flow rate through a network, for example, in filter or catalysis applications. A higher residence time inside the network can be achieved for low flow rates, so non-round fiber are preferred. Round fibers are better suited if a high flow rate is needed. Therefore, the sintering process as a basic production step was modified to achieve the rounding fibers during sintering and to prevent rounding for different applications.

As we know from Fick's second law (see equation (11)) and the general diffusion equation depicted in equation (12), the process is temperature and time-dependent. Whereas temperature is mostly needed to overcome the activation energy barrier and influences the diffusion speed, time is responsible for the distance the diffusion can overcome. The diffusion coefficient in the sintering temperature range at around 950-980 °C is in the low 10^{-13} m^2 s^{-1} region. [177]

While sintering is finished after a few minutes because of the low distance between the fibers, a much higher amount of material needs to be transported for rounding which leads to longer processing times, especially for larger fibers. Depending on the fiber size, the process can take up to one hour. An experimentally determined sintering temperature for the CuSi4 system is 950 °C with a certain holding time.

If the fibers should be just round but not sintered, a second adjustment of the parameters is necessary. Figure 34 shows untreated and rounded CuSi4 fibers of the same batch as SEM images and Figure 35 depicts the cross-sections. It can be seen that the flat fibers are nearly perfectly round afterwards. As discussed before and according to equation (20), the higher the change in surface energy, the higher the total difference in the free energy. Hence, the flatter the fibers, the higher the surface change and, thus, the faster the process.

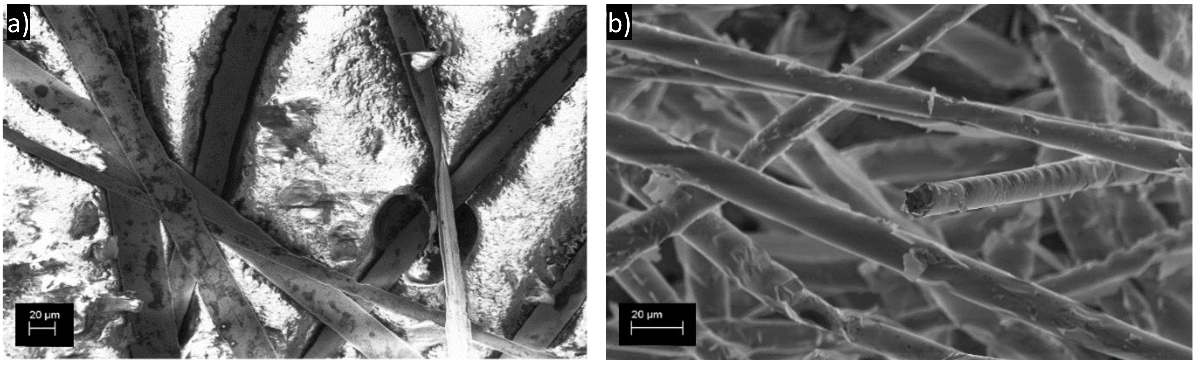

Figure 34: SEM images of a) untreated and b) rounded CuSi4 fibers. [176]

Furthermore, the process proceeds faster at the beginning and decelerates during rounding. There are two reasons for this: firstly, the free energy remaining in the system drops over time, so less can be released during the continuing rounding process. Secondly, the energy stored inside the fibers is released during every thermal treatment, i.e. also during the rounding process. This energy can lower the activation energy and, thus, can also increase the diffusivity.

The cross-section images were used to measure the width and thickness of the untreated fibers as well as the diameter of the rounded fibers and the area of both fibers. The results are shown in the appendix (Figure A 5, Figure A 6, Figure A 7). In addition, the aspect ratio change towards round fibers happens without any change of the cross-section area. While this, the crystal structure recrystallizes. Compared with the process combining sintering and rounding as discussed before, here a lower temperature is needed to avoid sintering between the fibers. Additionally, it is advantageous if the fibers are not in contact with each other or, if this cannot be prevented, that no pressure is applied to the overlaying point of fibers. While for the sintering, a temperature of 950 °C is needed, for the rounding only temperatures above 800 °C are necessary. According to equations (11) and (12), for lower temperatures a longer time is needed for the rounding to pervade the fibers completely. For the general rounding process, no significant difference between a protective gas atmosphere and vacuum conditions were found as the material transport only takes place within the fibers.

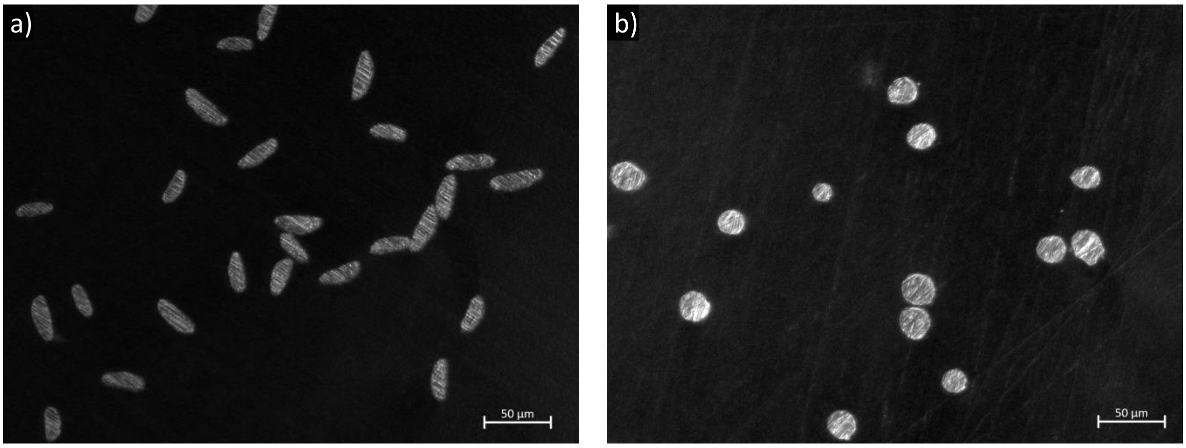

Figure 35: Optical microscope image of embedded cross-sections of a) untreated and b) rounded CuSi4 fibers. [176]

4.2.2.2. Sintering without fundamental change of the aspect ratio

Parts of the experiments discussed, findings as well as graphs and images are part of the patent application [175].

A high surface area is helpful for some processes, so flat fibers are advantageous compared to rounded fibers. Thus, a sintering process that prevents the rounding of fibers was developed. The key parameter here is the heating rate. As we know from the DSC investigations, most of the stored energy is already released after a slow heating with 10 K min^{-1} as soon as the sinter temperature is reached. Therefore, the temperature must be increased as fast as possible to use the stored energy at the fiber interfaces to obtain sintered fibers without the time-consuming rounding process. Experiments with a heating rate of around 900 K/min showed that the fibers are sintered together but without a fundamental change of the aspect ratio. Figure 36 shows two sintered fiber intersections with fibers still in the non-round shape as before sintering. As for the fibers with a change of the aspect ratio, a sinter neck can be observed between the fibers. Therefore, the sintering here is running according to the same principles as described above.

To show the influence of the stored energy, annealed fibers were sintered with the same parameters as the untreated fibers. The untreated fibers were sintered as flat fibers starting at 910 °C whereas the annealed fibers needed a temperature of 970 °C to show first signs of sintering. Additionally, the sintered annealed fibers featured already a more round character as before the sintering process. Furthermore, the untreated fibers were sintered at 970 °C but also showed a rounder shape as before. In conclusion, only untreated fibers can be sintered without fundamental change of the aspect ratio since the stored energy is essential for this.

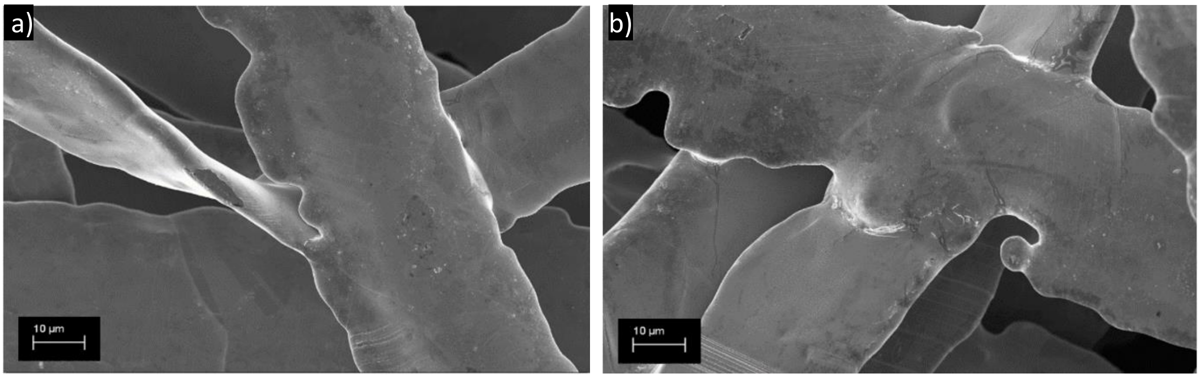

Figure 36: Sintered CuSi3 fibers without fundamental change of the aspect ratio. [175]

This need for stored energy or, more generally speaking, the beneficial character can be explained by the equation for the Gibbs free energy G and equation (21):

$$\Delta G = \Delta H - T\Delta S \tag{21}$$

ΔG (14) is negative during sintering due to the change of the surface (equation (20)) and can be assumed as equal for the glassy ΔG_a and annealed ΔG_a state. Therefore equation (21) can be reformulated to:

$$\Delta H_g - T_g \Delta S_g = \Delta H_a - T_a \Delta S_a \tag{22}$$

Ensuing from the release of the stored energy and equation (6), ΔH_g is significantly smaller than ΔH_a and, therefore, equation (22) can be reformulated to:

$$T_g \Delta S_g \ll T_a \Delta S_a \tag{23}$$

Therefore, the process temperature *T* required to fulfill the sintering is lower for fibers with stored energy than for fibers without. The reason for this is that the beneficial release of the stored energy leads to a lowering of ΔG. During sintering with a normal or slower heating rate, the energy is released during heating and, therefore, no beneficial effects are expressed.

Another aspect is the heating rate-dependent shift of temperature-dependent processes. [72] The stored energy in the interface between the two fibers is released within a short timeframe at such high temperatures, so that the interface area starts sintering at a lower system temperature while the rounding and necking of the fibers is shifted to higher temperatures because of the high heating rate. A detailed look at the fibers in Figure 36 b) supports these assumptions. In comparison to other sintered fibers not only a sintering neck interconnecting the two fibers is present here but the fibers also look like they were literally fused together leaving no space between the two fibers. Hence, the contact area is extremely large and, thus, the connecting forces are very strong.

4.2.2.3. Pressure-assisted low temperature sintering

Parts of the discussed experiments discussed, findings as well as graphs and images are part of the patent [178].

As discussed in the previous sections, the mechanical properties can change upon different thermal treatments. For normal sintering processes, the temperature is high enough so that, for example, Vitrovac would crystallize during sintering or CuSi4 would split into the two phases. To prevent this from happening, a sintering process at low temperatures is needed. From equation (23) we know that due to the stored energy lower temperatures are necessary for sintering. Experimentally, the temperature difference was found to be in the range of just several Kelvin, so an additional driving force is needed.

In this case, the additional driving force is pressure. The rapidly quenched materials are in a crystallographic non-preferred state with a lower density than in the ideal crystalline state. [179, 180] Slipenyuk *et al.* reported a direct correlation between enthalpy relaxation and free volume reduction and, thus, a density increase during the relaxation process. [181] This is in agreement with phenomenological considerations. If pressure is applied to a material, the material can at some point no longer withstand the stress. On the one hand deformation can lead to stress reduction, on the other hand a densification process can reduce the stress. Some materials exhibit special high-pressure modifications, for example, diamond in the carbon system. [182]

The phase transformation or in general the atomic movement in a phase with a higher degree of crystallinity is a diffusion-driven process. From a thermodynamic viewpoint, it is preferred to form a connection within the pressured material to lower the surface, i.e. in other words sintering occurs. In the case of Vitrovac sintering occurs at temperatures of only 350 °C, if a pressure of 35 MPa is applied to the network. These transformations happen very fast, so a sintering time of 1 min and less is sufficient. For other materials like CuSi fibers similar process parameters were needed. In general, a temperature of just around 30-40 % T_m is necessary with a pressure in the lower MPa range.

The process is detailed exemplarily for Vitrovac fibers. After fleece laying and pressure sintering, the networks were measured with XRD for their crystallographic state. Figure 37 shows the XRD results of the pressure-sintered Vitrovac network and crystallized Vitrovac fibers as reference. It can be seen that the material is still amorphous. It is expected that the interface area between the fibers has a higher degree of crystallinity. However, this cannot be measured with XRD due to the overlaying of the amorphous and crystalline phases. Hence. the fiber cross-sections were investigated with Nanoindentation.

Figure 38 a) shows the scanning probe microscopy (SPM) image of the cross-section of sintered Vitrovac fibers. The white box illustrates the area where a XPM^{TM} modulus mapping was performed. XPM^{TM} is the product name of Bruker Inc. for their ultra-fast modulus mapping, i.e. many single indents at a specific distance in a short time. This allows the modulus distribution over an certain area to be determined. Additionally, the resulting indents are visible in this area. Figure 38 b) shows the results of the XPM modulus mapping. As can be seen there, the interface area in between the fibers has different mechanical properties than the fibers themselves. To exclude the influence of surface roughness, the surface profile of the sample is shown in Figure 38 c). An average surface roughness of just R_a = 6.39 nm was measured over the whole indentation area.

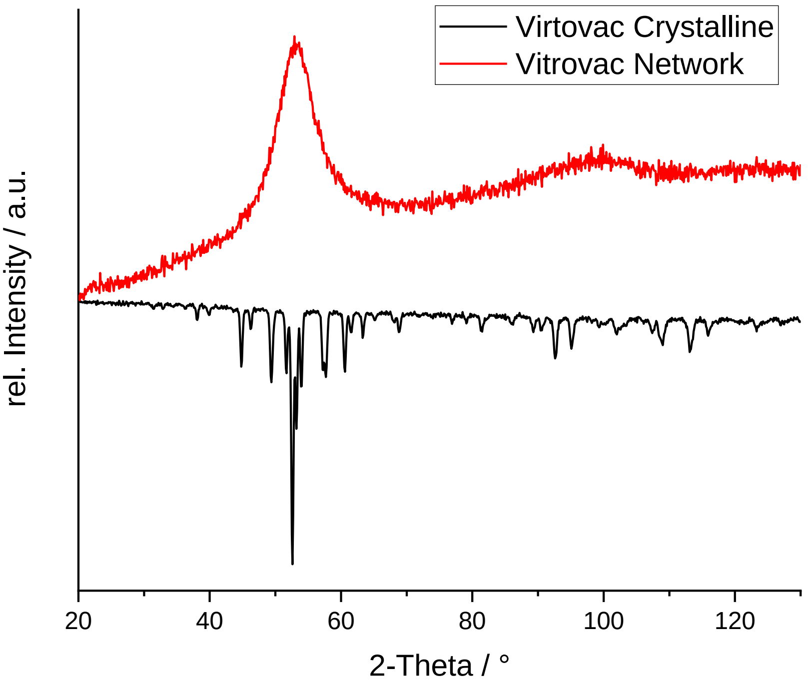

Figure 37: XRD patterns of pressure sintered and crystalline Vitrovac as reference.

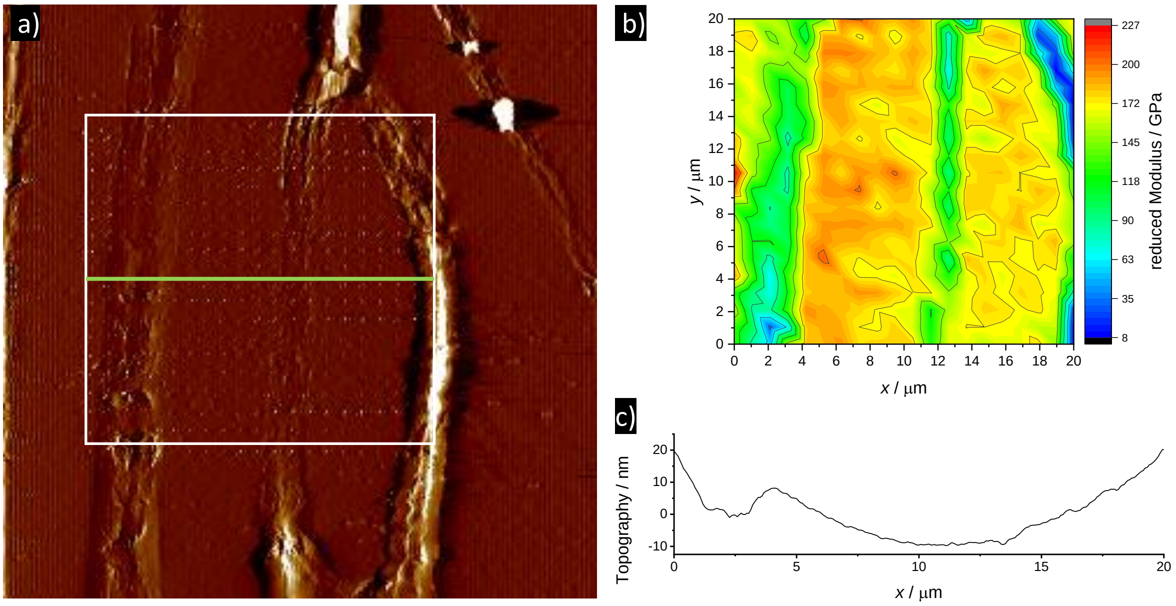

Figure 38: a) SPM image of the sintered fiber cross-section with the indentation area (white box) and the topographic scan (green line), b) the XPM modulus mapping and c) the topographic scan.

These cross-section interface layers between the fibers are also visible in the SEM. Figure 39 shows sintered fibers. In Figure 39 a) the interface layers between the fibers are all in the same thickness range, so that a global and controlled process is expected instead of a spontaneous local process. In between the fibers in Figure 39 b), a typical sinter neck between fibers is visible. Therefore, a diffusion-controlled process under the normal sintering conditions is expected. Temperature, time, and pressure variations were performed to investigate these in more detail.

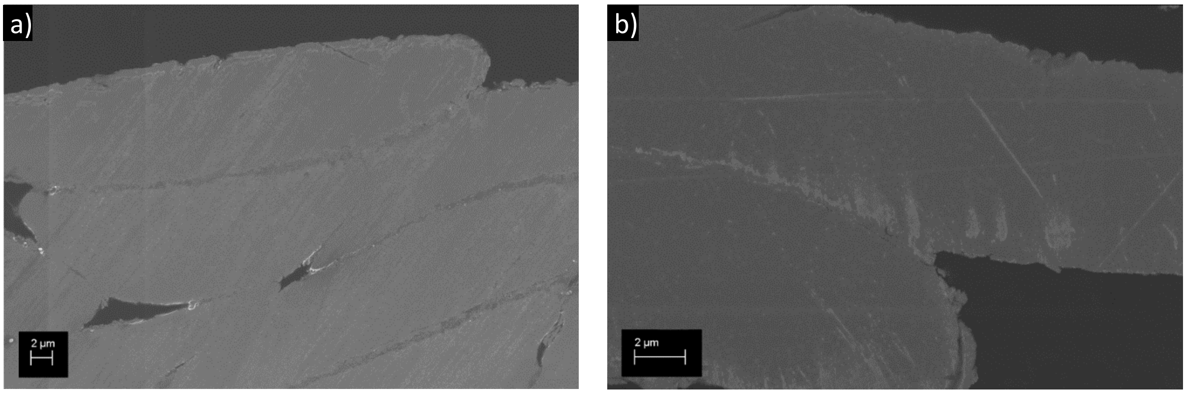

Figure 39: Pressure-assisted low temperature sintered Vitrovac fibers.

Figure 40 shows the results of the pressure-assisted low-temperature sintering according to equation (13) for 450 °C. The data for 350 °C and 400 °C can be found as Figure A 8 and Figure A 9 in the appendix. Here, the displacement is the difference between the former interface and the new interface between fiber and interphase layer, i.e. the half of the total formed interface. A diffusion typical linear behavior of the time displacement relation is visible. Moreover, a higher pressure means a thicker interface layer. From the slop fit, the diffusion coefficient *D* was calculated for all parameter sets. The diffusion coefficients were plotted as an Arrhenius plot and can be found as Figure A 10 in the appendix. From the Arrhenius plot, the self-diffusion coefficient D_0 and the activation energy E_a were calculated according to equation (12). Both are plotted against the pressure in Figure 41. Activation energy and self-diffusion coefficient are independent of the temperature, which has a strong impact on diffusion. For the whole system, an equal self-diffusion coefficient and activation energy is expected. Therefore, the induced pressure is responsible for the difference between the data points. To achieve such a high diffusion as observed here, a higher activation energy is needed. Since for all experimental sets the same temperature was used, the same amount of activation energy was provided to the system by thermal energy. The remaining part of the activation energy must be released energy due to the pressure-induced shift from the structure into a phase with a higher degree of crystallinity. The same is true for the self-diffusion coefficient. The self-diffusion coefficient decreases with increased pressure and, therefore, the occurring diffusion is more a product of the induced energy instead of high self-diffusion. The self-diffusion coefficient is a material constant, so it should be equal for the same material. Thus, pressure influences the activation energy as well as the self-diffusion coefficient. As a control experiment, the same parameters were applied to annealed fibers without any visible sintering effect. Therefore, the stored energy is essential for this special sintering technique.

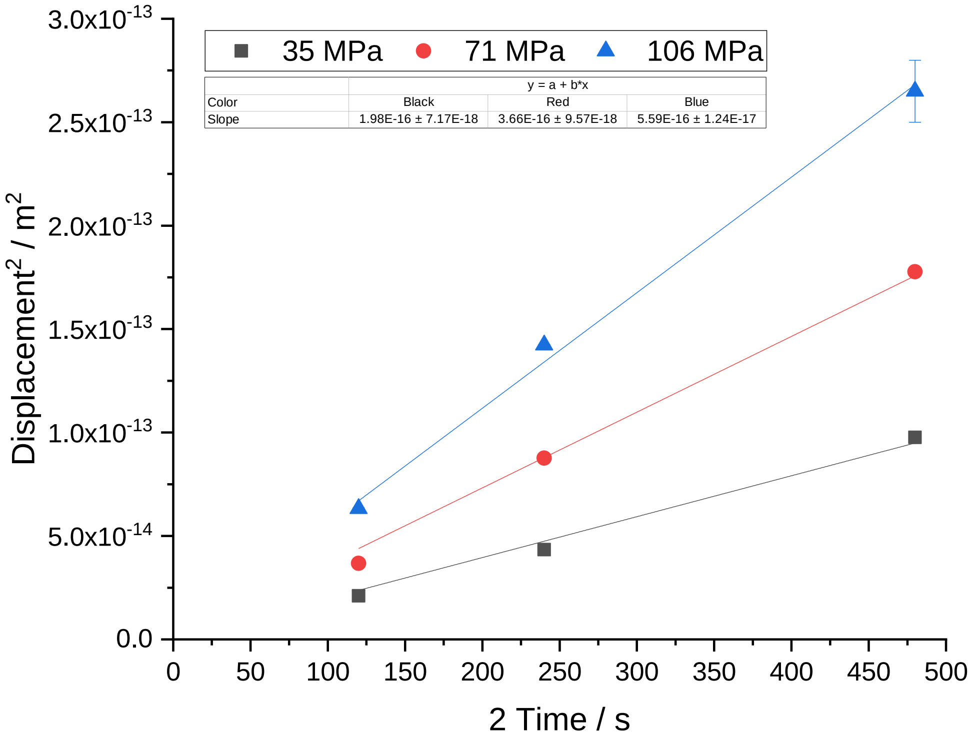

	y = a + b*x		
Color	Black	Red	Blue
Slope	1.98E-16 ± 7.17E-18	3.66E-16 ± 9.57E-18	5.59E-16 ± 1.24E-17

Figure 40: Diffusion interface data for Vitrovac at 450 °C.

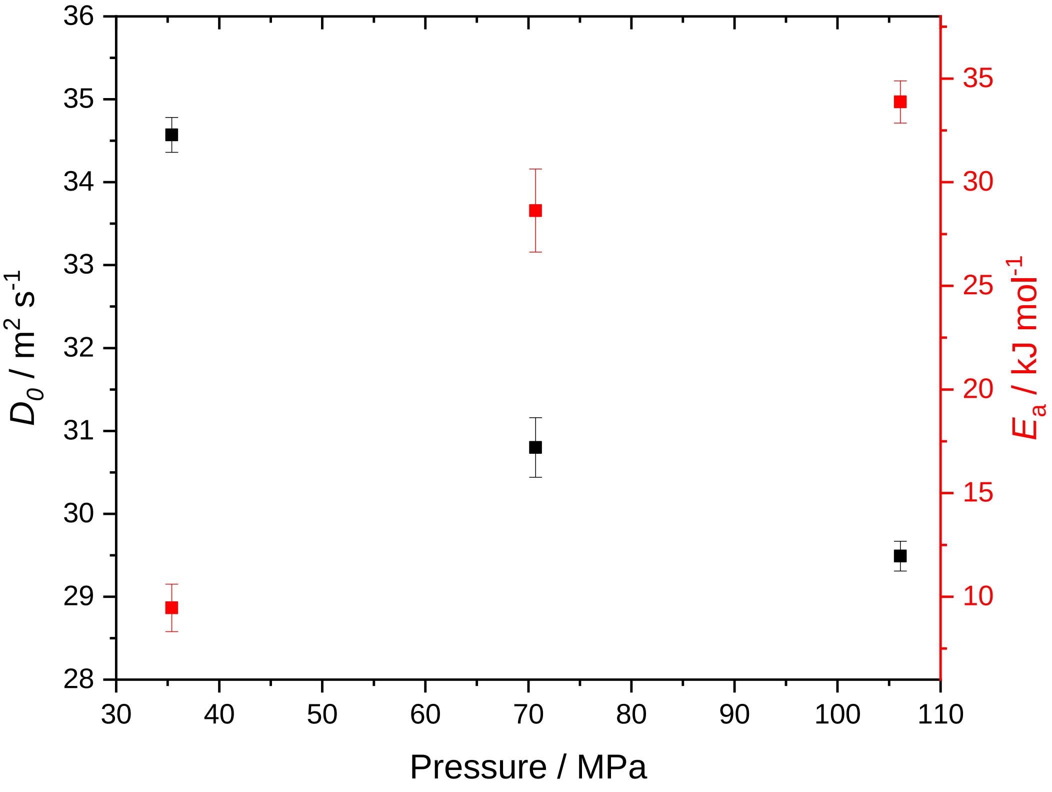

Figure 41: Self-diffusion coefficient D_0 *and activation energy* E_a *from pressure-assisted low-temperature sintered Vitrovac fibers.*

4.2.3. Network Properties

Fiber length and density represent the main influence on the mechanical properties of a network. Therefore, different fiber lengths were tested and compared to each other to investigate the mechanical properties as well as the electric conductivity. All CuSi4 fibers were cut as described before and dispersed in paraffin oil. The first investigated parameter was the homogeneity of the loose network. Figure 42 shows the variation in fiber length and area density. The networks exhibiting the highest homogeneity were produced with short fibers. The longer the fibers, the bigger is the chance that the fibers start to agglomerate and form inhomogeneities inside the network. The same principle applies to higher amounts of fibers per volume of dispersing media. If the density is too high, the fibers start to agglomerate. After the fibers were sintered, the electric conductivity was measured in two directions perpendicular to each other. No influence of the measurement direction was observed for the dispersed networks due to a statistical distribution of the fibers in every direction. The results are shown in Table 5. The higher the area density and the longer the fibers, the higher is the electric conductivity. This happens due to less connection points between the fibers.

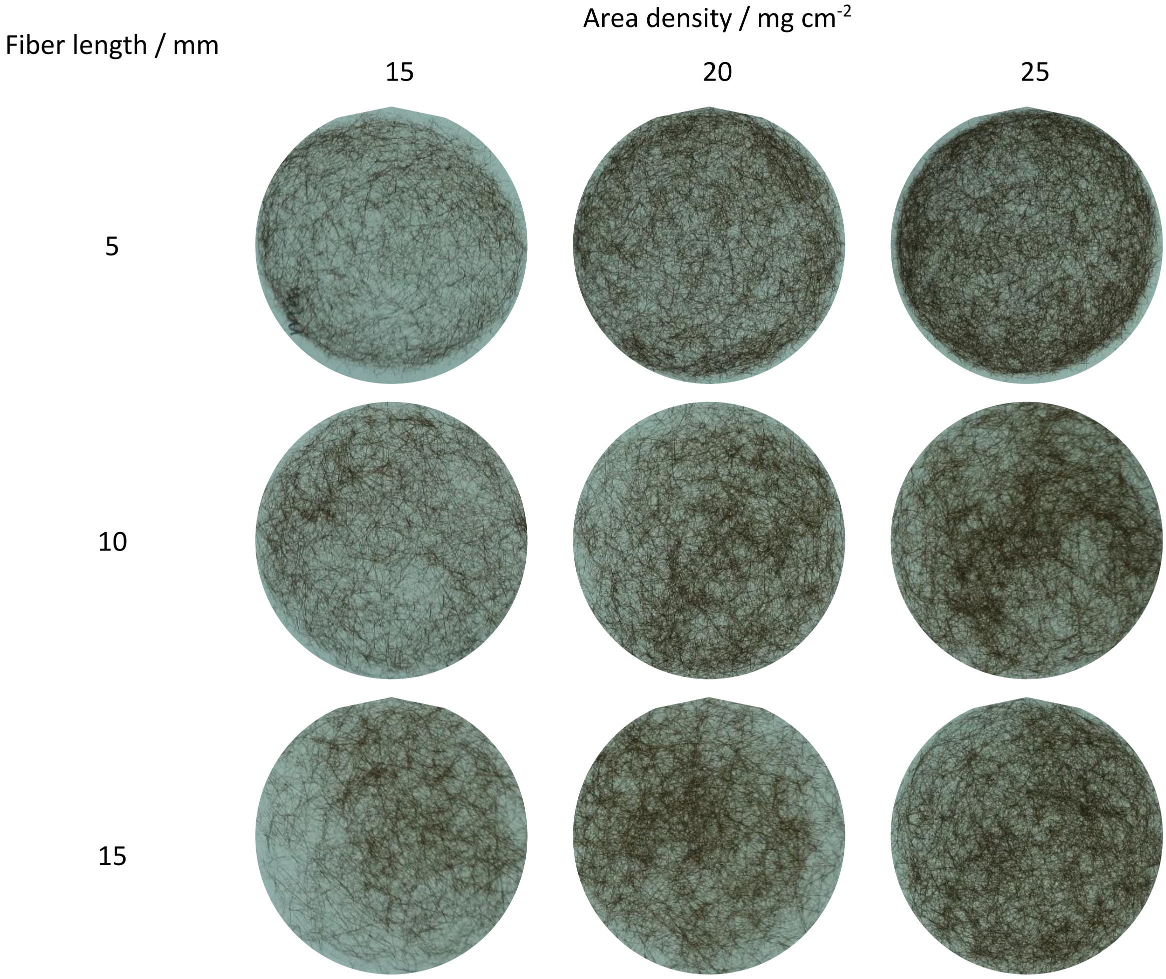

Figure 42: Area density and fiber length variation.

Table 5: Electric conductivity for area density and fiber length variation, respectively.

Fiber length / mm	Area density / mg cm^{-2}		
	15	20	25
5	0.8±0.1 S m^{-1}	1.5±0.2 S m^{-1}	287.4±19.8 S m^{-1}
10	1.7±0.3 S m^{-1}	129.5±57.7 S m^{-1}	1389±309 S m^{-1}
15	35.2±12.4 S m^{-1}	390.6±91.6 S m^{-1}	1667±67 S m^{-1}

The mechanical properties of the networks were measured for the highest area density of 25 mg cm^{-2}. Figure 43 shows the results of the tensile tests as well as their elastic modulus and their tensile strength. The lowest elastic modulus was found for the 5 mm fibers. This phenomenon originates from the lack of connection points between the fibers that would stabilize the network. The highest elastic modulus as well as the highest tensile strength were found for the 10 mm fibers. Regarding the number of connection points between the fibers, the highest values would be expected for the longest fibers. However, the reason for this behavior is depicted in Figure 44 featuring photographs of the networks at some special points. Both networks were practically the same before the tensile tests and the first difference occurs for the network elongated by 50 %. Here, the network with 10 mm fibers is torn apart in one line while the 15 mm network is just highly necked and still in good contact at the left side. Here, the homogeneity of the network comes into play. While the 10 mm network is highly homogeneous and all fibers are statistically distributed and, therefore, the mechanical properties are direction-independent, the 15 mm fiber networks shows areas with higher density. While the areas with lower density are much weaker and, therefore, break much earlier, the high-density area is still in contact and the complete network is only elongated. When the sample holder at the lower side is released, the residual elastic stress in the network pulls the network back together. Here, the residual stress for the 15 mm fibers is much higher than for the 10 mm fibers.

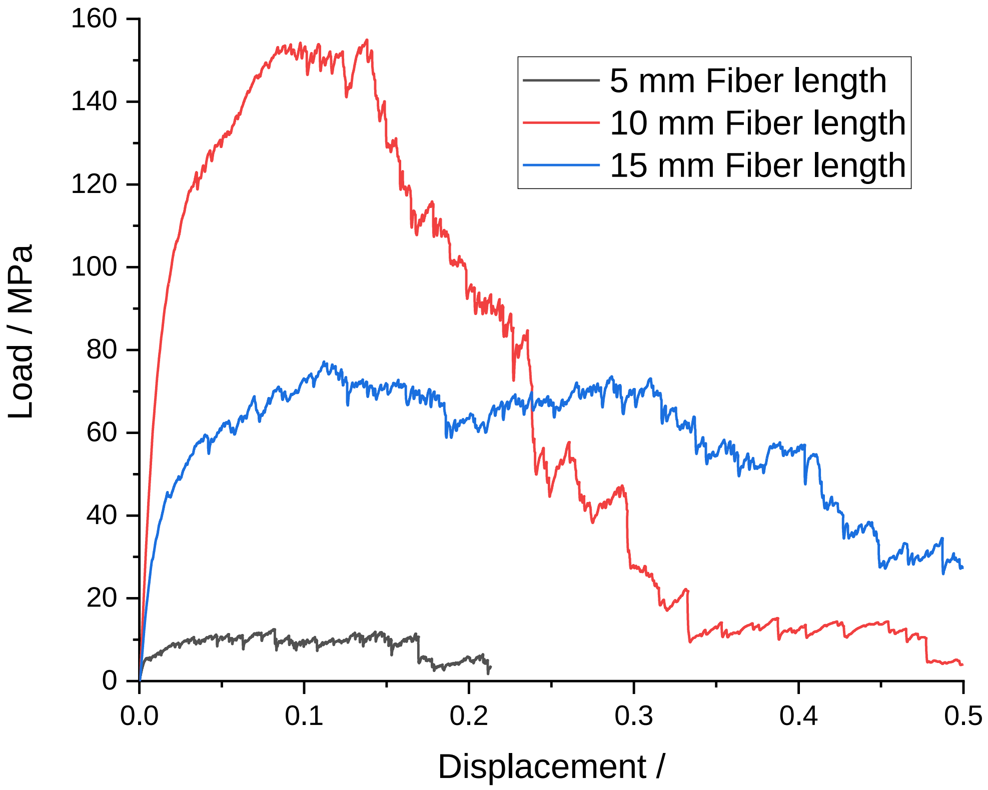

Figure 43: Tensile test for CuSi4 networks with different fiber lengths. The straight line at the begin represents the elastic network elongation, the unsteady line fiber cracks inside the network.

Therefore it can be concluded that in the first step the network is elongated while the fibers are pulled in a more parallel direction resulting in the network being elongated. In the second step, the fibers exposed to the highest stress break, which is visible as a small drop in the load displacement graph. For the 10 mm fibers, a few fibers are still connected with the upper and lower part. Whereas in the case of the 15 mm fibers the dense areas are still connected while the less dense areas are ripped apart. Depending on the application, either a high elasticity is better or a higher strength is more favorable. For our later application, a stable network with high homogeneity is needed, therefore, a compromise between mechanical properties and fleece laying homogeneity must be found. Considering the results from the different studies, the 7 mm fibers were found to be the most reliable.

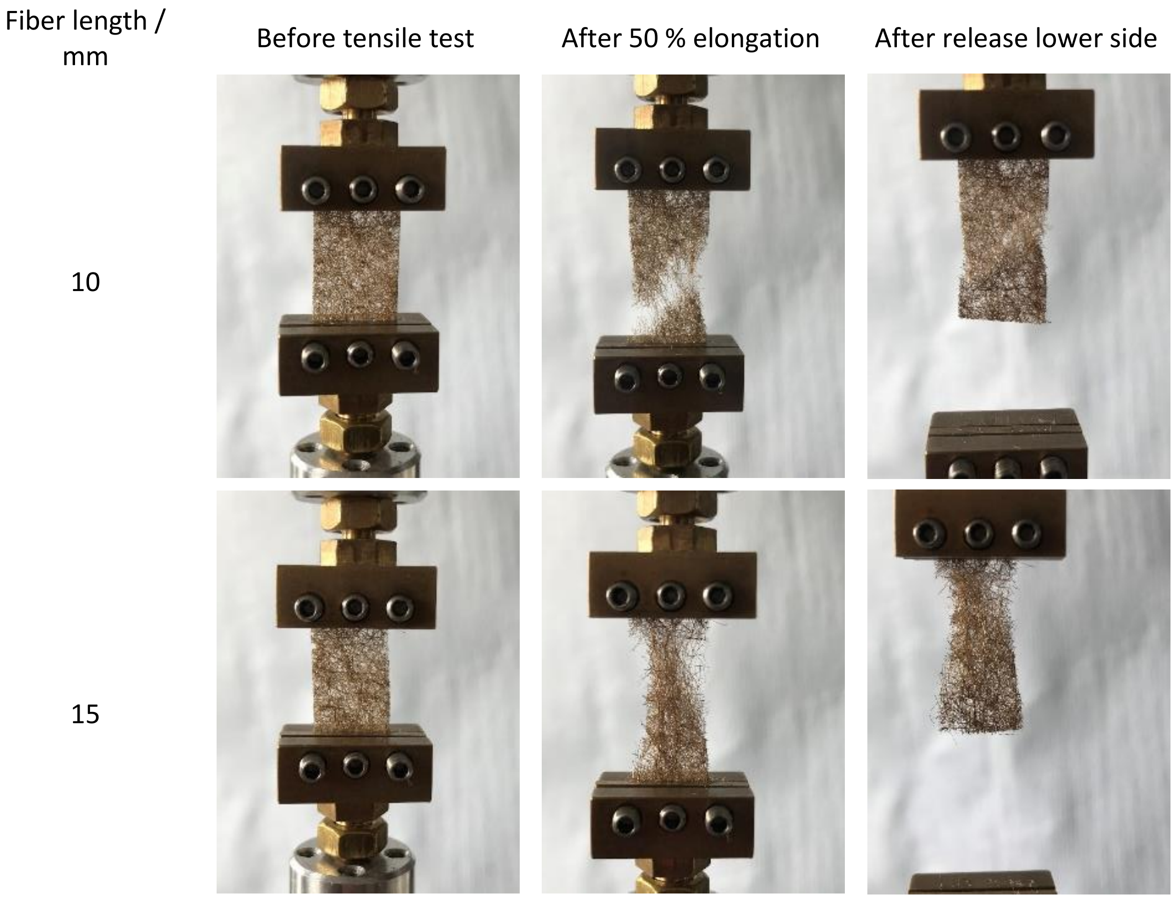

Figure 44: Pictures of networks with different fiber lengths during tensile tests.

A variation of the area density was tested for the networks with the 7 mm long fibers. Therefore, 20 mg cm^{-2} and 25 mg cm^{-2} were tested by tensile tests and their electric conductivity was also measured. Figure 45 shows the load displacement graph of both networks. As expected, the elastic modulus as well as the tensile strength is higher for the network with higher area density. Especially the elastic modulus is increased from 1.8 GPa for the 20 mg cm^{-2} to 10 GPa for the 25 mg cm^{-2} network. Additionally, the tensile strength is enhanced from 18 GPa to 83 GPa. Therefore, the network is highly suitable for the application as current collector for lithium-ion batteries. Both networks have an electric conductivity of around 71±1 S m^{-1} before the tensile test, again independent of the measurement direction. The conductivity of the 20 mg cm^{-2} network decreased to 17±4 S m^{-1} while the conductivity of the 25 mg cm^{-2} network decreased only to 54±7 S m^{-1}. This difference in the decrease can be explained by the different nature of the connection points in between the fibers. The connection points are equally high in the untreated state before the tensile test leading to the equal electric conductivity. For the 50 %-elongated state, the network with higher area density has more connection points left and, thus, a higher conductivity. Both conductivities are still relatively high and confirm the suitability of these types of fiber networks as electrically conductive matrices for several applications, for example, as current collector for lithium-ion batteries, also under high stresses and deformations.

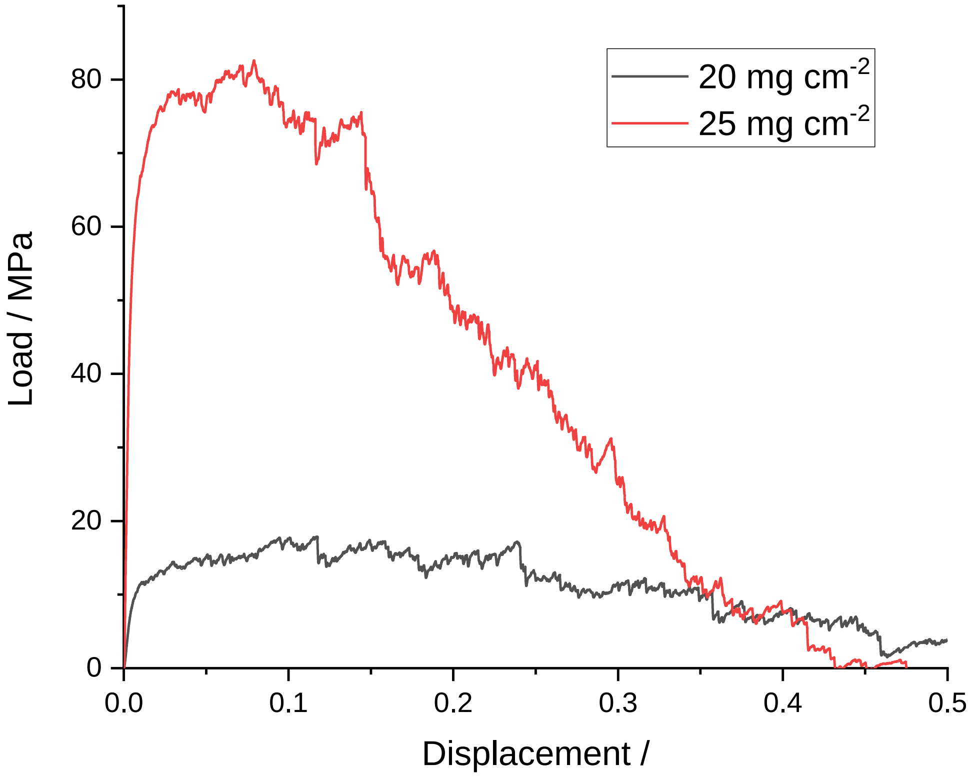

Figure 45: Load displacement graph for CuSi4 networks with 7 mm long fibers with different area density.

However, the carded networks exhibit different characteristics. Due to the more directed character of the fibers in the network, the mechanical properties and the electric conductivity depend on the measurement direction. Parallel to the fiber direction, a conductivity of 2373±55 S m^{-1} was measured for a sintered network with an area density of 25 mg cm^{-2}. This is nine times higher than the conductivity measured orthogonally to the fiber direction (254±27 S m^{-1}). This is based on the mechanism that along the fiber direction there is a direct connection from one electrode to the other following a single fiber without any sintering points or longer paths through junctions. In addition, the elastic modulus parallel to the fiber direction was measured as 4.2 GPa and is 4.6 times higher than for the measurement direction orthogonal to the fibers direction (0.9 GPa). Along the fiber direction, the elastic properties are mainly influenced by the elastic modulus of a single fiber and not by sintering points. Therefore, the elastic deformation is much lower due to the lack of necking of the whole network. Orthogonally to the fiber direction, fewer fibers and connection points are holding the network together, therefore the tensile strength is much lower at 47 MPa than the tensile strength parallel to the fiber direction with 139 MPa. Farley investigated with simulation methods the relationship between fiber diameter, volume fraction, and the resulting mean pore size based on the fibers and manufacturing strategies described in the present work. [183] Figure 46 shows the resulting heat map of the simulations. Here, round fibers similar to the fibers after sintering with rounding were simulated. With this heat map, the resulting porosity of the network can be predicted and therefore the production adjusted to obtain the wanted pore size.

With the help of the data from the simulation, a network of fibers with 50 µm width before sintering was produced. After sintering with rounding the fibers have a diameter of around 20 µm. With a view to the later application as current collectors for lithium-ion batteries, a pore size of around 150 µm should be obtained which requires 4 vol.-% fibers in the networks. The resulting network is shown in Figure 47 a) as a micro-CT scan (Skyscan 1272, Bruker Inc.). Figure 47 b) depicts the pore size distribution of the network (Euclid circles method, GeoDict, Math2Market GmbH). Pores over 250 µm are mainly open porosity on the network surface and will not be considered. As expected, a mean pore size of around 150 µm was achieved which follows along the predictions of the simulation. A pore size distribution is visible in the data and also correlated to the micro-CT picture. This distribution occurs due to variations in the fiber size and inhomogeneities during the network manufacturing, mainly in the dispersing step.

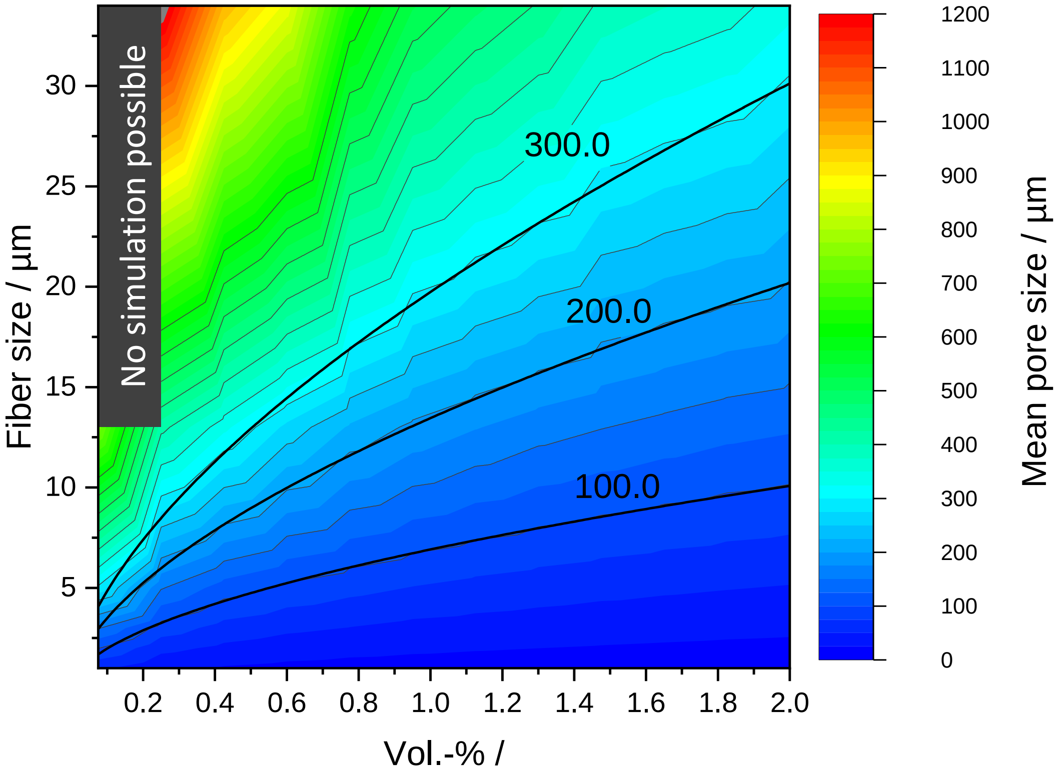

Figure 46: Heat map of the correlation between fiber size, volume fraction, and mean pore size. [183]

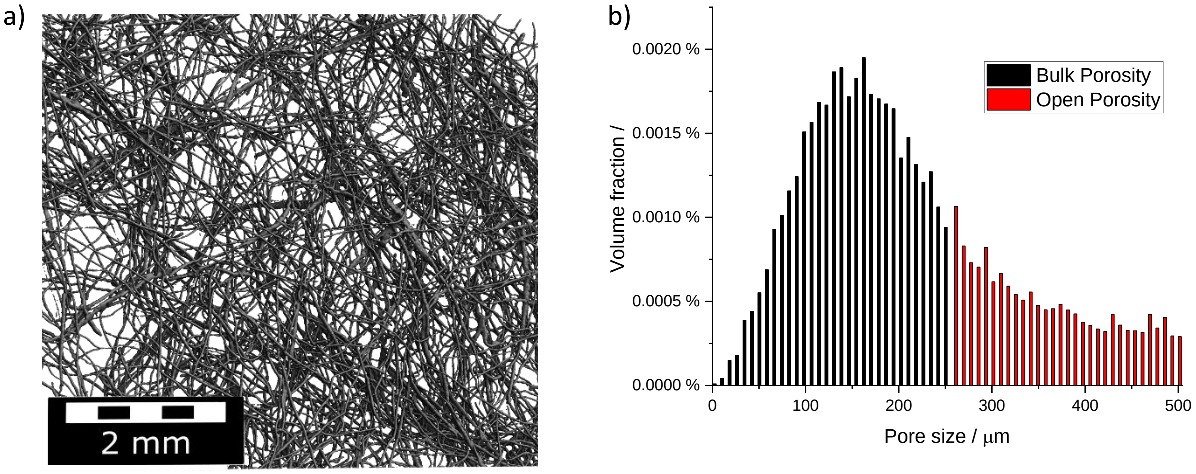

Figure 47: a) micro-CT scan of a dispersed network and b) the resulting pore size distribution.

In summary, the properties of dispersed and sintered metal fiber networks with a fiber length of around 7 mm and an area density between 20-25 mg cm^{-2} are highly attractive as a mechanically stable and electrically conductive backbone for several applications. The pore size after sintering can be tuned with the simulated heat map depending on fiber diameter and volume fraction to produce the required pore size. The manufacturing strategies described in the present work are highly suitable for the precise manufacturing of networks with predetermined pore size.

4.3. Sintered 3D fiber networks as current collectors in Lithium-Ion Batteries

The current trend in lithium-ion battery technology focuses on thicker electrodes to reduce the fraction of inactive components in the battery. [27] However, there are still several challenges that have to be overcome. The three most important ones are: the electrical conductivity of the electrode, the lithium-ion diffusion through the electrode, and the mechanical stability of the electrode. 3D current collectors are one approach to solve these problems and obtain thicker high-performance electrodes. In this section, the improved electric conductivity obtained by the 3D fiber networks on the electrode is discussed with a focus on less overpotentials and potential gradients in the network. The increased lithium-ion diffusion inside the networks will be investigated in comparison with other additives or no additives at all in thick electrodes. In addition, the improvement of the mechanical stability of the active material and of the electrode as a whole can increase the lifetime of the battery significantly. With the switch from a 2D to a 3D current collector, the foil normally used on one side of the active material bulk is replaced by a 3D structure inside the completely active material bulk. In this case, the 3D structure is a fiber-based sintered 3D network of CuSi3 fibers. CuSi3 is suitable for this application due to its high electric conductivity and no electrochemical activity in the voltage window of lithium-ion battery anodes. This section should be understood as proof of principle of the whole system with explanations of the main principles and improvements of the 3D fiber-based current collector network.

Parts of the discussed experiments, findings as well as graphs and images in this section are part of the patent and patent applications [178, 184, 185].

4.3.1. Electrical Conductivity

The thickness of the active material is one of the main parameters influencing battery performance and general characteristics. While thin active material layers can be charged faster, thicker electrodes have a higher capacity due to a lower portion of inactive materials. However, the electric conductivity drops to values too low to achieve sufficient bulk conductivity when approaching a certain thickness. In normal 2D setups, a linear gradient though the active material occurs. Therefore, the voltage is higher at the active material close to the metal foil and is decreasing towards the separator. Table 4 shows the electric conductivity of several active materials and also typical conductive additives. While graphite has a relatively high electrical conductivity, the values for the oxide active materials are rather low. Therefore, the amount of conductive additives is increased with decreasing active material conductivity.

Table 6: Electric conductivity of typical lithium-ion components.

	Electric conductivity / S m^{-1}
Graphite (parallel to layers) [186]	10^6
LTO [187]	10^{-5}
NMC622 [188]	10^{-1}
Carbon nanotubes [189]	10^6
Copper [148]	10^7
Aluminum [148]	10^7

Figure 48 shows the simulative potential gradient in a) a standard 2D foil electrode, b) a 2D foil electrode with carbon nanotubes, and c) with a sintered CuSi3 network as discussed in this work. The simulation is based on a simulated 3D fiber network with comparable parameters based on the networks in this work. [183] For all electrodes, a voltage of 1 V was set at the left side while the separator and counter electrode on the right side were set to 0 V. The standard 2D foil electrode exhibits a potential drop that is linear through the material. For the electrode with carbon nanotubes, the potential drop is flatter at the start but increases towards the separator. For the copper network, nearly no potential drop is visible in the electrode; a strong drop is only visible at the separator to which the 0 V are applied. This shows impressively the convincing suitability of the 3D fiber network as current collector for lithium-ion batteries presented here.

However, for the sintered metal fiber networks the sintering itself is crucial. Carbon nanotubes are the most common additive for a 3D battery. These carbon fibers are just in loose contact with each other in the active material bulk. [33] In an ideal case, the fibers have direct contact to each other but in the most cases, there is no direct contact between the fibers. To test the influence of the contact points, the dispersed networks were tested before and after sintering. Before sintering, an electrical conductivity from 89 S/m was measured which increases during sintering to 1242 S/m. These measured values are much lower than the theoretical values, which can be explained by the non-ideal contact between measurement electrodes and the porous structure of the fibers during the 4-point measurement. In graphite electrodes, the conductivity of the graphite matrix is high enough for a good conductivity. In cases with oxide active materials like LTO or NMC, the active material works as an insulator (see Table 6). Therefore, the connection between the fibers is more important for electrodes with oxide active materials. Hence, a conductive binder inside the matrix helps to overcome the isolating interfaces between the conductive additives.

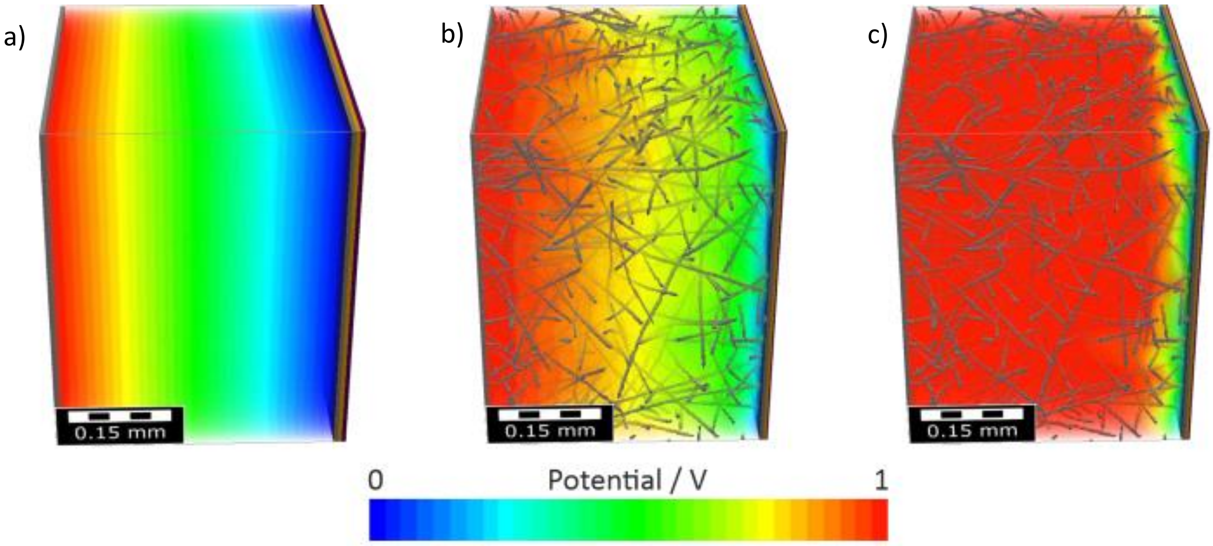

Figure 48: Gradient simulation of a) a standard 2D electrode, b) a 2D electrode with carbon nanotubes and c) a 3D copper current collector electrode. [183]

Two parameters are influencing the potential gradient inside fiber network electrodes or, in general, all 3D electrodes. The first is the amount of the conductive additive, the second is the conductivity of the conductive additive. Both was simulated by Farley in his work. [183] Figure 49 shows the results of the simulative variation of the amount of the fibers and the conductivity. The lower the amount of fibers and the lower the conductivity, the stronger the potential gradient. For the highest conductivity of the fibers, the gradient is also for the 0.6 vol.-% of fibers nearly not happen. For all simulations, an equal network structure was used for every volumetric fiber fraction. For this network structure, the material conductivity was changed. The highest simulated conductivity is in the range of the used CuSi fibers. For the second highest conductivity, which is around the range of carbon nanotubes, only the highest amount (2.0 vol.-%) exhibits a gradient low enough for good electric conductivity in a thick electrode. For lower conductivities, the thickness of the electrode is very limited due to the strong gradient inside the electrode. Therefore, only metallic structures are suitable for thick electrodes. Comparable systems are metal foams or fibrous metal structures which are much more difficult to manufacture. Furthermore, applying a precise set of parameters like the pore size is much more complicated compared to the system described here. [7, 32, 33, 190]

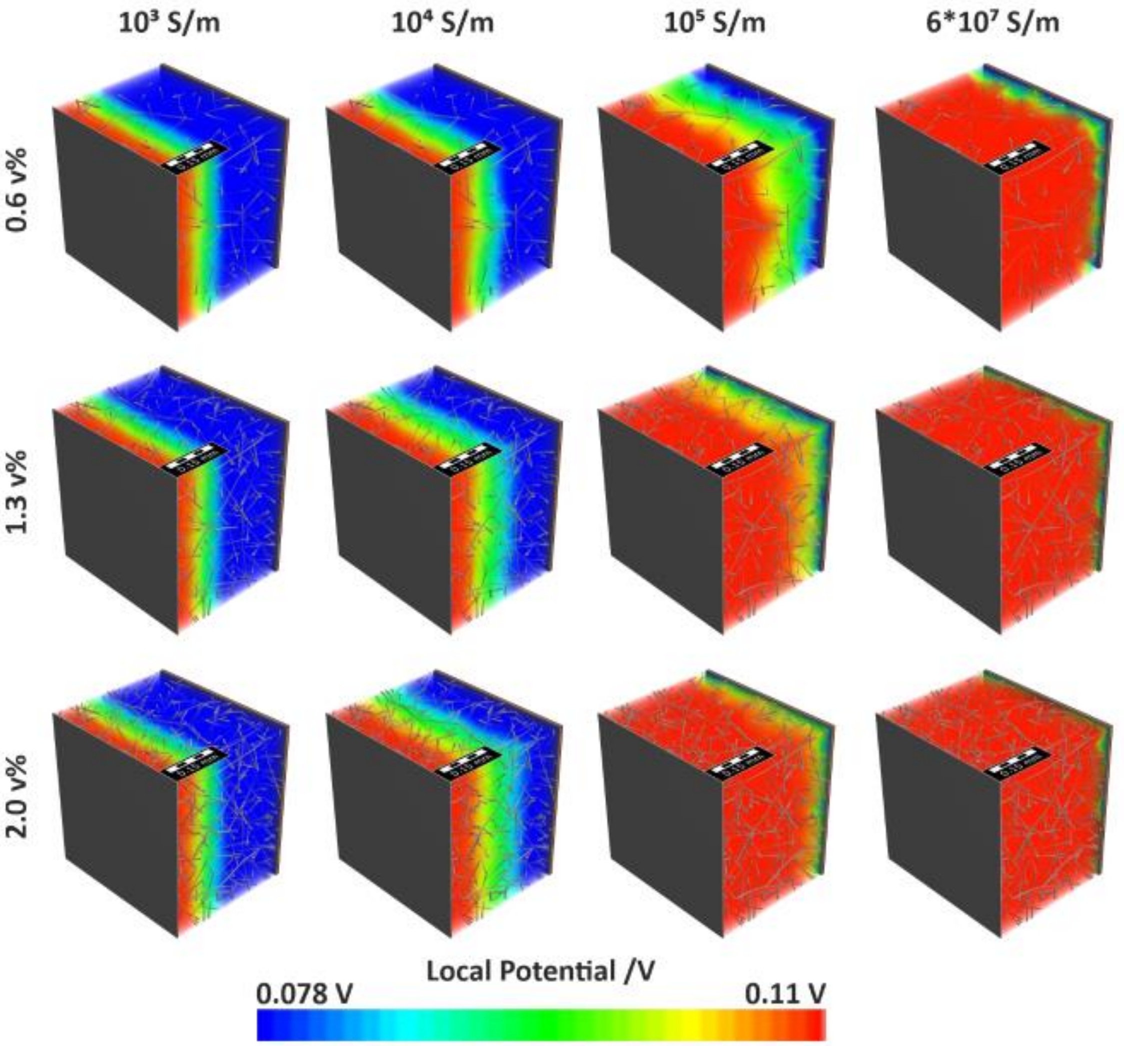

Figure 49: Simulative variation of fiber fraction and conductivity in thick electrodes. [183]

To validate these simulative results, electrodes were measured with EIS to investigate the electric resistance of the electrode. Since the most common anode active material is graphite, graphite electrodes were measured in half-cell configuration with EIS at a cell voltage of 0.143 V. Figure 50 shows the resulting Nyquist plot of two thick 3D electrodes and two 2D electrodes with a typical thickness of 40-60 µm. The electrical resistance is several times lower for 3D electrodes compared to the 2D electrodes. The contact resistance, mainly influenced by the contact between electrode and case, is equal for both systems. Apart from the current collector structure, also thickness, capacity, and porosity are different for both electrode systems. While for the 2D electrodes normally a residual porosity of around 10-15 % is present, the porosity is in the range of 50 % for the 3D electrodes without calendar treatment. Ogihara *et al.* described in their work the influence of the porosity on thick electrodes using EIS. [191] They described the internal resistance of an electrode as the sum of the resistance of the electrolyte R_{ion} and the charge transfer resistance R_{ct} of the active material. Both are expressed by equation (24) and (25):

$$R_{ion} = R_{ion,L} \cdot \frac{L}{n} \qquad [191]\ (24)$$

$$R_{ct} = \frac{R_{ct,A}}{2\pi r L} \qquad [191]\ (25)$$

where $R_{ion,L}$ is the ionic resistance per unit pore length L, n a natural number, $R_{ct,A}$ the charge transfer resistance per unit electroactive surface area $2\pi rL$. While the charge transfer resistance is decreasing with higher thickness, the ionic resistance is increased. Additionally, the reactive surface is increased with a higher amount of active material as well as with a higher porosity. Therefore, it is not possible to directly compare both electrodes phenomenologically. In total numbers, the internal resistance of 3D electrodes is several times lower compared to 2D electrodes with the same active material.

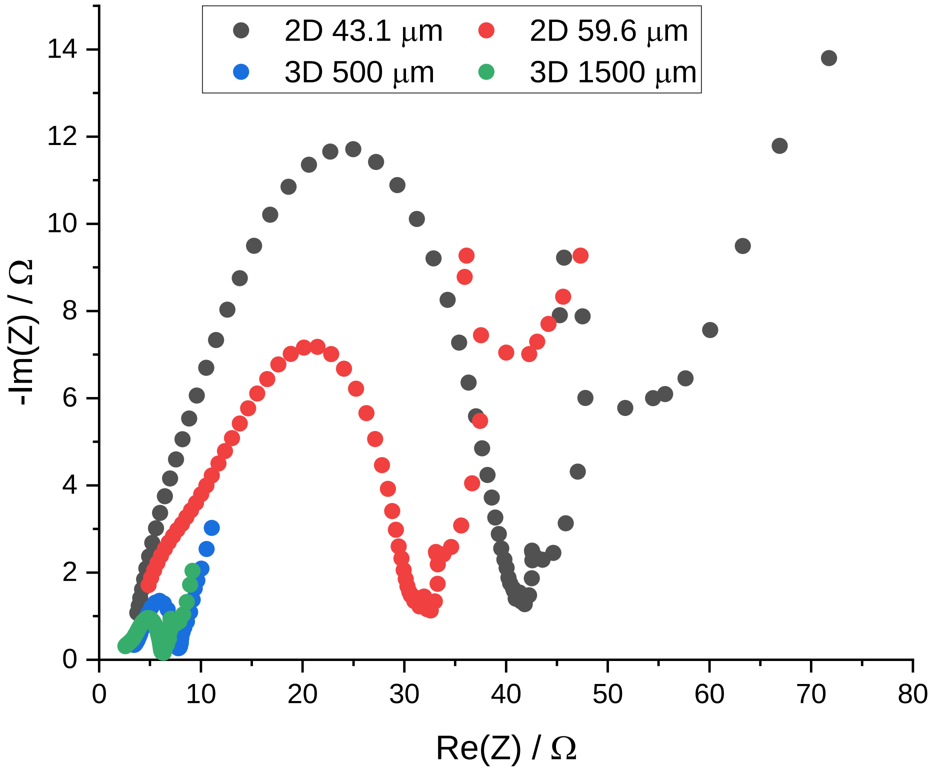

Figure 50: Nyquist plot for 2D and 3D electrodes in several thicknesses.

The lower internal resistance results in less overpotentials and higher fast-charging probabilities. Hence, the heat production is lowered as it is based on overpotentials and resistance heating of the electrode. [192] The overpotentials not only result in thermal energy, they can also initiate decomposition of the electrode - one of the strongest influencing factors for battery aging. [193] Overpotentials can be seen directly (green circle) in the loading curve of an electrode, which is given in Figure 50. Here, a 2D and a 3D electrode were loaded after formation with a loading speed of 0.5 C. Although both loading curves are nearly equal after a 0.1 state of charge (SOC), the 2D electrode shows a high overpotential of around 0.05 V. This overpotential is visible for the first 10 % of the battery capacity. The integral of the overpotential is energy which is not used for loading the battery. Not only from a thermal management point of view is this not promising, but also from energetically as the efficiency of the battery is decreased. Overpotentials cannot only decompose the electrode and the electrolyte thermally, the local potential peak can decompose the electrolyte also electrochemically. Especially, for active materials with significant lower conductivity like LTO or NMC, this effect is distinctively pronounced. Reason for this is the low electric conductivity of the active material and, therefore, a high potential gradient in the network with an overpotential next to the current collector.

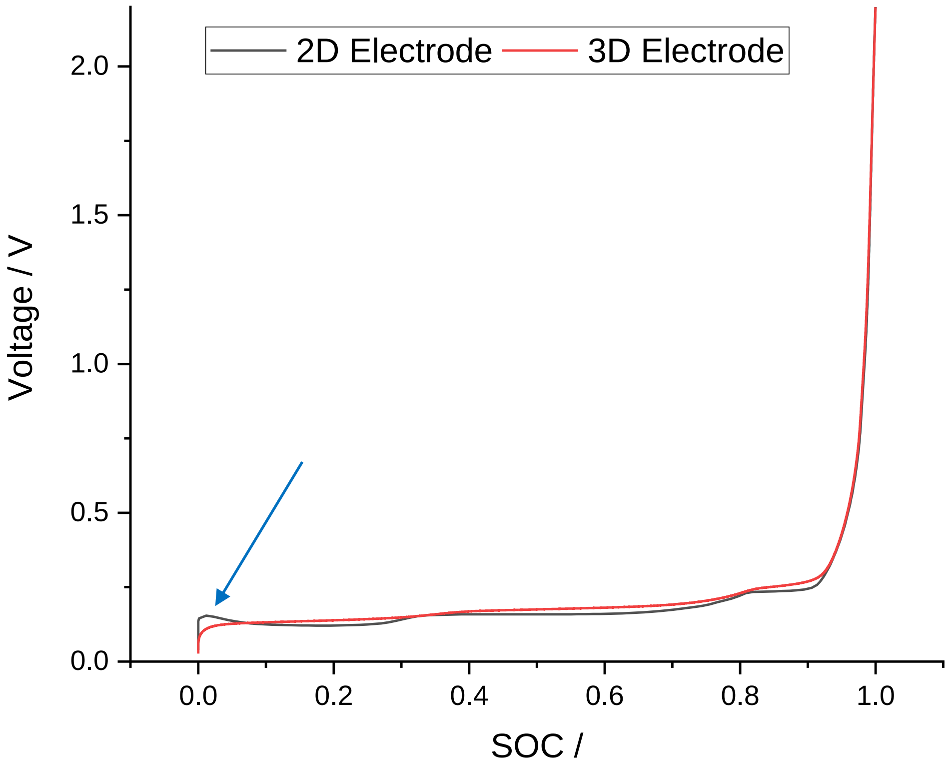

Figure 51: Overpotential (marked with a blue arrow) while loading a 2D and a 3D electrode.

Another limiting factor for the loading rate can be assigned to bulk conductivity. As shown in Figure 49, the voltage is decreasing the farther away the active material is located from the current collector. Therefore, the active material next to the current collector can already be fully loaded while the active material farther away is still not loaded. As the cell voltage is always measured at the current collector, the active material next to it is already loaded while active material with a higher distance is not yet loaded due to the low conductivity. The voltage is increased at the current collector and the loading electronic stops the loading process to avoid overloading and, thus, damaging the electrode, while only the active material next to the current collector is charged and not the whole active material. Because of this an additional constant voltage loading step is applied at the end of the loading in most of the applications. This results in an only partially loaded battery. The loading gradient is equalized with time and the consumer shows a partially loaded battery. With a dynamic loading rate the partial loading because of potential gradients can be suppressed. As the slower loading range regions exhibit a smaller potential gradient compared to fast charging rates, the loading rate is lower in the beginning and increases when the battery charges up. [194] As already mentioned before, significance is increased for active materials with lower electrical conductivity and, thus, is not needed for 3D CuSi3 current collector batteries.

4.3.2. Lithium-Ion Diffusion

The second important transport mechanism inside lithium-ion batteries is the lithium-ion diffusion. While the diffusion coefficient from lithium ions in graphite is in the range of 10^{-13} m^2 s^{-1} [195] the value for a typical electrolyte like $LiPF_6$ in EC:DMC (50:50) is in the range of 10^{-10} [196]. Therefore, it is promising to transport the lithium ions as far as possible inside the electrolyte before entering the active material. Hence, a highly connected porous network would be beneficial for several reasons. Firstly, the lower volumetric capacity of the cells which is mainly an application problem. The high porosity presents space in the consumer which is not used for energy storage and, therefore, not preferred. Secondly, the lower electric conductivity caused by thicker layers and less contact points between conductive additives. Currently, pseudo all-solid-state batteries with a gel electrolyte are an up-to-date research topic. These gel electrolytes have a much longer lifetime but require a larger and connected porosity inside the active material bulk. [17, 197, 198] Here, 3D current collectors are a promising pathway to introduce a solid-state electrolyte while the electrical properties remain the same. [199] If the solid-state electrolyte is not penetrating the whole active material, the overall lithium-ion diffusion is low due to the low diffusion inside the active material and, thus, the loading rate is decreased. It should be also mentioned that for an active material bulk without any porosity the diffusion interface (separator) is at the opposite site of the 2D conductive interface (current collector) inside the electrode.

In graphite-based anode systems with a 3D CuSi3 fiber network current collector, diffusivity is increased compared to normal 2D electrodes. This diffusion can be measured with EIS and the results are given in Figure 50 as the linear part at the right side of the measurement curve. The Warburg coefficients were fitted from these curves and are plotted against the electrode thickness in Figure 52. The Warburg coefficient is reciprocally proportional to the diffusion coefficient which means the lower the Warburg coefficient, the higher the diffusion. The diffusion is reportedly decreasing with increasing thickness for different 2D thicknesses, whereas the diffusion inside the 3D electrodes is apparently not influenced by thickness. [200] The tested 3D electrodes are several times thicker than the tested 2D electrodes, nevertheless the Warburg coefficient is around eight times lower for 3D electrodes. There are several explanations for this behavior: One is the low tortuosity due to the metal fibers in the active material and the possible small gap between fiber and active material. Another is the increased porosity in the active material. Therefore, a set of equal electrodes were calendered to decrease the porosity as well as the electrode thickness. In contrast to the electrodes from Figure 50 and Figure 52 these electrodes were tested not in half-cell configuration versus lithium but as symmetrical cells. This allows the exclusion of a possible influence of the metallic lithium but makes the measurements only comparable within one measurement series. As shows, the Warburg coefficient is independent of porosity and thickness of the 3D electrode. Therefore, the metallic 3D structure inside the active material must be the reason for the higher diffusivity in the electrode.

Jia *et al.* described in their work a surface mechanism based on defects, which increases the diffusion for nanowires. [201] They combined surface effects and chemical diffusion for an advanced model that describes the increased diffusivity more exactly than existing models based on the surface elastic theory. [202, 203] An overall mechanism for all these models is the surface-induced traction due to the surface free energy. The fibers used in this work have a non-round cross-section and therefore the surface free energy is increased compared to round fibers. Additionally, the non-ideal crystallographic state with a high defect density increases the free energy of the system. Therefore, the used fibers are a possible candidate for the models to describe the increased lithium-ion diffusion. In comparison to nanowires, which are loosely introduced in the active material bulk, the fibers in the metal network here are connected with each other and thus the pathways are not interrupted. Rupp *et al.* were able to show that on the surface of a planar copper current collector a higher lithium diffusion occurs. [204] In the case of 2D electrodes, this is not influencing the electrode performance because of the orthogonal ion flux. In the case of 3D metal networks, the fibers are penetrating the active material bulk with a statistic distribution in which every direction is represented by a fiber and surface diffusion can occur in any direction.

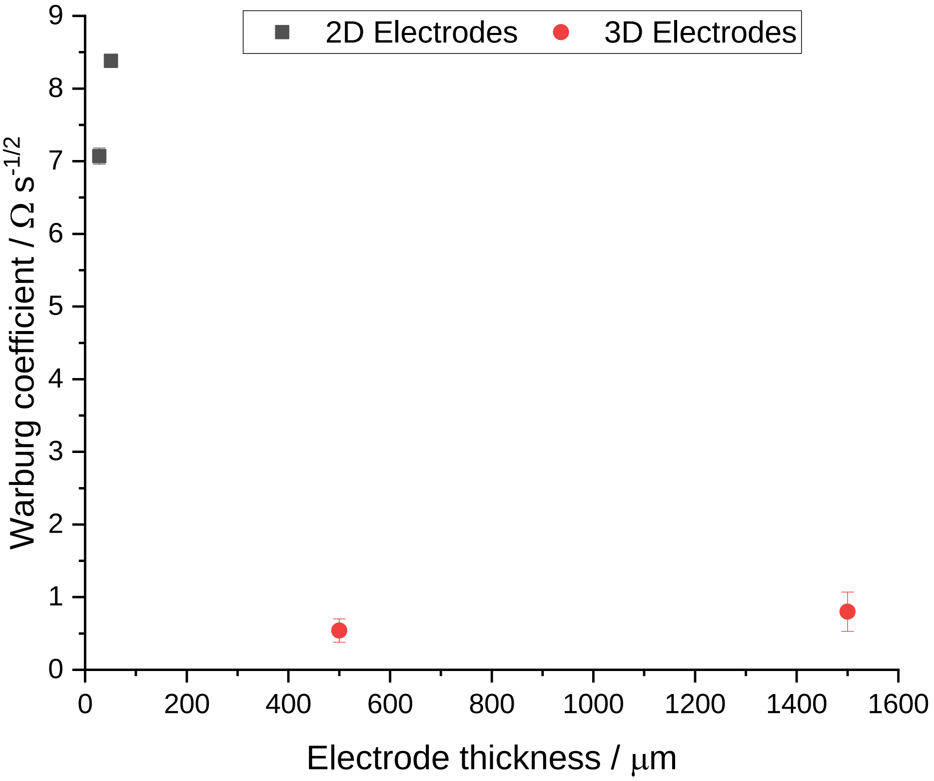

Figure 52: Warburg coefficient for 2D and 3D electrodes with different thicknesses.

While the hurdle of low electric conductivity inside an electrode towards fast charging electrodes can be overcome with conductive additives and more conductive active materials, increasing the lithium diffusion is more challenging. However, both mechanisms must be considered equally. While the free charge carriers during intercalation processes must be diverted without overpotentials, the lithium ion is needed for intercalation at the same point in the bulk. Therefore, a strategy that combines both approaches would advance the development of fast charging batteries.

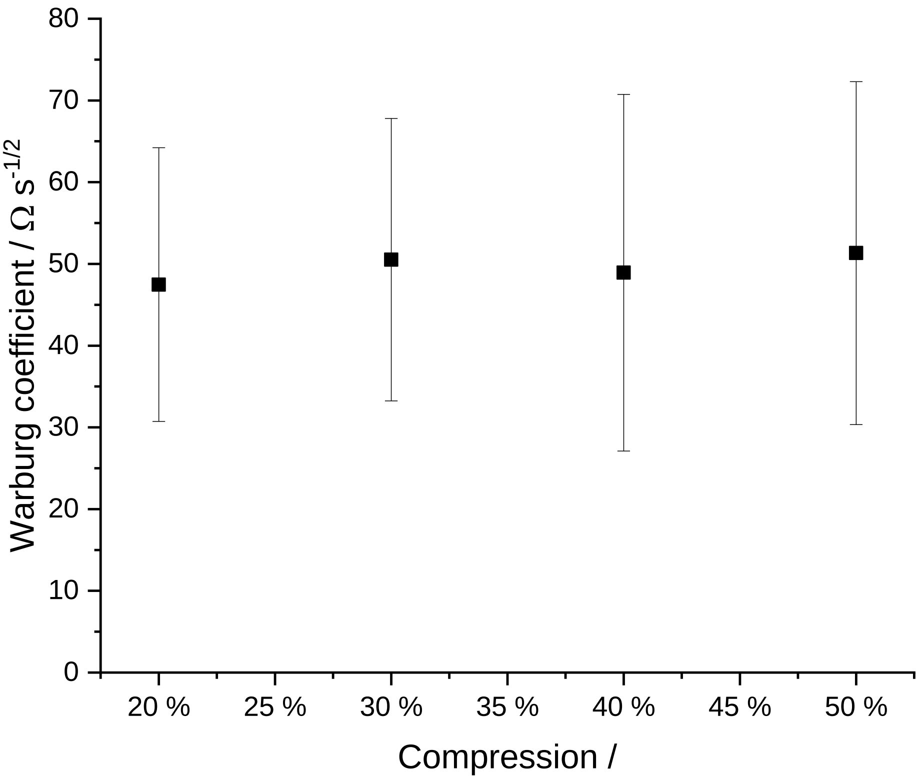

Figure 53: Warburg coefficient for electrodes with different compression states.

4.3.3. Mechanical Stability

Another significant property of an electrode is its mechanical stability. However, a distinction must be made between two types of stability. On the one hand, there is the macroscopic stability of the whole electrode, on the other hand is the stability of the active material within the electrode.

The focus will be first on the macroscopic electrode stability. Especially during the manufacturing of a cylindrical cell, but also for other types of batteries, the stress on electrodes is enormous. While the electrodes are pulled through roll-to-roll fabrication machines, not the tiniest defect is permitted. [205] Super-thin metal foils in the thickness range around 10 µm are not known for their high stress resistance. Even small cracks can lead to dangerous potential peaks that can then decompose the electrolyte. This happens frequently when the electrode gets stuck inside the manufacturing machines. These small metal foils will crack or tear without any remarkable elastic deformation. [206]

It has been shown that metal networks are able to tolerate a high elastic deformation without cracking and even after a large deformation are still electrically conductive. Therefore, CuSi networks with a graphite-based slurry were tested with tensile tests. The results are shown in Figure 54. A deformation of more than 1 % without cracking was measured for the 20 mg cm^{-2} metal fiber network electrode and more than 2.5 %. for the 25 mg cm^{-2} electrode. An elastic modulus of 1.3 GPa for the 20 mg cm^{-2}

metal fiber network and 1.8 GPa for the 25 mg cm^{-2} network was determined. Furthermore, the tensile strength increased from 7.6 MPa to 13.0 MPa with increased current collector area density.

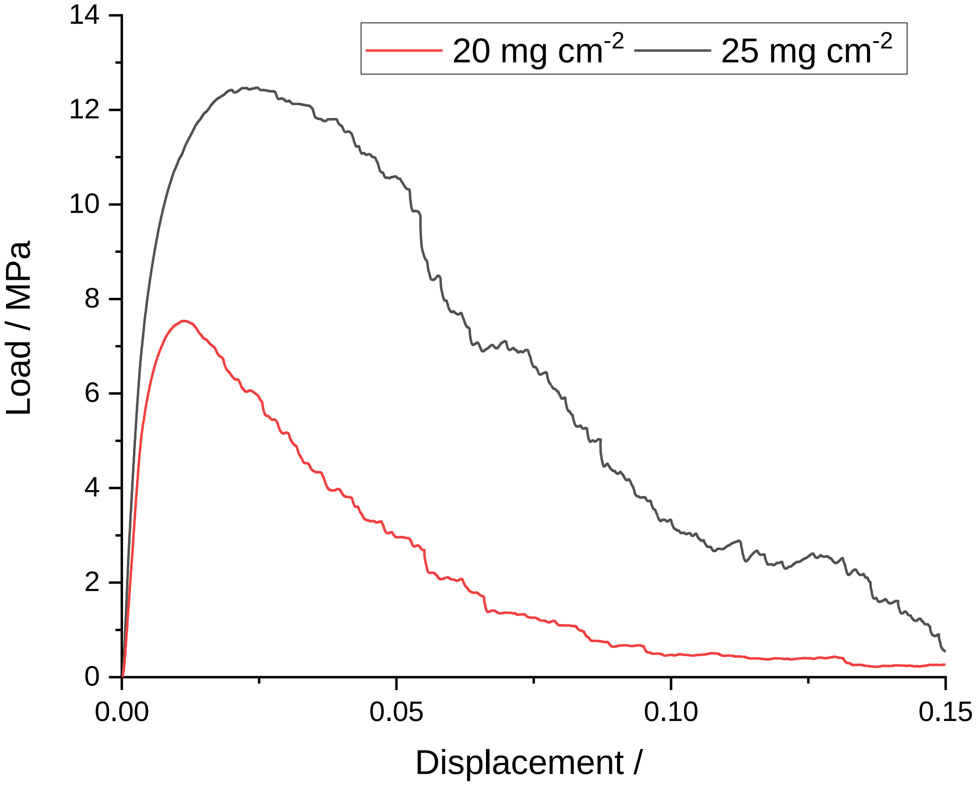

Figure 54: Tensile tests on CuSi network electrodes with graphite-based slurry.

To prove the resistance against a deformation-induced conductivity decrease, the electric conductivity was measured before and after a 25 % elongation. For the low current collector density, the conductivity decreased from 91 S m^{-1} to 27 S m^{-1} and for the higher current collector density from 333 S m^{-1} to 86 S m^{-1}. For the same samples, the weight before and after the experiment were measured. An active material loss of less than 1 wt.-% was observed for all tensile test samples. For similar experiments with 2D electrodes, nearly all the active material detached from the current collector foil.

The stability of the active material on the current collector is a severe problem, especially for active materials like graphite or silicon. While graphite is increasing its volume by around 8 vol.-% [207] during loading, silicon increases by around 400 vol.-% [208]. The active material in planar 2D electrodes sticks to the foil due to the binder. While loading the active material, the connection to the current collector or to other active material can fail due to the volume enlargement. Therefore, a high amount of binder inside the active material is needed which in turn decreases the ratio between active and inactive parts inside the electrode. [209] The thicker the active material coating, the more urgent this problem becomes. Since the loose active material cannot be loaded, the capacity of the battery decreases. Even more problematic is the creation of short-circuits by the active material inside the electrode.

A second force beside the binder is keeping the active material on the current collector in 3D current collectors. The fibers can keep the active material particles together from several sides, in other words, the active material is trapped in the network pores. The metal fiber network is an elastic structure; which can expand or contract together with the active material depending on the loading and unloading cycle. Hence, the connection between current collector and active materials is not stressed and the structure remains intact. This can significantly increase the cycle stability of the battery.

Due to the second holding force, the binder can be reduced inside the electrode. 3D electrodes and, as a control experiment copper foils, were coated with an adjusted graphite-based slurry. Hence, the binder and carbon black fraction were reduced at the same ratio. Table 7 shows the results of kinking tests for 2D and 3D electrodes. For the kinking tests, the electrode was placed between two linear tweezers and kinked in a straight line 90° to one side, 180° to the other side and back in the original position. Only the binder fraction is indicated for reasons of clarity. For the 2D case, not only detached material is taken into account but also detached parts of the active material. For 2D and 3D electrodes, the area 3 mm left and right of the kink was taken into account. For all binder fractions, the active material loss is much lower in the case of 3D electrodes. This shows impressively the strong influence of the structure on the active material stability and the possibility to decrease the binder fraction. The stability during deformation makes the 3D fiber current collector electrode also applicable as an electrode for flexible batteries. Here, a much more flexible electrode structure is needed compared with normal applications. [210, 211] All 3D electrodes with different binder fraction were cycled with 0.5 C for 100 cycles to prove the cycle stability. For none of the batteries, a detachment event was visible with comparably good cycle performance.

Table 7: Kinking tests on 2D and 3D electrodes with binder fraction variation.

Binder fraction / wt.-%	2D active material loss / wt.-%	3D active material loss / wt.-%
10	3	0
8	11	0
6	32	0
4	79	3
2	100	9

4.3.4. Electrochemical Performance

In the previous sections, the different properties of the electrodes were examined without relation to the other properties. Therefore, the general performance of the cells needs still to be investigated. However, the good electric conductivity combined with the increased lithium-ion diffusion and the high mechanical stability shows that the system is highly suitable as lithium-ion battery electrodes. In this section, the electrochemical performance of the electrode is discussed based on the previously mentioned properties.

All the challenges discussed before represent also the key challenges for Kuang *et al.* in their work. [27] They describe not only the need for 3D current collectors as a possibility for classic lithium-ion batteries, they also describe the 3D electrode design for future battery technologies in the form of substrates for metallic lithium anodes. With an increase of the electrode thickness from 25 µm to 200 µm, the fraction of inactive materials (28 vol.-% separator, 17 vol.-% current collector) can be reduced by one third (6 vol.-% separator, 6 vol.-% current collector) [27]. Calculations for the fiber electrodes showed that with the change from a thin-layer 2D current collector to a 3D fiber current collector with a 10 µm fiber size, 200 µm pore size, and an electrode thickness around 400 µm, the improvement is much bigger. The inactive material fraction can be reduced from around 7 vol.-% or 27 wt.-% to 5 vol.-% or 8 wt.-%, respectively, while the gravimetric energy density can be increased by 23 % and the volumetric by 33 %. This is a big step towards future high-performance batteries.

Another problem for thick electrodes is the slow charging rate or vice versa the small discharging current. The all-pervasive fiber network helps to create a super-parallel circuit in the battery. Tests with NMC/graphite pouch cells with the same capacity and thick 2D electrodes showed a seven times higher discharge current. Especially for applications which require high currents, this represents a unique possibility for a high-power high-energy battery.

In order to compare 2D and 3D electrodes, electrodes with an equal area capacity of 2.9 mAh cm^{-2} and an equal slurry were produced and cycled as half-cells against metallic lithium with 0.5 C. The results of these cycling experiment are shown inFigure 55. The state of charge (SOC) of the 2D electrode drops to around 20 % and is later increasing towards around 40 %, which is a typical value for electrodes of this thickness. [11, 212] For the 3D electrode, the SOC is dropping again during the first cycles to around 40 % increasing to 55 %. The drop at the first cycles is mainly caused by an incomplete SEI formation. [213] The low SOC in general is typical for graphite electrodes due to the low lithium-ion diffusion with long pathways inside the graphite particles. [11] The battery performance is highly influenced by the active material thickness due to the strong impact on the lithium-ion diffusion and electric conductivity. The tested network had an average pore size of around 160 µm, so the largest distance to the next current collector is 80 µm. Hence, the cycling performance is comparable with a 2D electrode with an active material thickness of 80 µm, while the 2D electrode tested here has an active material layer thickness of around 158 µm.

showing an additional measurement for a 2D 98 µm active material layer can be found in the appendix as Figure A 11. This shows impressively the power of the technology discussed here. With the simulation provided in Figure 46, it is possible to tailor the pore size diameter precisely to achieve the optimum network geometry for every application. Thus, a battery loading and unloading performance with much higher gravimetric and volumetric capacity can be realized.

Tests with super-thick electrodes showed a very strong increase in area capacity. Figure 56 shows several data points for thick 3D fiber electrodes with graphite as active material. For all electrodes, fibers with around 20 µm in diameter were used and the pore size was set to around 160 µm. As expected, a nearly linear increase of the area capacity with the electrode thickness is visible. For 2D electrodes, area capacities above around 5 mAh cm^{-2} are only possible with other types of active materials like silicon on the anode side and high amounts of conductive additive.

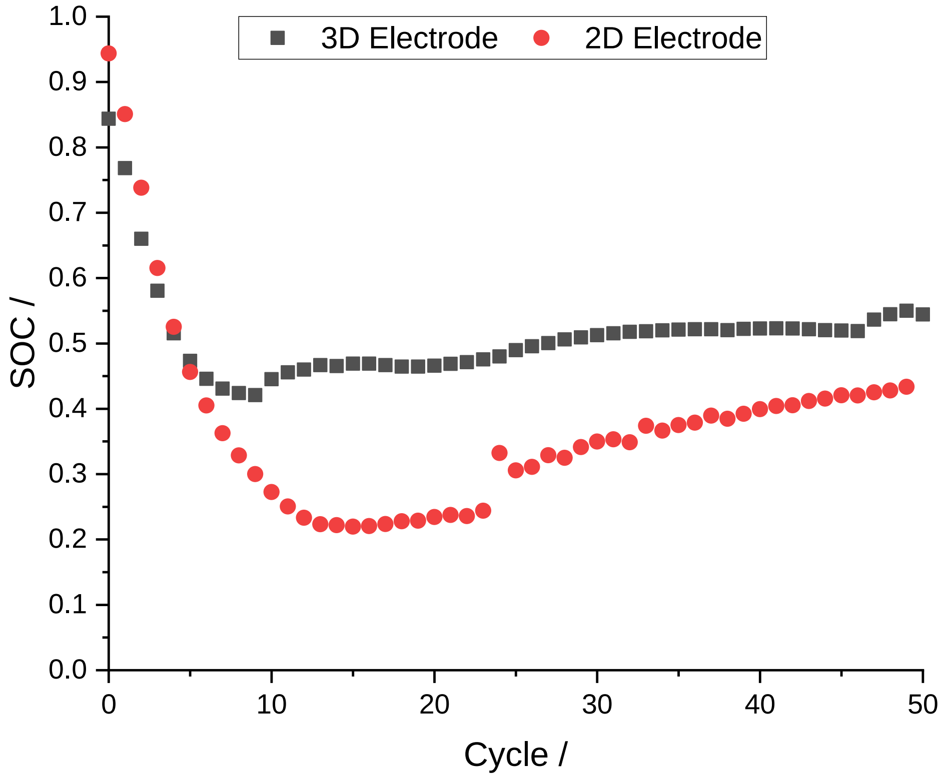

Figure 55: Cycling performance with 0.5 C of a 2D and 3D electrode with the same area capacity.

In conclusion, the fibers produced by melt spinning are an auspicious material to manufacture 3D current collector batteries based on micro metal fibers. They combine improvements for several unique aspects of batteries and are a potential candidate to overcome different challenges currently facing actual state-of-the-art batteries. [214] From their high failure resistance due to the fibrous and highly deformable current collector structure to their high power high energy performance, this system may be the next big step in battery development. As the current collector is an inactive component in the lithium-ion battery, it can be seen as drop-in technology that further improves all kinds of current developments on active components as the active material or electrolyte. Especially their performance with respect to lithium-ion diffusion and conductivity makes it a very promising solution to the challenges occurring in all solid-state batteries. [215] Furthermore, the system can also be transferred to aluminum networks that can be used as current collector on the cathode side. Several experiments described above were already performed for this system and showed similarly promising results. Hence, the production of batteries with a 3D current collector system on both the anode and cathode side is feasible. This can lead to an overall improvement of the electrical performance of the lithium-ion battery as well as an improved mechanical stability that opens the path to new applications as well as an increased sustainability of the batteries due to longer lifetimes.

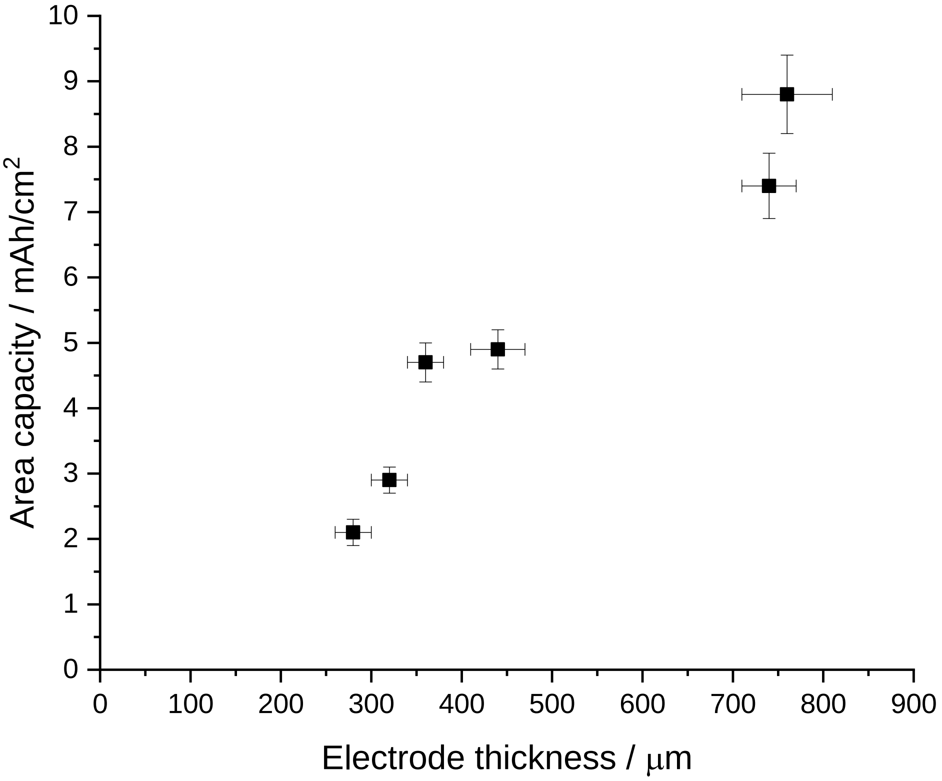

Figure 56: Area capacity for several 3D fiber electrode thicknesses.

5. Summary and Outlook

5.1. Summary

In the present work, the materials system of super-fast quenched microfibers is discussed in three parts. In the first part, the unique material properties are discussed and form the basis for all manufacturing routes, product properties, and applications discussed later. In the second part, different innovative manufacturing routes are introduced and discussed to form stable 3-dimensional fiber networks. In the last section, the application as lithium-ion battery current collector is presented and discussed with regard to their advantages over established systems.

The material class of super-fast quenched but crystalline materials is an intermediate system between amorphous metallic glasses and classic crystalline materials and combines the properties of both. Due to the super-fast quenching during the melt spinning process, a low degree of crystallization in the material occurs. During the production process the fibers are highly accelerated in the direction of the fibers' length. Simultaneous to this acceleration the fiber is solidified, so that the fibers show a strong orientation towards the fiber length. The smaller the fibers, the higher is the quenching rate and, therefore, the time for reaching a crystallographically preferred lattice position is shorter and the orientation is lower. By a controlled thermal treatment, the orientation of the fibers can be equalized towards a crystallographically more stable phase while at the same the degree of crystallinity can be increased depending on the temperature. During this thermal treatment, the materials move towards a crystallographically and thermodynamically more stable system.

The difference between the non-preferred state before the treatment and the more preferred state can be expressed as stored energy. For bulk metallic glasses, this stored energy is well known and can be measured as exothermal release while heating. It was possible to show that the bulk metallic glass as model system is also valid for the material system investigated here. After a thermal treatment above the crystallization temperature of amorphous fibers, the highest change in the degree of crystallization happens. This is directly visible as a drop in the specific heat capacity. For the crystalline CuSi fibers, a high exothermal release of the stored energy is also visible. Since the fibers are already crystalline, the stored energy could be measured as difference in the specific heat capacity of non-treated and annealed fibers. Combined with the results of the crystallographic properties of the fibers and the change in the degree of crystallization, the stored energy is higher for smaller fibers. The mechanical properties of the fibers were investigated for different fiber sizes, thermodynamic states, and degrees of crystallization. While for bulk metallic glasses only the degree of crystallization is influencing the mechanical properties, the intermediate material investigated here is also influenced by the size of the fibers. For the CuSi3 fibers, the degree of crystallization is increasing the elastic modulus within the fiber system. Similar to nanomaterials, the material is more elastic for smaller diameters.

Dry and wet routes are discussed for fiber laying. The dry method called carding is a modified process from the wool industry. With the help of carding a network of highly parallelized fibers can be achieved which can be used immediately or can act as an intermediate step for the wet route. Here, different materials were tested as assisting materials and successfully introduced to increase the homogeneity in networks with low area density. Pure polypropylene fibers showed the best results as assisting agent. The fibers could be removed without any residues during the protective gas sintering process in the next production step. For the wet approach dispersing was investigated. Here the fibers were cut from the carded network in a certain length and it was investigated how production parameters influence network homogeneity and later network properties. Here, a fiber length of 7 mm was found to be the best compromise between network stability and network homogeneity. For dispersing the fibers, water with polyvinyl alcohol as dispersing agent showed good results with respect to network homogeneity and was easy to remove completely by washing the network. The most promising approach was dispersing in paraffin oil. The networks showed a high homogeneity and the paraffin oil residues on the fibers could be evaporated during protective gas sintering in the next production step.

The fibers were sintered to stabilize the network. Here, the same basic principle of diffusion-driven processes could be demonstrated. Three unique routes, which can only be applied to these materials, were investigated. The fibers discussed here possess a non-round cross-section, which means that the surface is much larger than for round fibers. With a controlled thermal treatment, the fibers can be rounded by diffusion principles. The driving force here is the reduction of the surface towards a minimized Gibbs energy. Parameters for just rounding and combined rounding with sintering are presented in this work. A super-fast heating process is introduced for processes where a large surface is helpful. Super high heating rates in the range of several hundred kelvins per minute are required for this process. With this fast heating rate, the stored energy can be used as the process temperature and the sintering temperature can be decreased significantly. For this process, process times of less than one minute are required for a permanent connection of the fibers. Due to the reduced process time, the time is too short to round the fibers. For material systems like the metallic glass fibers, a sintering process with low temperatures is needed. The stored energy can also be used here to reduce the required energy. It could be shown that pressure combined with a temperature of just around 30-40 % T_m is enough to sinter the fibers. Here, the pressure activation energy relation was investigated. The higher the pressure, the higher the diffusion rate at the same temperature.

The sintered networks were tested for their mechanical properties and their electric conductivity. The longer, the higher the electric conductivity. A fiber length of 7-10 mm showed the best properties with respect to elastic modulus and tensile strength. Here, the connection points and network homogeneity are the impact parameters. While short fiber networks showed a homogeneous elongation, networks with longer fibers showed an inhomogeneous necking due to inhomogeneities in the network caused by the production process. The area density of the 7 mm fibers was variated and showed that more fibers and, therefore, more connection points in between the network significantly increases the elastic modulus and the tensile strength. The electric conductivity in the network is in the range of a bulk metal and the conductivity is still high after elongation by 50 %.

This good electric conductivity is one of the big improvements for the application of the 3D fiber networks as current collector for lithium-ion batteries. In contrast to a conventional foil-based electrode where only one side of the active material film is conducted with a metal substrate, in our case the whole active material bulk is conducted. This improves several battery properties. One is the overpotential in batteries, especially during high loading rates. Compared with other material which are used to improve the bulk conductivity, copper has a 10 times higher conductivity. Therefore, the overpotential could be removed nearly completely. The effect of overpotentials is not only more relevant for fast charging rates but also for thick electrodes. The larger the distance from the active material to the next current collector, the higher the potential gradient. Therefore, electrode thickness is strongly limited in the 2D case by the electric conductivity.

It was possible to show, that in our system lithium-ion diffusion is increased compared to the 2D system. Possible explanations for this are a smaller tortuosity and surface diffusion effects. The higher surface stress due to the non-round cross-section as well as the high defect concentration are helpful for surface diffusion. Apart from electric conductivity, lithium-ion diffusion is the second limiting factor for fast charging and thicker electrodes. The longer the diffusion path in the solid active material, the lower the fast charging possibilities. Therefore, a system with higher porosity in addition to surface diffusion and tortuosity is helpful. With higher porosity, the electrolyte is penetrating more into the active material bulk and, therefore, much faster diffusion in the electrolyte can be used. A higher porosity is not possible in the 2D system because it decreases the conductivity. This is especially relevant for all solid-state batteries.

Another impact factor for lithium-ion batteries is mechanical stability. In the 3D system, not only the adhesion effect of the binder helps to stabilize the active material. The 3-dimensional structure of the networks helps to keep the active material within the electrode. This is needed especially for active materials which are swelling while loading. The elastic structure of the fiber networks allows the active material to swell while the current collector is swelling at the same time. During kinking tests it could be shown that also with a much lower binder fraction in the active material, the mechanical stability is highly increased compared with 2D electrodes. This was also visible during tensile tests. After a 15 % elongation less than 1 wt.-% of the active material was released. After a 25 % elongation, the electric conductivity in the electrode is still high which shows a high failure safety. This strong mechanical stability makes the 3D fiber electrode highly usable for flexible batteries.

Based on the improved electric conductivity, lithium-ion diffusion, and mechanical properties, it could be shown that the system presented here is a good candidate for thick electrodes. With thick electrodes, the energy density can be improved highly due to less inactive components like separators or current collector foils. For our system with 10 µm fibers, the gravimetric energy density can be increased by around 23 % and the volumetric by around 33 %. An electrode with a thickness of over 800 µm could be manufactured, which is up to 10 times higher than 2D batteries. It could be shown that in the case of the 3D fiber electrodes not the active material film thickness is setting the loading properties but the pore size. Also ultra-thick electrodes showed a good cycle performance. With this system it is possible to combine the high power and high energy of 2D electrodes to obtain high-power high-energy 3D energy.

5.2. Outlook

The present work covers the complete system from the smallest part, a single fiber, the properties towards an intermediate product to the production result, a network, and finally its application as a lithium-ion battery anode. Further studies must be divided in the following steps:

Fibers

In this work, the basic properties of hyper quenched but still amorphous fibers is explained with the copper-silicon system as model system. However, a wide range of other materials and compositions also shows promise. While in this work, only fibers with a silicon content of 3 wt.-% and 4 wt.-% silicon were available, the systematic variation of fiber properties by a higher or lower amount of silicon could help to explain the influence of precipitations. The reported trend of mechanical properties as function of thermodynamics and crystallography towards smaller fibers can be extended towards fibers in the single-digit micrometer range or also in the nanometer range. In this range, the fibers could be also amorphous which would change all material properties significantly.

Beside the copper-silicon system, aluminum is an important material for lithium-ion battery cathodes. Therefore, aluminum or aluminum alloys are a highly recommended candidate for further investigations. There, not only parameter variations presented here can be investigated but also the influence of material density compared with copper and the influence of surface passivation is of interest as well.

In this work, amorphous design alloys were used as model systems to explain the processes inside the materials. For Vitrovac or other amorphous design alloys like $Fe_{40}Ni_{40}B_{20}$ it seems to be interesting to study the fiber size variations to observe the influence of crystallinity in more detail and with a wider variation range compared to crystalline materials

A modified melt spinning process could lead to much higher quenching rates and their influence could be investigated in more detail. In the present work only indicators showed the strong influence of the quenching rate on the properties. Here, it was not possible to investigate this influence without the possible influence of the fiber size. Same-sized fibers with different quenching rates could help to clarify the quenching rate influence.

Networks

The most obvious extension of the network parameters and sintering methods presented here is aluminum or the aluminum alloy system. Aluminum is a much softer, more elastic and lower meltable material and seems to be an interesting candidate to translate the methods presented here to a much more difficult other material. Especially, low-temperature pressure-assisted sintering could be a good method to overcome sintering problematics caused by the oxide surface passivation layer.

In general, it should be possible to translate the methods for rounding, sintering without fundamental change of the aspect ratio, and low-temperature pressure-assisted sintering to a wide range of materials.

Especially for amorphous materials, low-temperature pressure-assisted sintering seems to be a unique method for sintering without crystallization. In this work, only macroscopic experiments were performed to explain the process mechanisms. More precise results could be achieved for single fiber sintering. While for the crystalline fibers, the interface area is clearly visible due to the change in the crystallinity, this is not the case for crystalline fibers. Here, the interface could be investigated with its mechanical properties or with doped materials and, therefore, an atomic gradient. For amorphous materials transmission electron microscopy could be used to investigate the crystallographic structure and the assumed amorphous to crystalline phase transition in the interface area in more detail.

In this work, the influence of area density and fiber length was investigated. Another interesting parameter is the fiber size which could also influence the mechanical and electrical network properties. In addition, it would be worthwhile to study the influence of the fiber cross-section, i.e. round or non-round fibers.

Lithium-Ion Battery

In this work, 3D fiber network current collectors were introduced. Based on copper-silicon fibers, only the anode was investigated here. Using aluminum fibers the 3D fiber network current collector could also be introduced into the cathode. Simulations in the group showed that the benefit of the 3D current collector in the cathode is much higher than in the anode due to the lower electric conductivity of the active material in the cathode. These simulations also showed the influence of the size of the fibers and therefore the amount of fibers on a certain pore size. Therefore, fiber size is important for the potential gradient in the electrode, especially for fast charging electrodes. For all these and more simulative results, an experimental validation is still missing.

The results showed that the metal fiber network improves lithium-ion diffusivity through the anode. Here, systematic investigation on an atomistic scale is needed to explain this important property in detail. Additional electrochemical measurements like galvanostatic intermittent titration (GITT) or nuclear magnetic resonant and transmission electron microscopy (TEM) could help to determine diffusion parameters and the underlying mechanism.

Many of the electrode processing parameters like slurry viscosity and, thus, active material penetration in the network or the pore size have not been investigated completely. Here, a lot of processing work is still missing.

Further applications

Here, lithium-ion batteries are discussed as possible applications for the microfibers. However, many more surface-active processes could be improved by the 3D fiber networks. Possible candidates are electrolysis, catalysis or filtration. Here, the surface influence of fiber size variation and of the non-round cross-sections are relevant parameters. Not only the higher surface is promising but also the good mechanical properties compared to state-of-the art systems are unique.

While the surface is mainly relevant for most of the further applications discussed previously, also the amorphous character seems to be helpful to increase catalysis efficiency. Here, the low-temperature pressure-assisted sintering is a unique production route to form mechanically stable and, in a certain range, also thermally stable catalysts.

6. Appendix

6.1. Supplementary Figures

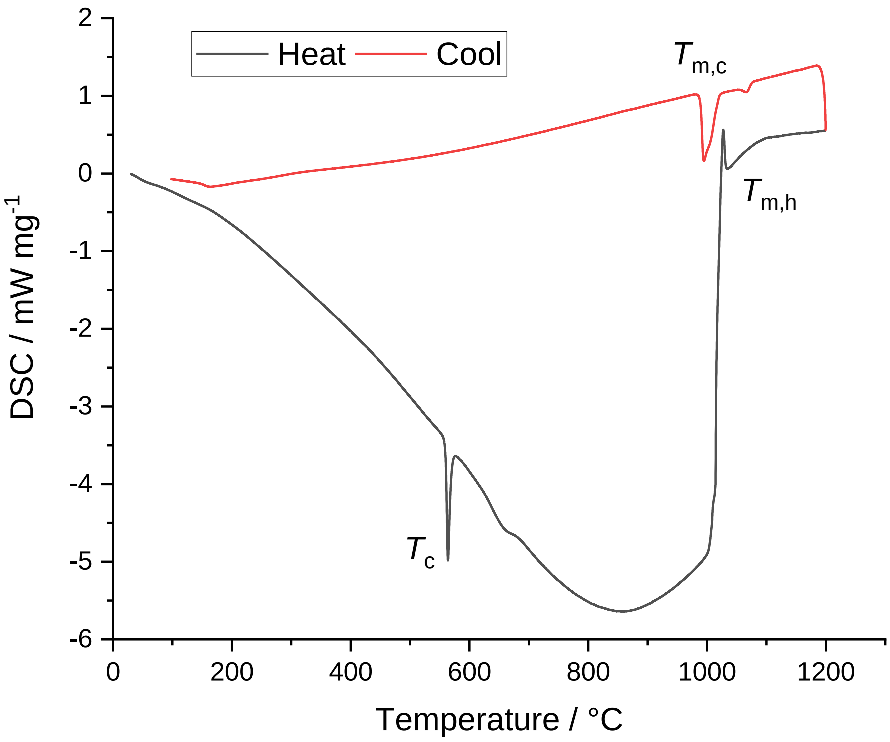

Figure A 1: DSC measurement results of Vitrovac: T_c = 565 °C; $T_{m,h}$ = 1030 °C; $T_{m,c}$ = 995 °C.

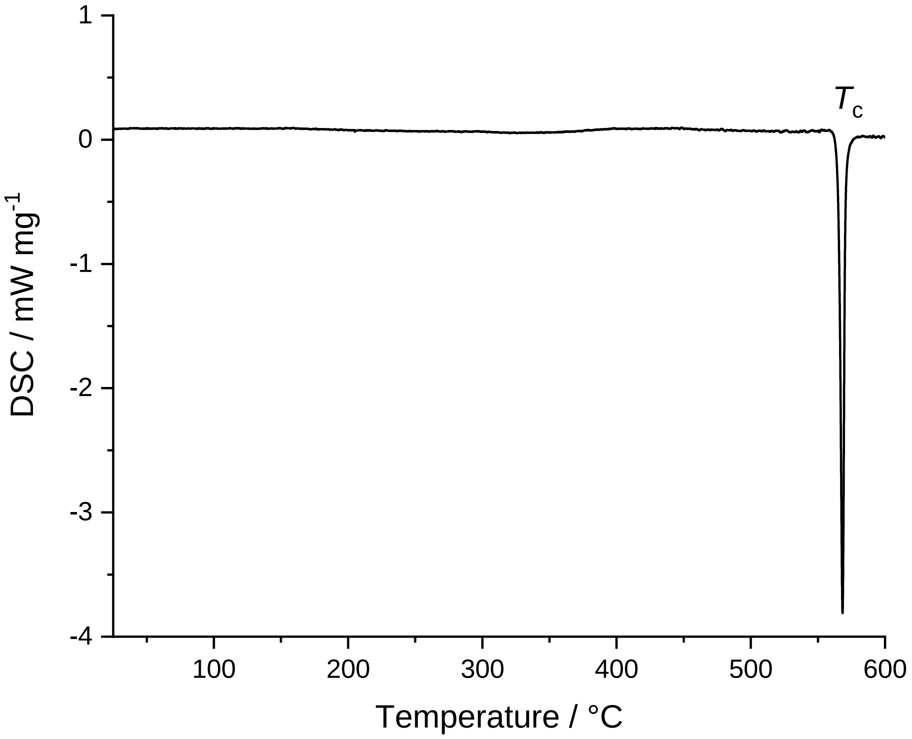

Figure A 2: DSC measurement results of Vitrovac: T_c = 568 °C.

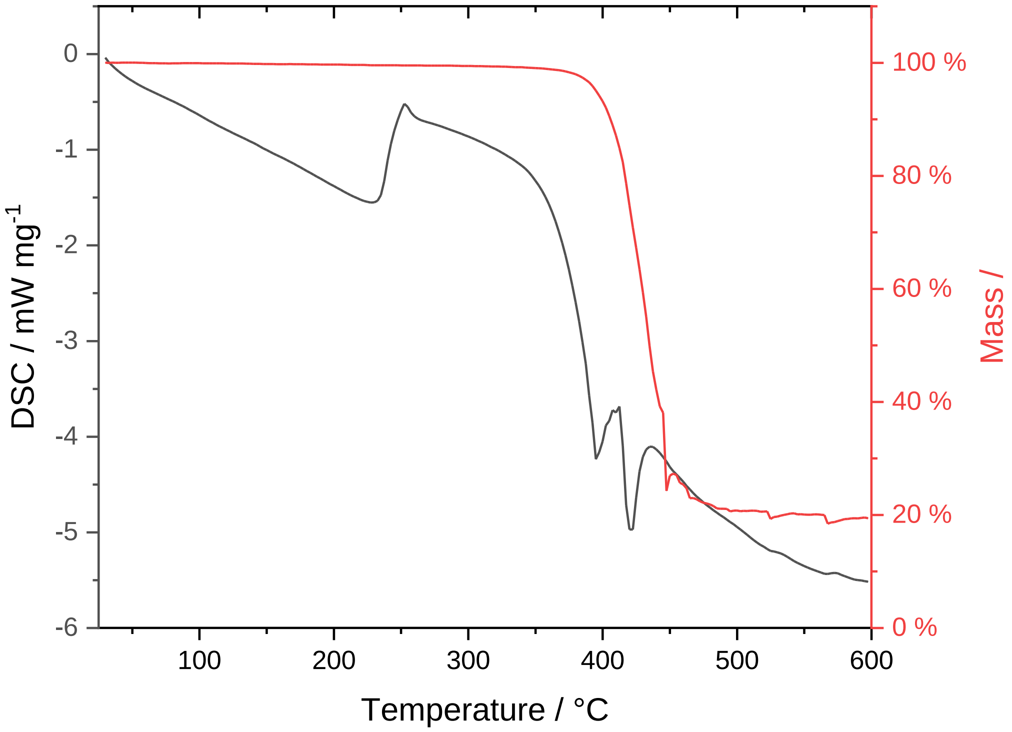

Figure A 3: STA measurements results of Polyethylene (Advansa, Hamm).

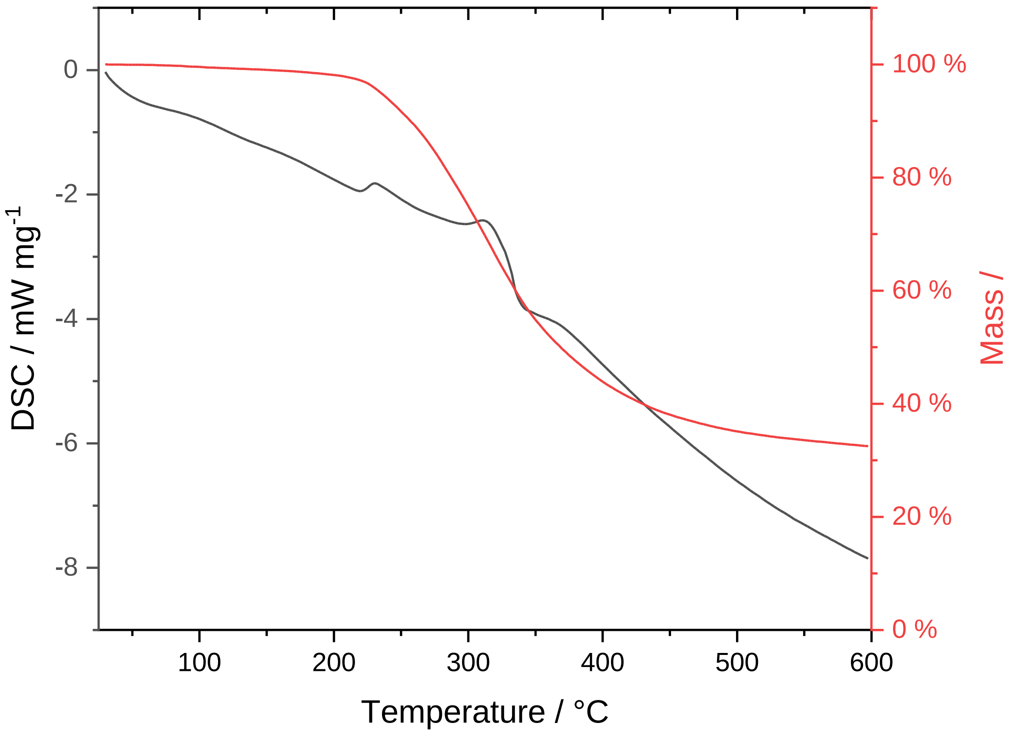

Figure A 4: STA measurement results of virgin wool (Wollknoll, Oberrot).

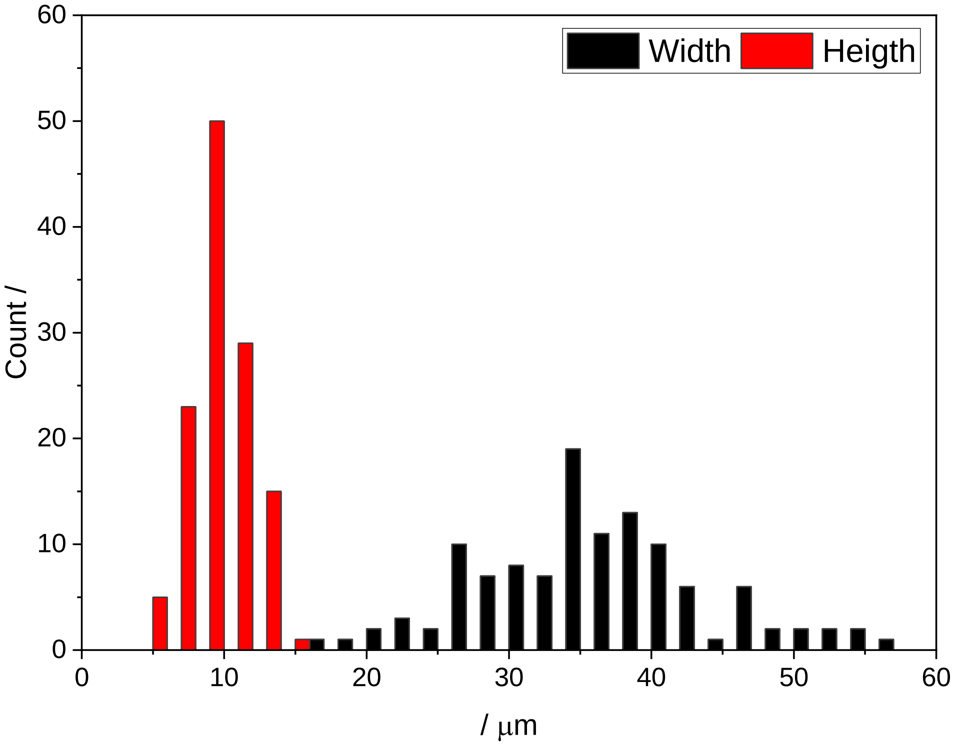

Figure A 5: Width and height of flat CuSi3 fibers.

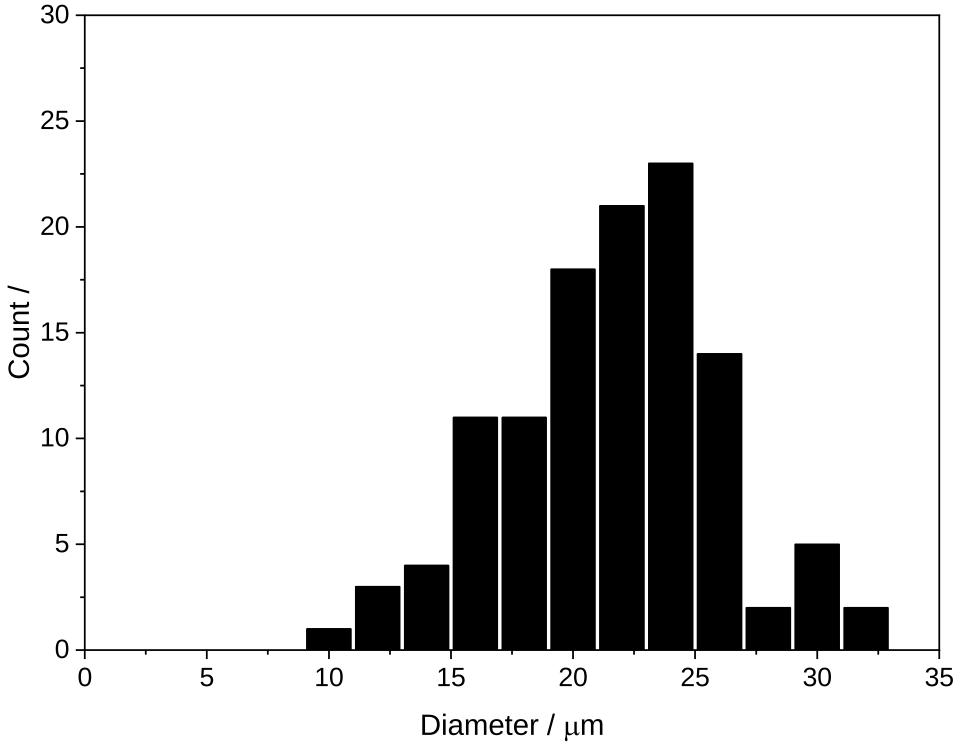

Figure A 6: Diameter of rounded CuSi3 fibers.

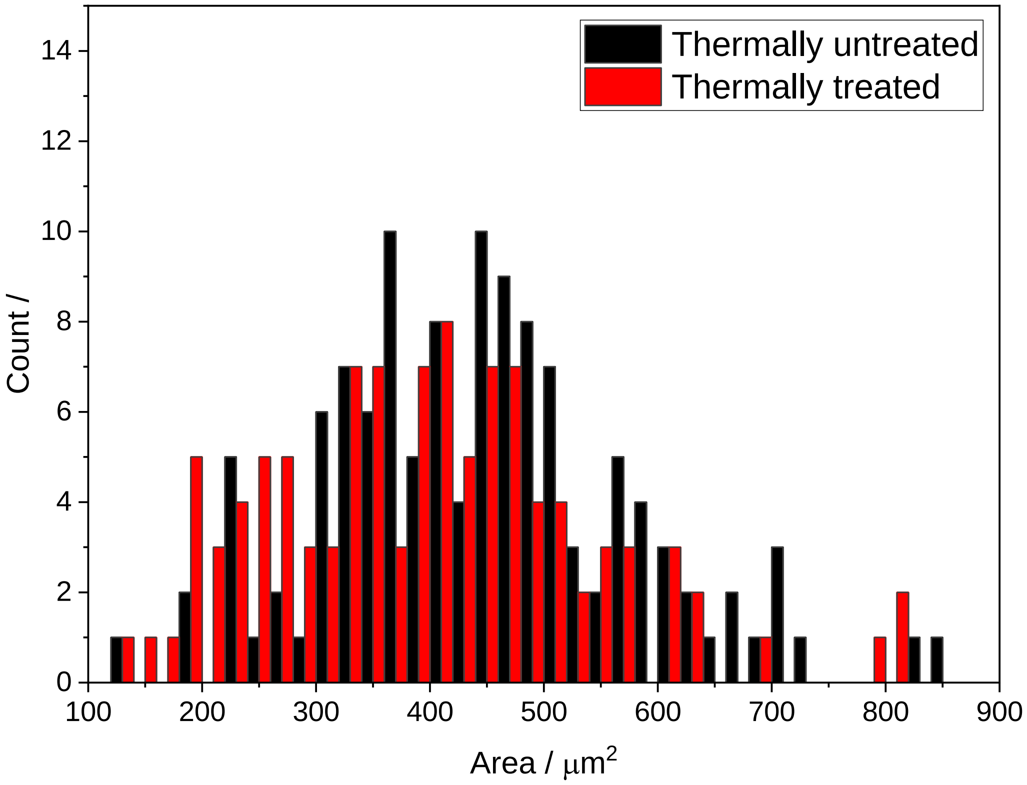

Figure A 7: Cross-section area flat and rounded CuSi3 fibers.

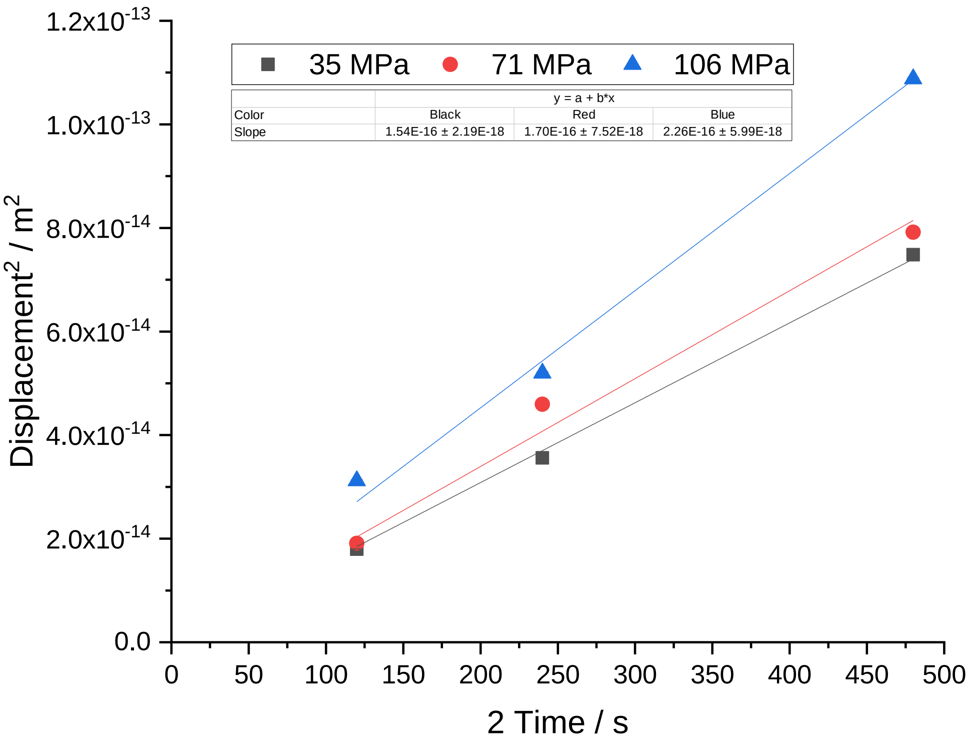

Figure A 8: Diffusion interface data for Vitrovac at 350 °C.

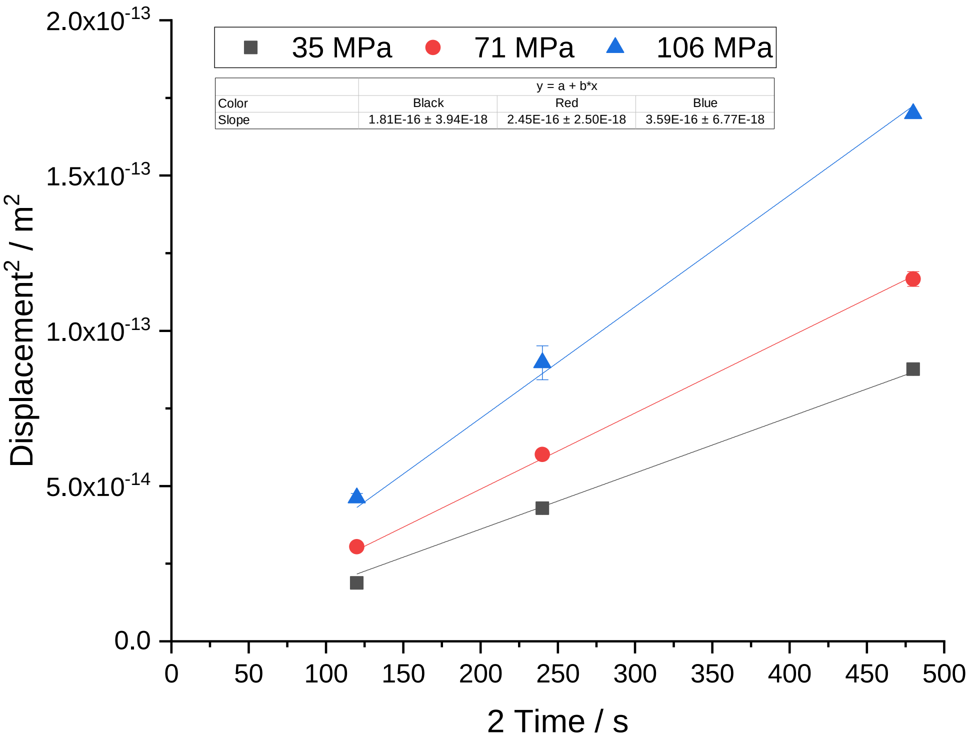

Figure A 9: Diffusion interface data for Vitrovac at 400 °C.

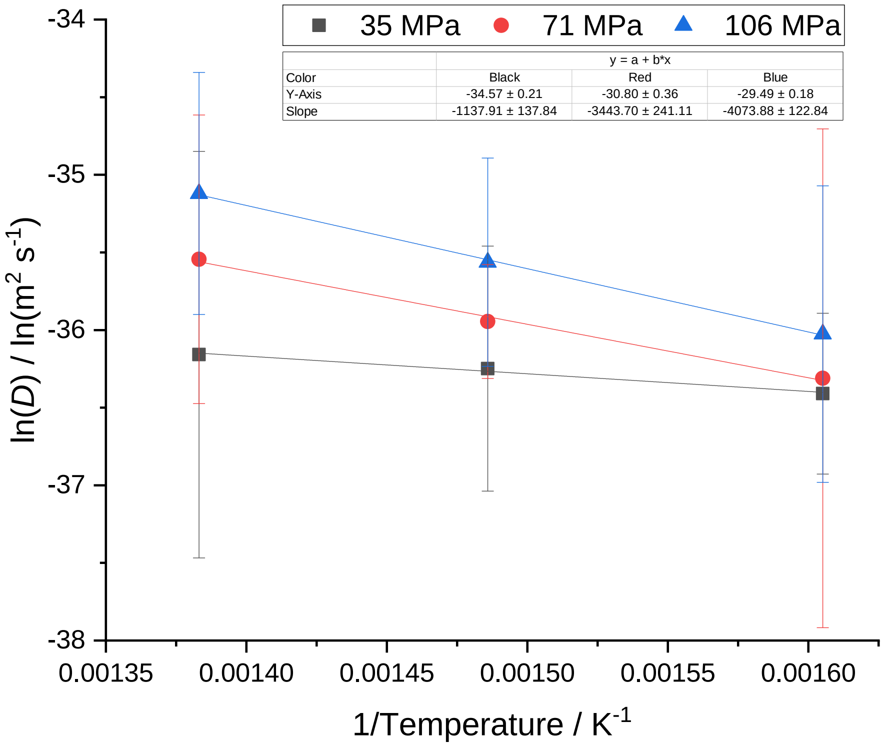

	y = a + b*x		
Color	Black	Red	Blue
Y-Axis	-34.57 ± 0.21	-30.80 ± 0.36	-29.49 ± 0.18
Slope	-1137.91 ± 137.84	-3443.70 ± 241.11	-4073.88 ± 122.84

Figure A 10: Arrhenius plot of the diffusion interface data for Vitrovac.

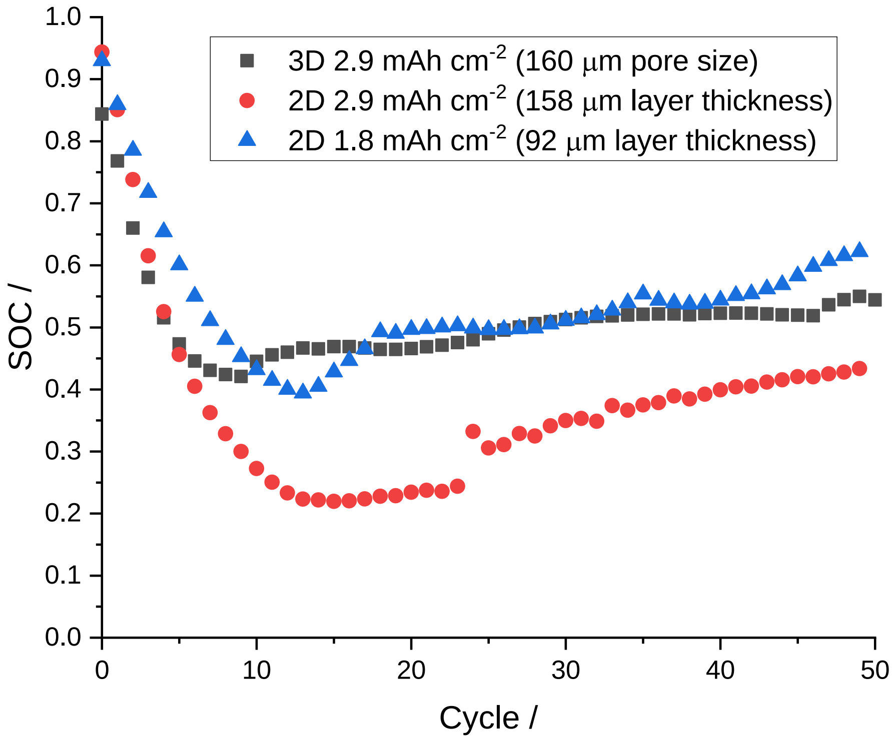

Figure A 11: Cycling performance with 0.5 C for a 3D electrode compared with 2D electrodes with either the same area capacity or comparable active material thickness (thickness vs. 0.5 times pore diameter).

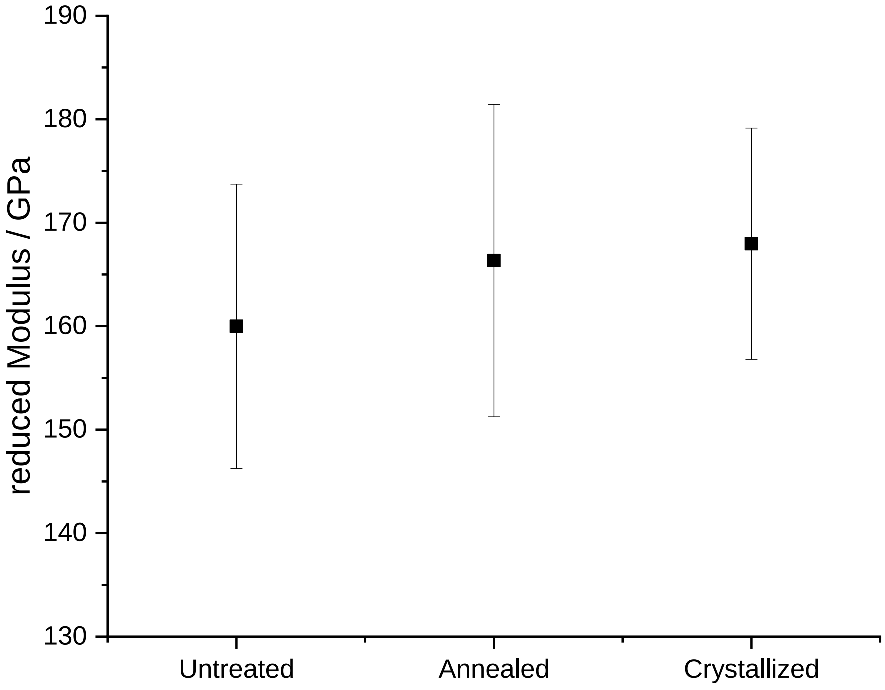

Figure A 12: Nanoindentation results for fibrous Vitrovac in different states.

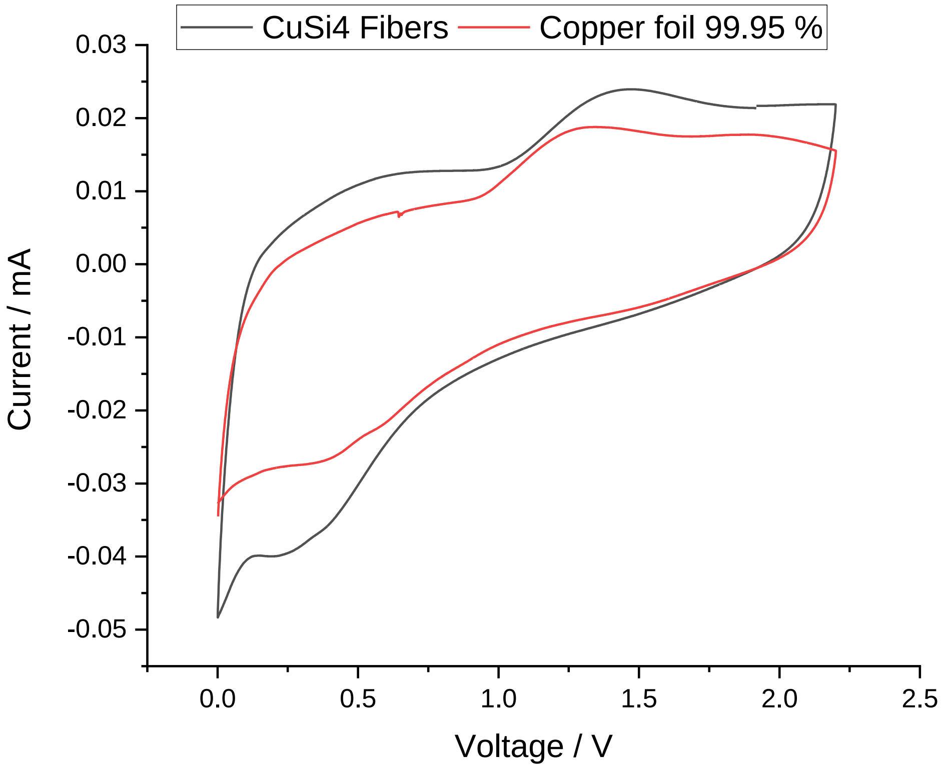

Figure A 13: Electrochemical stability of CuSi4 fibers vs. commercially available battery grade copper foil (MIT Corporation).

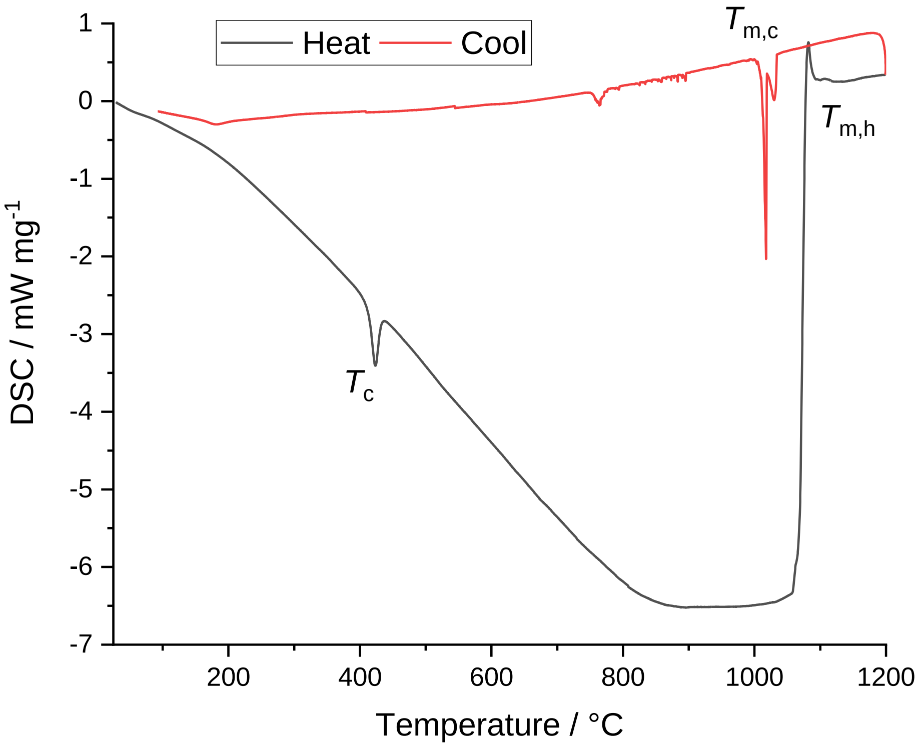

Figure A 14: DSC measurement results of $Fe_{40}Ni_{40}B_{20}$*:* $T_c = 423$ *°C;* $T_{m,h} = 1078$ *°C;* $T_{m,c} = 1018$ *°C.*

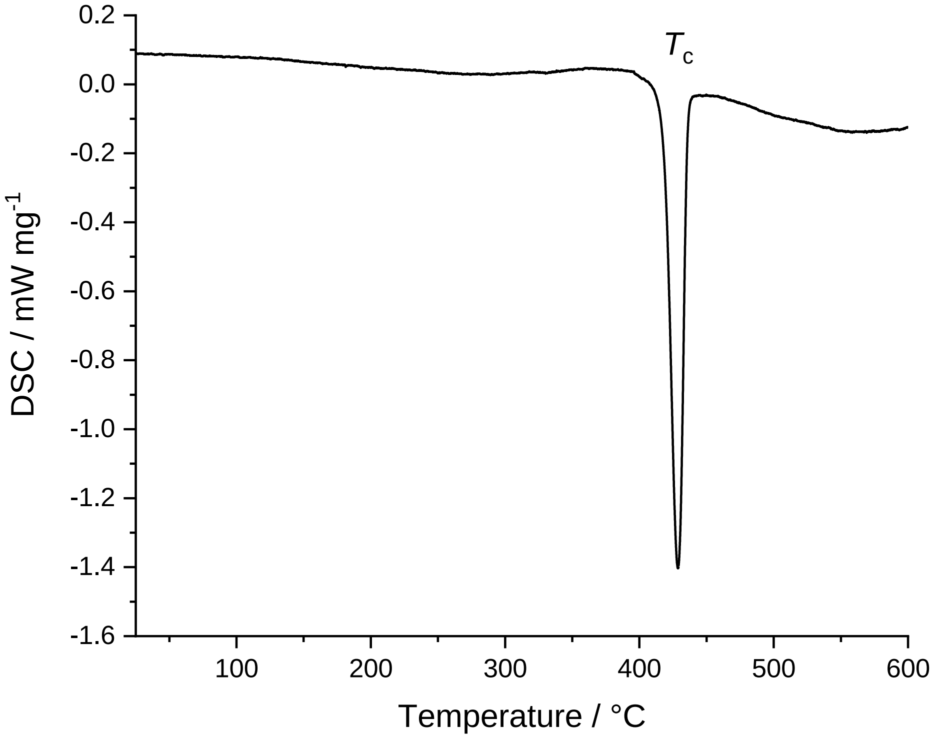

Figure A 15: : DSC measurement results of $Fe_{40}Ni_{40}B_{20}$*:* $T_c = 429$ *°C.*

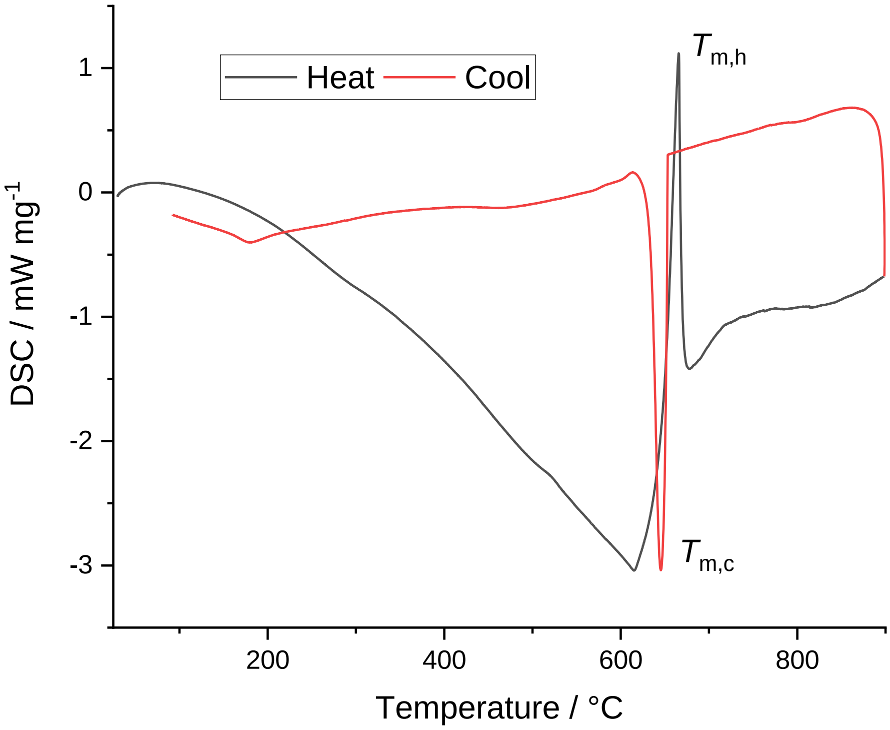

Figure A 16: DSC measurement results of AlSi1: $T_{m,h}$ *= 665 °C;* $T_{m,c}$ *= 646 °C*

6.2. Supplementary results

With the process investigated in section 4.2.2.1, non-round melt spinning AlSi1 fibers were rounded in a controlled manner. Here, a temperature of 630 °C seems to be the ideal rounding temperature. Figure A 17 shows a SEM image of controlled rounded AlSi1 fibers. These results and findings are also published in [176].

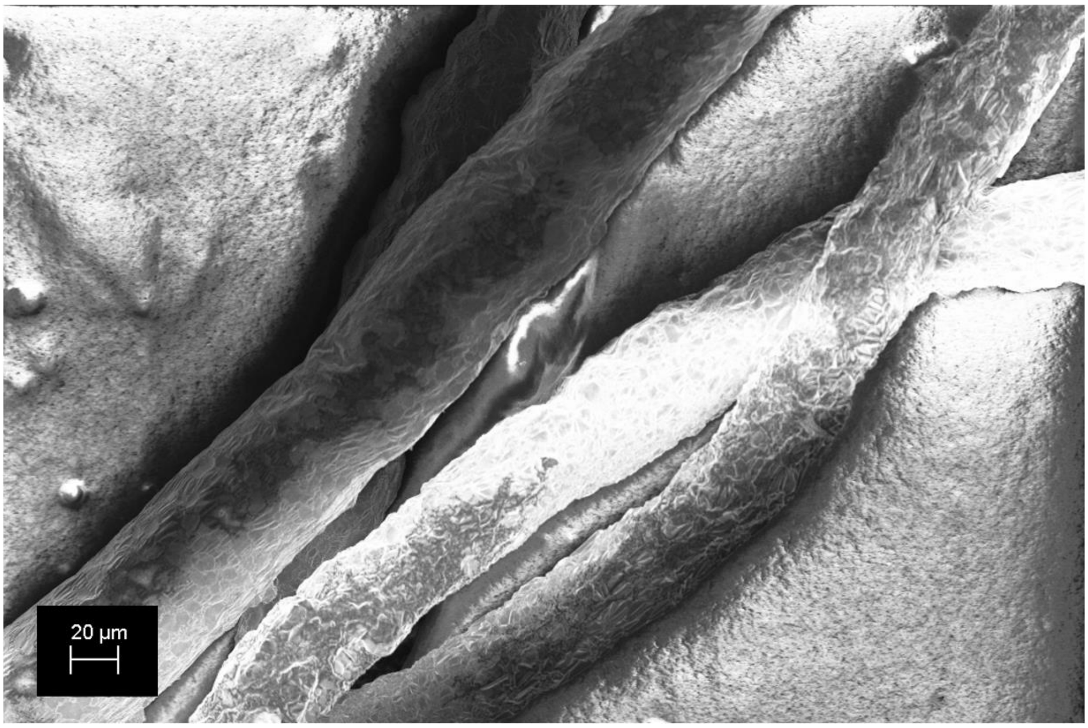

Figure A 17: Rounded AlSi1 fibers.

With the process investigated in section 4.2.2.2, non-round melt spinning AlSi1 fibers were sintered without a fundamental change of the aspect ratio. Untreated fibers with stored energy start to sinter at 630 °C while annealed fibers start at 640 °C but with a rounding of the fibers. Figure A 18 shows some of these sintered flat fibers. These results and findings are also published in [175].

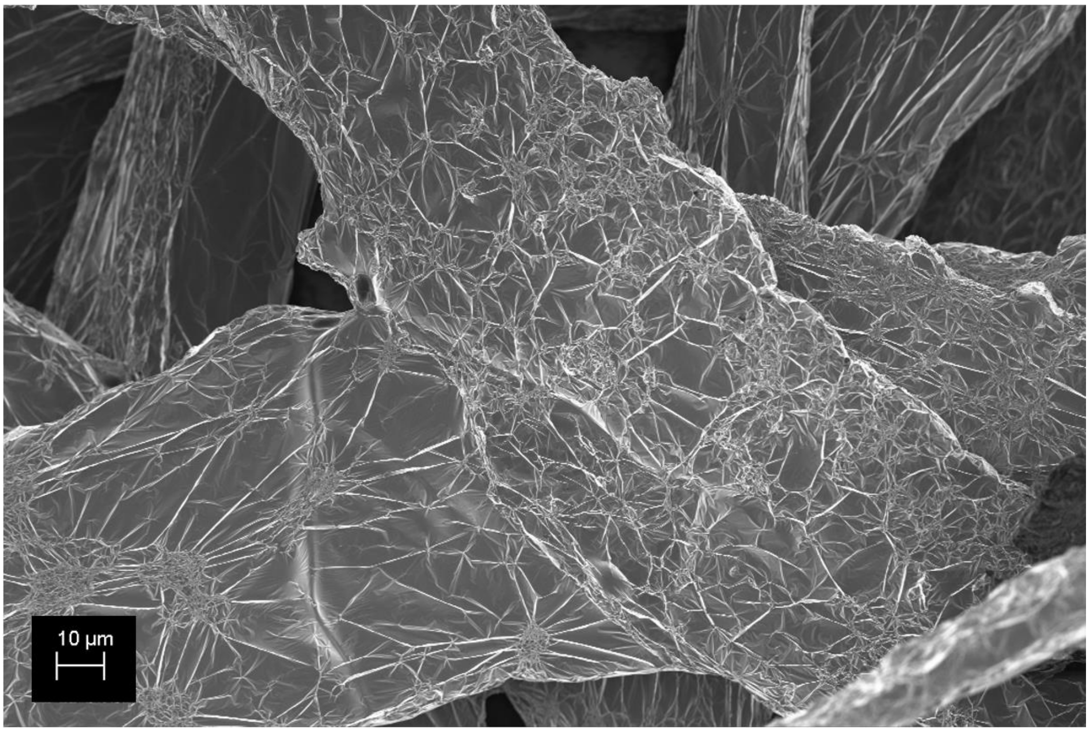

Figure A 18: Sintered AlSi1 fibers without fundamental change of the aspect ratio.

With the process investigated in section 4.2.2.3, other fibrous melt spinning materials were sintered. The experimental determined parameters are given in Table A 1. The presented parameters can be understood as minimum parameters for a permanent mechanically stable connection between the fibers. Parts of the results and findings are published in [178].

Table A 1: Pressure-assisted low-temperature sintering parameters for $Fe_{40}Ni_{40}B_{20}$, CuSi3, CuSi4 and AlSi1.

Material	Temperature / °C	Pressure / MPa	Time / s
$Fe_{40}Ni_{40}B_{20}$	350	35	60
CuSi3	300	35	60
CuSi4	300	35	60
AlSi1	150	18	60

6.3. List of Figures

6.4. List of Tables

6.5. List of Publications

6.5.1. Granted Patents

Joachim P. Spatz, **Maximilian Hackner**, Alexandre Micoulet, Timotheus H. Jahnke, Zaklina Burghard, Martin Möller: “*Network of metal fibers, method for producing a network of metal fibers, electrode and battery*”, EP3821482 (A1).

6.5.2. Patent Applications

Maximilian Hackner, Timotheus H. Jahnke, Joachim P. Spatz: “*Filter*”, EP20/208880.3.

Maximilian Hackner, Joachim P. Spatz: “*Thermal bonding of non-round fibers without fundamental change of the aspect ratio*”, PCT/EP2021/062435.

Maximilian Hackner, Timotheus H. Jahnke, Yuanzhen Wang, Joachim P. Spatz: “*Mono-Multi-valent Ion diffusion in batteries*”, PCT/EP2021/062443.

Joachim P. Spatz, **Maximilian Hackner**, Daniel C. Hotz: “*Dry coated 3D fiber electrodes*”, EP21/179716.2.

6.5.3. Scientific publications

Maximilian Hackner, Joachim P. Spatz, et. al.: "*Thermal, crystallographic and mechanic properties of micrometer sized copper-silicon alloy fibers and their thermally induced relaxation*", in preparation.

Maximilian Hackner*, Timotheus H. Jahnke*, Joachim P. Spatz, et. al.: "*Tailored high-surface-area metal fiber networks as high performance filters*", in preparation.

Maximilian Hackner*, Timotheus H. Jahnke*, Joachim P. Spatz, et. al.: "*3-dimensional micrometer sized metal fiber based current collectors towards ultra-thick lithium ion battery electrodes*", in preparation.

Maximilian Hackner*, Yuanzhen Wang*, Timotheus H. Jahnke*, J.P. Spatz, et. al.: „*Significantly increased lithium ion mobility in active material by ultra-fine metal fibers*", in preparation.

---

* These authors contributed equally to this work.

6.6. Permissions

	License Number	License Date
Figure 1	5078821402132	May 30, 2021
Figure 2	5130751355813	August 16, 2021
Figure 4	5078741068668	May 30, 2021
Figure 5	5070760048493	May 16, 2021
Figure 6	5070861358701	May 16, 2021
Figure 8	5075341462925	May 24, 2021
Figure 8	Special permisson by mail from Springer Nature	September 2, 2021
Figure 10	5075430360787	May 24, 2021

Figure 7: Reproduced under the Creative Commons Attribution 4.0 International License: https://creativecommons.org/licenses/by/4.0/

7. References

1. Klein, S.J. and S. Coffey, *Building a sustainable energy future, one community at a time.* Renewable and Sustainable Energy Reviews, 2016. **60**: p. 867-880.
2. Brown, M.A., et al., *Scenarios for a clean energy future.* Energy policy, 2001. **29**(14): p. 1179-1196.
3. Chu, S. and A. Majumdar, *Opportunities and challenges for a sustainable energy future.* nature, 2012. **488**(7411): p. 294-303.
4. Diekmann, J., et al., *Ecological recycling of lithium-ion batteries from electric vehicles with focus on mechanical processes.* Journal of the electrochemical society, 2016. **164**(1): p. A6184.
5. Wu, F., J. Maier, and Y. Yu, *Guidelines and trends for next-generation rechargeable lithium and lithium-ion batteries.* Chemical Society Reviews, 2020. **49**(5): p. 1569-1614.
6. Mller, T. *Lithium ion battery automotive applications and requirements*. in *Seventeenth Annual Battery Conference on Applications and Advances. Proceedings of Conference (Cat. No. 02TH8576)*. 2002. IEEE.
7. Yue, Y. and H. Liang, *3D Current Collectors for Lithium-Ion Batteries: A Topical Review.* Small Methods, 2018. **2**(8).
8. Mizushima, K., et al., *LixCoO2 (0<x<-1): A new cathode material for batteries of high energy density.* Materials Research Bulletin, 1980. **15**(6): p. 783-789.
9. Whittingham, M.S., *Chemistry of intercalation compounds: Metal guests in chalcogenide hosts.* Progress in Solid State Chemistry, 1978. **12**(1): p. 41-99.
10. Yoshino, A., K. Sanechika, and T. Nakajima, *Secondary battery*. 1985.
11. Korthauer, R., *Lithium-Ion Batteries: Basics and Applications*. 2018: Springer.
12. Yu, S.-H., et al., *Understanding conversion-type electrodes for lithium rechargeable batteries.* Accounts of chemical research, 2018. **51**(2): p. 273-281.
13. Wang, H., et al., *TEM Study of Electrochemical Cycling-Induced Damage and Disorder in LiCoO2 Cathodes for Rechargeable Lithium Batteries.* Journal of The Electrochemical Society, 1999. **146**(2): p. 473-480.
14. Daniel, C., et al., *Cathode materials review.* AIP Conference Proceedings, 2014. **1597**: p. 26-43.
15. Aurbach, D., et al., *Design of electrolyte solutions for Li and Li-ion batteries: a review.* Electrochimica Acta, 2004. **50**(2-3): p. 247-254.
16. Hayamizu, K., *Temperature Dependence of Self-Diffusion Coefficients of Ions and Solvents in Ethylene Carbonate, Propylene Carbonate, and Diethyl Carbonate Single Solutions and*

Ethylene Carbonate + Diethyl Carbonate Binary Solutions of LiPF6Studied by NMR. Journal of Chemical & Engineering Data, 2012. **57**(7): p. 2012-2017.

17. Zheng, F., et al., *Review on solid electrolytes for all-solid-state lithium-ion batteries.* Journal of Power Sources, 2018. **389**: p. 198-213.
18. Tarascon, J.-M. and M. Armand, *Issues and challenges facing rechargeable lithium batteries.* Materials for sustainable energy: a collection of peer-reviewed research and review articles from Nature Publishing Group, 2011: p. 171-179.
19. Lu, L.L., et al., *Free-Standing Copper Nanowire Network Current Collector for Improving Lithium Anode Performance.* Nano Lett, 2016. **16**(7): p. 4431-7.
20. Li, A., et al., *A Review on Lithium-Ion Battery Separators towards Enhanced Safety Performances and Modelling Approaches.* Molecules, 2021. **26**(2): p. 478.
21. Song, Y., et al., *From separator to membrane: Separators can function more in lithium ion batteries.* Electrochemistry Communications, 2021. **124**: p. 106948.
22. Su, F.-Y., et al., *Flexible and planar graphene conductive additives for lithium-ion batteries.* Journal of Materials Chemistry, 2010. **20**(43): p. 9644.
23. Landi, B.J., et al., *Carbon nanotubes for lithium ion batteries.* Energy & Environmental Science, 2009. **2**(6): p. 638.
24. Zhou, G., et al., *Nanowires for Electrochemical Energy Storage.* Chemical Reviews, 2019. **119**(20): p. 11042-11109.
25. Lu, L., D. Yongnian, and Y. Yaochun, *Effect of conductive additives on the performance of lithium-ion batteries.* Materials Review, 2007. **21**(8): p. 267-269.
26. De Las Casas, C. and W. Li, *A review of application of carbon nanotubes for lithium ion battery anode material.* Journal of Power Sources, 2012. **208**: p. 74-85.
27. Kuang, Y., et al., *Thick Electrode Batteries: Principles, Opportunities, and Challenges.* Advanced Energy Materials, 2019. **9**(33): p. 1901457.
28. García-Moreno, F., *Commercial Applications of Metal Foams: Their Properties and Production.* Materials, 2016. **9**(2): p. 85.
29. Ji, H., et al., *Ultrathin graphite foam: a three-dimensional conductive network for battery electrodes.* Nano letters, 2012. **12**(5): p. 2446-2451.
30. Saleh, M.S., et al., *3D printed hierarchically-porous microlattice electrode materials for exceptionally high specific capacity and areal capacity lithium ion batteries.* Additive Manufacturing, 2018. **23**: p. 70-78.
31. Timmermans, M.Y., et al., *Electrodeposition of Adherent Submicron to Micron Thick Manganese Dioxide Films with Optimized Current Collector Interface for 3D Li-Ion Electrodes.* Journal of The Electrochemical Society, 2017. **164**(14): p. D954.

32. Jin, S., et al., *Advanced 3D Current Collectors for Lithium-Based Batteries.* Advanced Materials, 2018. **30**(48): p. 1802014.

33. Sun, H., et al., *Hierarchical 3D electrodes for electrochemical energy storage.* Nature Reviews Materials, 2018. **4**(1): p. 45-60.

34. Banhart, J., *Metal foams: production and stability.* Advanced engineering materials, 2006. **8**(9): p. 781-794.

35. Bisht, A., B. Gangil, and V.K. Patel, *Selection of blowing agent for metal foam production: A review.* Journal of Metals, Materials and Minerals, 2020. **30**(1).

36. Kulshreshtha, A. and S. Dhakad, *Preparation of metal foam by different methods: A review.* Materials Today: Proceedings, 2020. **26**: p. 1784-1790.

37. Hannemann, C., et al. *The Challenge of Open Cellular Metal Foam Production*. in *Proceedings of the 11th International Conference on Porous Metals and Metallic Foams (MetFoam 2019)*. 2020. Springer Nature.

38. Xu, Y., et al., *Solution processable holey graphene oxide and its derived macrostructures for high-performance supercapacitors.* Nano letters, 2015. **15**(7): p. 4605-4610.

39. Jahnke, T., et al., *Highly Porous Free-Standing rGO/SnO2 Pseudocapacitive Cathodes for High-Rate and Long-Cycling Al-Ion Batteries.* Nanomaterials, 2020. **10**(10): p. 2024.

40. Luo, J., et al., *Three-dimensional graphene foam supported Fe3O4 lithium battery anodes with long cycle life and high rate capability.* Nano letters, 2013. **13**(12): p. 6136-6143.

41. Kim, C.H., E.J. Shin, and L.H. Shin, *Flexible secondary battery and method for manufacturing same* 2014.

42. Jenax Inc. *Jenax Inc. Products Batteries*. 2014 [cited 2021 16th August]; Available from: https://jenaxinc.com/products/batteries/.

43. Idowu, A., B. Boesl, and A. Agarwal, *3D graphene foam-reinforced polymer composites–A review.* Carbon, 2018. **135**: p. 52-71.

44. Wei, T.S., et al., *3D printing of customized Li-ion batteries with thick electrodes.* Advanced Materials, 2018. **30**(16): p. 1703027.

45. Tian, X., et al., *Emerging 3D-printed electrochemical energy storage devices: a critical review.* Advanced Energy Materials, 2017. **7**(17): p. 1700127.

46. Hu, Y., et al., *Free-standing graphene–carbon nanotube hybrid papers used as current collector and binder free anodes for lithium ion batteries.* Journal of power sources, 2013. **237**: p. 41-46.

47. Liebermann, H. and C. Graham, *Production of amorphous alloy ribbons and effects of apparatus parameters on ribbon dimensions.* IEEE Transactions on Magnetics, 1976. **12**(6): p. 921-923.

48. Spatz, J., M. Watari, and R. Mager, *Apparatus and method of manufacturing metallic or inorganic fibers having a thickness in the micron range by melt spinning* 2016.

49. Spatz, J., *Method of producing metal strands and apparatus for producing metal strands*. 2019.

50. Wieland Werke AG, *Material Analysis CuSi4*. 2019.

51. Sekels GmbH, *Broschüre Abschirmfolie VITROVAC 6025X*. 2019.

52. Berkovich, E., *Three faceted diamond pyramid for micro-hardness testing.* Industrial Diamond Review, 1951. **11**(127): p. 129.

53. Oliver, W.C. and G.M. Pharr, *Measurement of hardness and elastic modulus by instrumented indentation: Advances in understanding and refinements to methodology.* Journal of Materials Research, 2004. **19**(1): p. 3-20.

54. Oliver, W.C. and G.M. Pharr, *An improved technique for determining hardness and elastic modulus using load and displacement sensing indentation experiments.* Journal of Materials Research, 1992. **7**(6): p. 1564-1583.

55. Wang, H., L. Zhu, and B. Xu, *Principle and Methods of Nanoindentation Test*. 2018, Springer Singapore. p. 21-36.

56. Wang, H., L. Zhu, and B. Xu, *Theoretical Models for Measuring Residual Stress by Nanoindentation Method*. 2018, Springer Singapore. p. 37-67.

57. Fischer-Cripps, A.C., *Nanoindentation Testing*. 2011, Springer New York. p. 21-37.

58. Fischer-Cripps, A.C., *Analysis of Nanoindentation Test Data*. 2011, Springer New York. p. 39-75.

59. Gottstein, G., *Materialwissenschaft und Werkstofftechnik - Physikalische Grundlagen*. 2014: Springer.

60. Shen, T.D., et al., *On the elastic moduli of nanocrystalline Fe, Cu, Ni, and Cu–Ni alloys prepared by mechanical milling/alloying.* Journal of Materials Research, 1995. **10**(11): p. 2892-2896.

61. Anthony, J.W., *Handbook of mineralogy*. 1990: Mineral Data Pub.

62. Hall, E.O., *The Deformation and Ageing of Mild Steel: II Characteristics of the Lüders Deformation.* Proceedings of the Physical Society, 1951. **64**(9): p. 742-747.

63. Petch, N.J., *The Cleavage Strength of Polycrystals.* Journal of the Iron and Steel Institute, 1953. **174**: p. 25-28.

64. Chokshi, A.H., et al., *On the validity of the hall-petch relationship in nanocrystalline materials.* Scripta Metallurgica, 1989. **23**(10): p. 1679-1683.

65. Kumar, K.S., H. Van Swygenhoven, and S. Suresh, *Mechanical behavior of nanocrystalline metals and alloys11The Golden Jubilee Issue—Selected topics in Materials Science and Engineering: Past, Present and Future, edited by S. Suresh.* Acta Materialia, 2003. **51**(19): p. 5743-5774.

66. Carlton, C. and P. Ferreira, *What is behind the inverse Hall–Petch effect in nanocrystalline materials?* Acta Materialia, 2007. **55**(11): p. 3749-3756.

67. Cottrell, A.H., *Theory of brittle fracture in steel and similar metals.* Trans. Met. Soc. AIME, 1958. **212**.

68. Quintana, P., E. Amano, and R. Valenzuela, *Effects of crystallization on the magnetization dynamics of Vitrovac amorphous ribbons.* Materials Science and Engineering: A, 1994. **181-182**: p. 978-981.

69. Fagherazzi, G., et al., *XRD investigation of the crystallization process in Fe40Ni40B20 metallic glass.* Journal of Non-Crystalline Solids, 1992. **151**(1-2): p. 59-65.

70. Zhu, F., et al., *Spatial heterogeneity as the structure feature for structure-property relationship of metallic glasses.* Nat Commun, 2018. **9**(1): p. 3965.

71. Qiao, J.C. and J.M. Pelletier, *Enthalpy relaxation in Cu46Zr45Al7Y2 and Zr55Cu30Ni5Al10 bulk metallic glasses by differential scanning calorimetry (DSC).* Intermetallics, 2011. **19**(1): p. 9-18.

72. Qiao, J.C. and J.M. Pelletier, *Dynamic Mechanical Relaxation in Bulk Metallic Glasses: A Review.* Journal of Materials Science & Technology, 2014. **30**(6): p. 523-545.

73. Qiao, J.C., et al., *Structural heterogeneities and mechanical behavior of amorphous alloys.* Progress in Materials Science, 2019. **104**: p. 250-329.

74. Gallino, I., M.B. Shah, and R. Busch, *Enthalpy relaxation and its relation to the thermodynamics and crystallization of the Zr58.5Cu15.6Ni12.8Al10.3Nb2.8 bulk metallic glass-forming alloy.* Acta Materialia, 2007. **55**(4): p. 1367-1376.

75. Callen, H., *Thermodynamics and an Introduction to Thermostatistics*. 2 ed. 1985: Wiley.

76. Claudy, P., M. Siniti, and J. El Hajri, *Thermodynamic Study of the Glass Relaxation Phenomena. DSC study of annealing of maltitol glass.* Journal of Thermal Analysis and Calorimetry, 2002. **68**(1): p. 251-264.

77. Chen, H., A. Inoue, and T. Masumoto, *Two-stage enthalpy relaxation behaviour of (Fe 0.5 Ni 0.5) 83 P 17 and (Fe 0.5 Ni 0.5) 83 B 17 amorphous alloys upon annealing.* Journal of materials science, 1985. **20**(7): p. 2417-2438.

78. Šesták, J., P. Hubík, and J.J. Mareš, *Thermal Physics and Thermal Analysis*. Hot Topics in Thermal Analysis and Calorimetry. 2017: Springer.

79. Mittemeijer, E.J., *Analysis of the kinetics of phase transformations.* Journal of Materials Science, 1992. **27**(15): p. 3977-3987.

80. Mittemeijer, E.J., *Fundamentals of Materials Science*. 2011: Springer.

81. Mittemeijer, E.J., *Diffraction Analysis of the Microstructure of Materials*. 2004: Springer.

82. Kaufman, L., *Coupled phase diagrams and thermochemical data for transition metal binary systems-VI.* Calphad, 1979. **3**(1): p. 45-76.

83. *Cu-Si Binary Phase Diagram 0-100 at.% Si: Datasheet from "PAULING FILE Multinaries Edition – 2012" in SpringerMaterials*, P. Villars and H. Okamoto, Editors., Springer-Verlag Berlin Heidelberg & Material Phases Data System (MPDS), Switzerland & National Institute for Materials Science (NIMS), Japan.
84. Bragg, W.H. and W.L. Bragg, *The reflection of X-rays by crystals.* Proceedings of the Royal Society of London. Series A, Containing Papers of a Mathematical and Physical Character, 1913. **88**(605): p. 428-438.
85. Spieß, L., et al., *Moderne Rötgenbeugung*. 2019: Springer.
86. Fick, A., *Ueber Diffusion.* Annalen der Physik und Chemie, 1855. **170**(1): p. 59-86.
87. Matano, C., *On the Relation between Diffusion-Coefficients and Concentrations of Solid Metals.* Japanese Journal of Physics, 1933. **8**: p. 109-113.
88. Balogh, Z. and G. Schmitz, *5 - Diffusion in Metals and Alloys*, in *Physical Metallurgy*, D. Lauglin and K. Hono, Editors. 2014, Elsevier.
89. Arrhenius, S., *Über die Reaktionsgeschwindigkeit bei der Inversion von Rohrzucker durch Säuren.* Zeitschrift für Physikalische Chemie, 1889. **4U**(1): p. 226-248.
90. Exner, H.E. and E. Arzt, *Sintering Processes*. 1990, Springer Netherlands. p. 157-184.
91. Vladikova, D., *Impedance of Lithium Ion Batteries — Basic Models and Differential Analysis*. 2000, Springer Netherlands. p. 593-596.
92. Westerhoff, U., et al., *Analysis of Lithium-Ion Battery Models Based on Electrochemical Impedance Spectroscopy.* Energy Technology, 2016. **4**(12): p. 1620-1630.
93. Chang, B.-Y. and S.-M. Park, *Electrochemical impedance spectroscopy.* Annual Review of Analytical Chemistry, 2010. **3**: p. 207-229.
94. Wang, S., et al., *Electrochemical impedance spectroscopy.* Nature Reviews Methods Primers, 2021. **1**(1).
95. Gulyaev, A. and E. Trusova, *Regularities of changes in the properties of solid solutions.* Zhurnal Tekhnicheskoi Fiziki, 1950. **20**: p. 66-78.
96. Olesinski, R.W. and G.J. Abbaschian, *The Cu−Si (Copper-Silicon) system.* Bulletin of Alloy Phase Diagrams, 1986. **7**(2): p. 170-178.
97. Yan, X. and Y.A. Chang, *A thermodynamic analysis of the Cu–Si system.* Journal of Alloys and Compounds, 2000. **308**(1-2): p. 221-229.
98. Lyutyi, P.Y., Y.O. Tokaichuk, and A. Fedorchuk, *Ternary Cr–Ga–Si system at 870 K.* Materials Science, 2011. **46**(4): p. 486-492.
99. Wang, J.Y., Z.M. Wang, and E.J. Mittemeijer, *Mechanism of aluminum-induced layer exchange upon low-temperature annealing of amorphous Si/polycrystalline Al bilayers.* Journal of Applied Physics, 2007. **102**(11).

100. Solberg, J.K., *The crystal structure of η-Cu3Si precipitates in silicon.* Acta Crystallographica Section A: Crystal Physics, Diffraction, Theoretical and General Crystallography, 1978. **34**(5): p. 684-698.

101. Kruzic, J.J., *Bulk metallic glasses as structural materials: a review.* Advanced Engineering Materials, 2016. **18**(8): p. 1308-1331.

102. Shkvarina, E.G., et al., *Thermal stability of the layered modification of Cu0.5ZrTe2 in the temperature range 25–900 °C.* Acta Crystallographica Section C Structural Chemistry, 2018. **74**(9): p. 1020-1025.

103. Haasen, P., *How are new orientations generated during primary recrystallization?* Metallurgical Transactions B, 1993. **24**(2): p. 225-239.

104. Katayama, K., K. Nakamura, and T. Amano, *Structural formation during melt spinning process.* Kolloid-Zeitschrift und Zeitschrift für Polymere, 1968. **226**(2): p. 125-134.

105. White, J.L. and M. Cakmak, *Orientation development and crystallization in melt spinning of fibers.* Advances in Polymer Technology: Journal of the Polymer Processing Institute, 1986. **6**(3): p. 295-337.

106. Fan, G., et al., *Oriented growth during recrystallization revisited in three dimensions.* Scripta Materialia, 2014. **72**: p. 9-12.

107. Stanford, N., D. Dunne, and M. Ferry, *Effect of orientation stability on recrystallization textures of deformed aluminium single crystals.* Materials Science and Engineering: A, 2003. **348**(1-2): p. 154-162.

108. Miura, H., et al. *Nucleation of dynamic recrystallization at the grain boundaries of copper bicrystals*. in *Materials Science Forum*. 2007. Trans Tech Publ.

109. Donthu, S.K., et al., *Activation energy determination for recrystallization in electroplated-copper films using differential scanning calorimetry.* Journal of electronic materials, 2003. **32**(6): p. 531-534.

110. Qi, Y., et al., *Molecular-dynamics simulations of glass formation and crystallization in binary liquid metals: Cu-Ag and Cu-Ni.* Physical review B, 1999. **59**(5): p. 3527.

111. Battezzati, L., et al., *A DSC study of structural relaxation in metallic glasses prepared with different quenching rates.* Journal of Non-Crystalline Solids, 1984. **61-62**: p. 877-882.

112. Zhong, L., et al., *Formation of monatomic metallic glasses through ultrafast liquid quenching.* Nature, 2014. **512**(7513): p. 177-180.

113. Benchabane, G., et al., *Recrystallization of pure copper investigated by calorimetry and microhardness.* Materials Characterization, 2008. **59**(10): p. 1425-1428.

114. Parker, W., et al., *Flash method of determining thermal diffusivity, heat capacity, and thermal conductivity.* Journal of applied physics, 1961. **32**(9): p. 1679-1684.

115. Liu, C., et al., *The cooling rate dependence of crystallization for liquid copper: A molecular dynamics study.* The Journal of Chemical Physics, 2001. **114**(17): p. 7506-7512.

116. Humphreys, F.J. and M. Hatherly, *Recrystallization and related annealing phenomena*. 2012: Elsevier.

117. Ackland, K., et al., *Ultra-soft magnetic Co-Fe-B-Si-Nb amorphous alloys for high frequency power applications.* AIP Advances, 2018. **8**(5): p. 056129.

118. Balasubramanian, G., A. Tiwari, and C. Srivastava, *Applicability of FMR for crystallization studies in metallic glasses.* Journal of materials science, 1990. **25**(3): p. 1636-1639.

119. Bergmann, L., C. Schaefer, and S. Blügel, *Lehrbuch der Experimentalphysik 6. Festkörper*. Vol. 6. 2005: Walter de Gruyter.

120. Ungar, T., *Microstructural parameters from X-ray diffraction peak broadening.* Scripta Materialia, 2004. **51**(8): p. 777-781.

121. Scherrer, P., *Bestimmung der inneren Struktur und der Größe von Kolloidteilchen mittels Röntgenstrahlen*, in *Kolloidchemie Ein Lehrbuch*. 1912, Springer. p. 387-409.

122. Yazdani, A., et al., *A method to quantify crystallinity in amorphous metal alloys: A differential scanning calorimetry study.* PLOS ONE, 2020. **15**(6): p. e0234774.

123. Schawe, J.E.K. and J.F. Löffler, *Existence of multiple critical cooling rates which generate different types of monolithic metallic glass.* Nature Communications, 2019. **10**(1).

124. Imran, M.M., et al., *Glass transition phenomena, crystallization kinetics and enthalpy released in binary Se100–xInx (x= 2, 4 and 10) semiconducting glasses.* physica status solidi (a), 2000. **181**(2): p. 357-368.

125. Chrissafis, K., et al., *Detailed study of the crystallization behaviour of the metallic glass Fe75Si9B16.* Journal of alloys and compounds, 2005. **386**(1-2): p. 165-173.

126. Tan, J., et al., *Study of mechanical property and crystallization of a ZrCoAl bulk metallic glass.* Intermetallics, 2011. **19**(4): p. 567-571.

127. Pogatscher, S., et al., *Monotropic polymorphism in a glass-forming metallic alloy.* Journal of Physics: Condensed Matter, 2018. **30**(23): p. 234002.

128. Abu-Sehly, A.A., S.N. Alamri, and A.A. Joraid, *Measurements of DSC isothermal crystallization kinetics in amorphous selenium bulk samples.* Journal of Alloys and Compounds, 2009. **476**(1-2): p. 348-351.

129. Legg, B.A., J. Schroers, and R. Busch, *Thermodynamics, kinetics, and crystallization of Pt57. 3Cu14. 6Ni5. 3P22. 8 bulk metallic glass.* Acta materialia, 2007. **55**(3): p. 1109-1116.

130. Zhang, Y., et al., *Formation and properties of Zr48Nb8Cu14Ni12Be18 bulk metallic glass.* Acta materialia, 2003. **51**(7): p. 1971-1979.

131. Buttino, G., A. Cecchetti, and M. Poppi, *Temperature dependence of structural and magnetic relaxation in amorphous and nanocrystalline Co-based alloys.* Journal of Magnetism and Magnetic Materials, 2002. **241**(2-3): p. 183-189.

132. Kissinger, H.E., *Reaction Kinetics in Differential Thermal Analysis.* Analytical Chemistry, 1957. **29**(11): p. 1702-1706.

133. Boswell, P.G., *On the calculation of activation energies using a modified Kissinger method.* Journal of Thermal Analysis, 1980. **18**: p. 353-358.

134. Ozawa, T., *Estimation of activation energy by isoconversion methods.* Journal of Materials Science, 1992. **203**: p. 159-165.

135. Schawe, J.E.K., S. Pogatscher, and J.F. Löffler, *Thermodynamics of polymorphism in a bulk metallic glass: Heat capacity measurements by fast differential scanning calorimetry.* Thermochimica Acta, 2020. **685**.

136. Wang, B.-X., L.-P. Zhou, and X.-F. Peng, *Surface and size effects on the specific heat capacity of nanoparticles.* International journal of thermophysics, 2006. **27**(1): p. 139-151.

137. Debye, P., *Zur theorie der spezifischen wärmen.* Annalen der Physik, 1912. **344**(14): p. 789-839.

138. De Wolf, I., *Micro-Raman spectroscopy to study local mechanical stress in silicon integrated circuits.* Semiconductor science and technology, 1996. **11**(2): p. 139.

139. Sohrabi, N., et al., *Critical crystallization properties of an industrial-grade Zr-based metallic glass used in additive manufacturing.* Scripta Materialia, 2021. **199**: p. 113861.

140. Schawe, J.E. and J.F. Löffler, *Existence of multiple critical cooling rates which generate different types of monolithic metallic glass.* Nature communications, 2019. **10**(1): p. 1-10.

141. Schawe, J., *Modulated temperature DSC measurements: the influence of the experimental conditions.* Thermochimica acta, 1996. **271**: p. 127-140.

142. Schawe, J.E., *Influence of processing conditions on polymer crystallization measured by fast scanning DSC.* Journal of Thermal Analysis and Calorimetry, 2014. **116**(3): p. 1165-1173.

143. Liu, Y., et al., *Cooling-rate induced softening in a Zr 50 Cu 50 bulk metallic glass.* Applied physics letters, 2007. **90**(7): p. 071909.

144. Yokoyama, Y., et al., *Study of the structural relaxation-induced embrittlement of hypoeutectic Zr–Cu–Al ternary bulk glassy alloys.* Acta Materialia, 2008. **56**(20): p. 6097-6108.

145. Deng, D. and A.S. Argon, *Structural Relaxation and Embrittlement of* $Cu_{59}Zr_{41}$ *and* $Fe_{80}B_{20}$ *Glasses.* Acta Metallurgica, 1986. **34**(10): p. 2011-2023.

146. Wu, T.W. and F. Spaepen, *Small angle X-ray scattering from an embrittling metallic glass.* Acta Metallurgica, 1985. **33**(12): p. 2185-2190.

147. Saida, J., R. Yamada, and M. Wakeda, *Recovery of less relaxed state in Zr-Al-Ni-Cu bulk metallic glass annealed above glass transition temperature.* Applied Physics Letters, 2013. **103**(22): p. 221910.

148. Cardarelli, F., *Materials Handbook*. 2018: Springer.

149. Cuenot, S., et al., *Surface tension effect on the mechanical properties of nanomaterials measured by atomic force microscopy.* Physical Review B, 2004. **69**(16): p. 165410.

150. Wang, Z.-Q., Y.-P. Zhao, and Z.-P. Huang, *The effects of surface tension on the elastic properties of nano structures.* International journal of engineering science, 2010. **48**(2): p. 140-150.

151. Yu, X. and Z. Zhan, *The effects of the size of nanocrystalline materials on their thermodynamic and mechanical properties.* Nanoscale research letters, 2014. **9**(1): p. 1-6.

152. Kulachenko, A., et al., *Elastic properties of cellulose nanopaper.* Cellulose, 2012. **19**(3): p. 793-807.

153. Hearle, J., *The fine structure of fibers and crystalline polymers. III. Interpretation of the mechanical properties of fibers.* Journal of applied polymer science, 1963. **7**(4): p. 1207-1223.

154. Hintsala, E.D., U. Hangen, and D.D. Stauffer, *High-throughput nanoindentation for statistical and spatial property determination.* Jom, 2018. **70**(4): p. 494-503.

155. Wang, Y., et al., *Orientation dependence of nanoindentation pile-up patterns and of nanoindentation microtextures in copper single crystals.* Acta materialia, 2004. **52**(8): p. 2229-2238.

156. Liu, Y., et al., *Orientation effects in nanoindentation of single crystal copper.* International Journal of Plasticity, 2008. **24**(11): p. 1990-2015.

157. Gerold, V. and H. Karnthaler, *On the origin of planar slip in fcc alloys.* Acta Metallurgica, 1989. **37**(8): p. 2177-2183.

158. Jackson, A.G., *Handbook of Crystallography*. 1991: Springer.

159. Madge, S., H. Rösner, and G. Wilde, *Transformations in supercooled Pd40. 5Ni40. 5P19.* Scripta materialia, 2005. **53**(10): p. 1147-1151.

160. Pelletier, J.-M. and B. Van de Moortèle, *Phase separation and crystallization in the Zr41. 2–Ti13. 8–Cu12. 5–Ni10–Be22. 5 bulk metallic glass determined by physical measurements and electron microscopy.* Journal of non-crystalline solids, 2003. **325**(1-3): p. 133-141.

161. Weidner, A., U.D. Hangen, and H. Biermann, *Nanoindentation measurements on deformation-induced α′-martensite in a metastable austenitic high-alloy CrMnNi steel.* Philosophical magazine letters, 2014. **94**(8): p. 522-530.

162. Ziegenhain, G., A. Hartmaier, and H.M. Urbassek, *Pair vs many-body potentials: Influence on elastic and plastic behavior in nanoindentation of fcc metals.* Journal of the Mechanics and Physics of Solids, 2009. **57**(9): p. 1514-1526.

163. Rinaldi, R., et al., *Modelling of the mechanical behaviour of amorphous glassy polymer based on the Quasi Point Defect theory—Part I: Uniaxial validation on polycarbonate.* International Journal of Non-Linear Mechanics, 2011. **46**(3): p. 496-506.

164. Qiao, J. and J.-M. Pelletier, *Mechanical relaxation in a Zr-based bulk metallic glass: analysis based on physical models.* Journal of Applied Physics, 2012. **112**(3): p. 033518.

165. Bergfjord, C. and B. Holst, *A procedure for identifying textile bast fibres using microscopy: flax, nettle/ramie, hemp and jute.* Ultramicroscopy, 2010. **110**(9): p. 1192-1197.

166. Berger, W., et al., *Textile Faserstoffe - Beschaffenheit und Eigenschaften*, ed. W. Bobeth. 1993: Springer.

167. Bockhorn, H., et al., *Kinetic study on the thermal degradation of polypropylene and polyethylene.* Journal of Analytical and Applied Pyrolysis, 1999. **48**(2): p. 93-109.

168. Janiak, C., *Metallocene and related catalysts for olefin, alkyne and silane dimerization and oligomerization.* Coordination chemistry reviews, 2006. **250**(1-2): p. 66-94.

169. Swei, J. and J.B. Talbot, *Viscosity correlation for aqueous polyvinylpyrrolidone (PVP) solutions.* Journal of applied polymer science, 2003. **90**(4): p. 1153-1155.

170. Yahya, G., et al., *Preparation and viscosity behavior of hydrophobically modified poly (vinyl alcohol)(PVA).* Journal of applied polymer science, 1995. **57**(3): p. 343-352.

171. Loría-Bastarrachea, M., et al., *A TG/FTIR study on the thermal degradation of poly (vinyl pyrrolidone).* Journal of thermal analysis and calorimetry, 2011. **104**(2): p. 737-742.

172. Li, J., J. Mayer, and E. Colgan, *Oxidation and protection in copper and copper alloy thin films.* Journal of applied physics, 1991. **70**(5): p. 2820-2827.

173. Peng, Z. and L.X. Kong, *A thermal degradation mechanism of polyvinyl alcohol/silica nanocomposites.* Polymer Degradation and Stability, 2007. **92**(6): p. 1061-1071.

174. Chen, Y., P. Renner, and H. Liang, *Dispersion of nanoparticles in lubricating oil: A critical review.* Lubricants, 2019. **7**(1): p. 7.

175. Hackner, M. and J. Spatz, *Thermal bonding of non-round fibers without fundamental change of the aspect ratio*. 2021.

176. Hackner, M., J. Spatz, and T. Jahnke, *Filter*. 2020.

177. Kuper, A., et al., *Self-diffusion in copper.* Physical Review, 1954. **96**(5): p. 1224.

178. Hackner, M., et al., *Network of metal fibers, method for producing a network of metal fibers, electrode and battery* 2018.

179. Taub, A.I. and F. Spaepen, *The kinetics of structural relaxation of a metallic glass.* Acta Metallurgica, 1980. **28**(12): p. 1781-1788.

180. Wang, W.H., et al., *Stability of ZrTiCuNiBe bulk metallic glass upon isothermal annealing near the glass transition temperature.* Journal of materials research, 2002. **17**(6): p. 1385-1389.

181. Slipenyuk, A. and J. Eckert, *Correlation between enthalpy change and free volume reduction during structural relaxation of Zr55Cu30Al10Ni5 metallic glass.* Scripta Materialia, 2004. **50**(1): p. 39-44.

182. Tonkov, E.Y., *High pressure phase transformations handbook 1*. 1992: CRC Press.

183. Farley, E., *Microstructure based Multiphysics simulation on Lithium-Ion Batteries - towards the virtual design of a 3D metal fiber current collector*. 2021, University of Stuttgart.

184. Hackner, M., J. Spatz, and D. Hotz, *Dry coated 3D fiber electrodes*. 2021.

185. Hackner, M., et al., *Mono-Multi-valente Ionendiffusion in Batterien*. 2021.

186. Hollemann, A.F. and N. Wiberg, *Anorganische Chemie - Band 1: Grundlagen und Hauptgruppenelemente*. 2017: De Gruyter.

187. Babu, B.V., et al., *Structural and electrical properties of Li4Ti5O12 anode material for lithium-ion batteries.* Results in Physics, 2018. **9**: p. 284-289.

188. Wang, Y., et al., *Improved electrochemical performance of Li (Ni0. 6Co0. 2Mn0. 2) O2 at high charging cut-off voltage with Li1. 4Al0. 4Ti1. 6 (PO4) 3 surface coating.* Chinese Physics B, 2019. **28**(6): p. 068202.

189. Ebbesen, T., et al., *Electrical conductivity of individual carbon nanotubes.* Nature, 1996. **382**(6586): p. 54-56.

190. Zhang, X., et al., *Multiscale Understanding and Architecture Design of High Energy/Power Lithium-Ion Battery Electrodes.* Advanced Energy Materials, 2020. **11**(2).

191. Ogihara, N., et al., *Impedance Spectroscopy Characterization of Porous Electrodes under Different Electrode Thickness Using a Symmetric Cell for High-Performance Lithium-Ion Batteries.* The Journal of Physical Chemistry C, 2015. **119**(9): p. 4612-4619.

192. Liu, G., et al., *Analysis of the heat generation of lithium-ion battery during charging and discharging considering different influencing factors.* Journal of Thermal Analysis and Calorimetry, 2014. **116**(2): p. 1001-1010.

193. Dubarry, M., et al., *Identifying battery aging mechanisms in large format Li ion cells.* Journal of Power Sources, 2011. **196**(7): p. 3420-3425.

194. Liu, B., et al., *Safety issues and mechanisms of lithium-ion battery cell upon mechanical abusive loading: A review.* Energy Storage Materials, 2020. **24**: p. 85-112.

195. Yu, P., et al., *Determination of the lithium ion diffusion coefficient in graphite.* Journal of The Electrochemical Society, 1999. **146**(1): p. 8.

196. Lee, S.-I., et al., *A study of electrochemical kinetics of lithium ion in organic electrolytes.* Korean Journal of Chemical Engineering, 2002. **19**(4): p. 638-644.

197. Song, J., Y. Wang, and C.C. Wan, *Review of gel-type polymer electrolytes for lithium-ion batteries.* Journal of power sources, 1999. **77**(2): p. 183-197.

198. Kufian, M., et al., *PMMA–LiBOB gel electrolyte for application in lithium ion batteries.* Solid State Ionics, 2012. **208**: p. 36-42.

199. Oudenhoven, J.F., L. Baggetto, and P.H. Notten, *All-solid-state lithium-ion microbatteries: a review of various three-dimensional concepts.* Advanced Energy Materials, 2011. **1**(1): p. 10-33.

200. Gao, H., et al., *Revealing the Rate-Limiting Li-Ion Diffusion Pathway in Ultrathick Electrodes for Li-Ion Batteries.* J Phys Chem Lett, 2018. **9**(17): p. 5100-5104.

201. Jia, N., et al., *Surface and chemical diffusion effects of nanowire electrodes in lithium-ion batteries.* Science China Technological Sciences, 2020. **63**(11): p. 2413-2422.

202. Gurtin, M.E. and A.I. Murdoch, *A continuum theory of elastic material surfaces.* Archive for rational mechanics and analysis, 1975. **57**(4): p. 291-323.

203. Gurtin, M.E. and A.I. Murdoch, *Surface stress in solids.* International Journal of Solids and Structures, 1978. **14**(6): p. 431-440.

204. Rupp, R., et al., *Lithium diffusion in copper.* The journal of physical chemistry letters, 2019. **10**(17): p. 5206-5210.

205. Pettinger, K.-H., *Fertigungsprozesse von Lithium-Ionen-Zellen*, in *Handbuch Lithium-Ionen-Batterien*, R. Korthauer, Editor. 2013, Springer Berlin Heidelberg: Berlin, Heidelberg. p. 221-235.

206. Wieder, F., et al., *Röntgentomografische Untersuchung eines kommerziellen Lithium-Ionen-Kondensators.* Materials Testing, 2014. **56**(9): p. 722-727.

207. Schweidler, S., et al., *Volume changes of graphite anodes revisited: a combined operando X-ray diffraction and in situ pressure analysis study.* The Journal of Physical Chemistry C, 2018. **122**(16): p. 8829-8835.

208. McDowell, M.T., et al., *The effect of metallic coatings and crystallinity on the volume expansion of silicon during electrochemical lithiation/delithiation.* Nano Energy, 2012. **1**(3): p. 401-410.

209. Shi, Y., X. Zhou, and G. Yu, *Material and structural design of novel binder systems for high-energy, high-power lithium-ion batteries.* Accounts of chemical research, 2017. **50**(11): p. 2642-2652.

210. Fu, K.K., et al., *Flexible batteries: from mechanics to devices.* ACS Energy Letters, 2016. **1**(5): p. 1065-1079.

211. Tao, T., S. Lu, and Y. Chen, *A review of advanced flexible lithium-ion batteries.* Advanced Materials Technologies, 2018. **3**(9): p. 1700375.

212. Wang, C., et al., *Electrochemical performance of modified artificial graphite as anode material for lithium ion batteries.* Ionics, 2013. **19**(2): p. 221-226.

213. Pinson, M.B. and M.Z. Bazant, *Theory of SEI formation in rechargeable batteries: capacity fade, accelerated aging and lifetime prediction.* Journal of the Electrochemical Society, 2012. **160**(2): p. A243.

214. Etacheri, V., et al., *Challenges in the development of advanced Li-ion batteries: a review.* Energy & Environmental Science, 2011. **4**(9): p. 3243-3262.

215. Lim, H.-D., et al., *A review of challenges and issues concerning interfaces for all-solid-state batteries.* Energy Storage Materials, 2020. **25**: p. 224-250.

8. Acknowledgement

My greatest thanks go to Prof. Joachim P. Spatz for the unique opportunity to write my doctoral thesis on such a diverse and unique project. Not only the exciting project itself, but also the unparalleled opportunities for experimental and personal development in this project were an unforgettable time for me. I don't think there is another PhD student who had the opportunity to develop a finished high-tech product from the smallest component to the end and to build a complete prototype line on a laboratory scale. Without the highly motivated environment, such work would not have been possible. In particular, the intensive personal exchange of ideas on a project that was new to both of us in this depth was, I believe, a lot of fun for both of us and brought us a long way forward.

My next thanks go to Prof. Martin Möller for kindly taking on the role as reviewer for my PhD.

Without a large number of colleagues, staff, students and the entire technical and administrative staff, this work would not have been possible to this extent. First and foremost, Dr. Timotheus H. Jahnke, who joined the project first as an "advisor" and then as a colleague, and who played a decisive role in shaping the entire development of the fiber network-based lithium-ion battery and bringing it forward. Especially his deep theoretical knowledge of the lithium-ion battery and the resulting simulations have contributed decisively to understanding and explaining the novel processes in detail. I would also like to thank him for the many micro-CT measurements and pore size determinations of the networks, of which only one ultimately made it into the thesis. No less important during the almost complete time was Daniel C. Hotz, who tirelessly and sometimes even on weekends and holidays stood with me in the lab to perform urgently needed test series or repairs. Many thanks for the years of "on-call" service. With both of the aforementioned, we will probably all be able to remember Berlin and Itzehoe with a smile for many years to come. I would like to thank Lea-Sophie Hornberger for her contribution to the project during her internship semester and especially for the studies on the usability of polymer fibers in mesh production. I thank Svenja Hiotidis, Simone Bauder and Mark Otterbach for all the preparatory work in the lab, especially for the billions of chopped fibers that were prepared with almost no grumbling. I also thank Erik A. Farley and Wenzel U. Gassner for their dedicated help in the lab and the many good ideas for new process possibilities. Erik A. Farley deserves special mention here. During his master's thesis, he helped me to better understand the processes in the electrodes and, above all, to represent them graphically. This helped me a lot here in the thesis to show the processes. I would like to thank Yuanzhen Wang for his incredible mathematical understanding and simulative skills, which have already had a significant impact on the project and will do so even more in the future.

Dr. Sebastian Weber and Louise M. K. Kaeswurm I thank for the many kilos of copper fibers that I was able to use to do this work. I was very impressed with the progress in fiber production and advancement. I thank Dr. Alexandre Micoulet for the Vitrovac fibers. Also, the technical discussions with all three of them on the production of the fibers helped me decisively in understanding and being able to measure the properties.

I thank Gerd Maier (ZWE Materials, Max Planck Institute for Intelligent Systems Stuttgart) for the XRD measurements and his expertise on crystal structures and their characterization.

From the non-scientific side, special thanks go to Jörg Graf from the Max Planck Institute for Medical Research in Heidelberg with his purchasing team, who always provided me and us with the materials and equipment we needed and made everything possible, no matter how unusual our requests were. From the Max-Planck-Institutes in Stuttgart, especially the mechanical workshop under the direction of Thomas Frey has to be mentioned, who always carried out our prototypes, conversions and modifications in perfect execution in the shortest possible time. Especially Martin Großmann has to be mentioned here, who repaired our oven retort many times and in the end rebuilt it better than the manufacturer. In general, many names from the fields of building services, electronics, precision mechanics, glassblowing, etc. should be mentioned here, without whose cooperation such a comprehensive project would not have been possible.

I would like to thank Dr. Achim M. Diem , Elisabeth Pfeilmeier and Louise M. K. Kaeswurm above all for editing my dissertation.

I acknowledge highly the kidly providing of fibers samples from the DWI Aachen, IFG Asota Linz and Advansa Hamm.

An finally, Dr. Achim Diem, Leila Raafat, Timotheus H. Jahnke and Louise M. K. Kaeswurm, who helped me to find my way over the one or other hard phases of the dissertation in a culinary way.

Eidesstattliche Versicherung gemäß § 8 der Promotionsordnung der Naturwissenschaftlich-Mathematischen Gesamtfakultät der Universität Heidelberg

1. Bei der eingereichten Dissertation zu dem Thema „Fiber based 3D current collector towards ultra-thick batteries - From single property to electrode production -” handelt es sich um meine eigenständig erbrachte Leistung.

2. Ich habe nur die angegebenen Quellen und Hilfsmittel benutzt und mich keiner unzulässigen Hilfe Dritter bedient. Insbesondere habe ich wörtlich oder sinngemäß aus anderen Werken übernommene Inhalte als solche kenntlich gemacht

3. Die Arbeit oder Teile davon habe ich bislang nicht an einer anderen Hochschule des In- oder Auslandes als Bestandteil einer Prüfungs- oder Qualifikationsleistung vorgelegt.

4. Die Richtigkeit der vorstehenden Erklärung bestätige ich.

5. Die Bedeutung der eidesstattlichen Versicherung und die strafrechtlichen Folgen einer unrichtigen oder unvollständigen eidesstattlichen Versicherung sind mir bekannt.

Ich versichere an Eides statt, dass ich nach bestem Wissen die reine Wahrheit erklärt und nichts verschwiegen habe.

--------------------	--------------------
Ort und Datum	Unterschrift